Concurrent measurement method of spindle radial, axial and angular motions using concentric circle grating and phase modulation interferometers

同心円回折格子と位相変調干渉計を用いた軸受のラジアル　アキシャル　アンギュラモーションの同時測定法

MUHUMMAD MADDEN

ID: 08514885

Supervisor: Prof. Masato AKETAGAWA

Information Science and Control Engineering

Nagaoka University of Technology

Nagaoka, Niigata, Japan

Acknowledgments

Contents

List of abbreviations

ANSI	American National Standards Institute
APD	Avalanche Photodetector
ASME	American Society of Mechanical Engineers
BS	Beam Splitter
DC	Direct Current
DAQ	Data Acquisition
FFT	Fast Fourier Transform
FG	Function Generator
FM	Fixed Mirror
HOPG	Highly Oriented Pyrolytic Graphite
HWP	Half-Wave Plate
ISO	International Organization for Standardization
LD	Laser Diode
LIA	Lock-in Amplifier
LVDT	Linear Variable-Differential Transformer
NC	Numerical Control
P	Polarizer
PBS	Polarized Beam Splitter
PC	Personal Computer
PD	Photodetector
PSD	Position Sensitive Detector
PZT	Piezoelectric Transducer
QWP	Quarter-Wave Plate
SEM	Scanning Electron Microscope
SM	Steering Mirror
STM	Scanning Tunneling Microscope

List of nomenclatures

y_A	Y-axis displacement of optical sensor A
z_A	Z-axis displacement of optical sensor A
x_B	X-axis displacement of optical sensor B
z_B	Z-axis displacement of optical sensor B
x_C	X-axis displacement of optical sensor C
z_C	Z-axis displacement of optical sensor C
R_A	Distance from optical sensor A to the center of rotation
R_B	Distance from optical sensor B to the center of rotation
R_C	Distance from optical sensor C to the center of rotation
R	Average distance of optical sensor A, B, and C from the center of rotation
R_x	X-axis radial motion
R_y	Y-axis radial motion
R_z	Axial motion
θ_x	Angular motion in angular direction of the X-axis
θ_y	Angular motion in angular direction of the Y-axis
θ_i	Incident angle
$\boldsymbol{S}$	Unit vector along the incident light direction
$\boldsymbol{S'}$	Unit vector along the diffraction light direction
$\boldsymbol{\varepsilon}$	Unit vector normal to the grating plane
$\boldsymbol{q}$	Unit vector along the ruling direction
m	Diffraction order
d	Grating pitch
n	Refractive index
λ	Vacuum wavelength of the light source
θ_{iXZ}	Incident angle on the XZ plane
θ_{iYZ}	Incident angle on the YZ plane
θ_{iZ}	Small angle between incident light and the Z-axis
θ_{+1}	+1st-order diffraction angle
θ_{-1}	-1st-order diffraction angle
θ_{+2}	+2nd-order diffraction angle

θ_{-2}	-2nd-order diffraction angle
$\Delta\phi_{+1}$	Phase shift of the +1st-order diffraction
$\Delta\phi_{-1}$	Phase shift of the -1st-order diffraction
Δx	Displacement shift of the grating along the X-axis
Δy	Displacement shift of the grating along the Y-axis
Δz	Displacement shift of the grating along the Z-axis
E_{+1}	Electrical field amplitude of +1st-order diffraction
E_{-1}	Electrical field amplitude of -1st-order diffraction
φ_{+1}	Initial phase of +1st-order diffraction
φ_{-1}	Initial phase of -1st-order diffraction
I_{fix0}	Interference light intensity between FM and 0th-order diffraction of the grating
$I_{\pm1}$	Interference light intensity of $\pm1^{st}$ order diffraction of the grating
E_{fix}	Electrical field amplitude of the light reflected from the fixed mirror
E_0	Electrical field amplitude of the light reflected from the grating
ψ	Initial phase of 0th-order diffraction
L	Distance between the grating and PD1
ω_m	Sinusoidal angular modulation frequency
E_F	Electrical field amplitude of the light reflected from the fixed mirror
E_{+2}	Amplitudes of the light diffracted from +2nd-order of the grating
E_{-2}	Amplitudes of the light diffracted from -2nd-order of the grating
$\varphi_{int,0}$	Initial phase of Michelson interferometer
$\varphi_{int,\pm2}$	Initial phase of grating interferometer
f	Frequency of the light source
L_{int}	Optical path difference of Michelson interferometer arms
$L_{\pm2}$	Optical path difference of grating interferometer arms
f_0	Center frequency
Δf	Modulation frequency
$\Delta\lambda$	Wavelength modulation
φ_0'	Initial phase of Michelson interferometer
$k_{m,0}$	Modulation depth of Michelson interferometer
J_m	Bessel coefficient of m-order
$2\omega_m$	2nd-harmonic sinusoidal angular modulation frequency
$3\omega_m$	3rd-harmonic sinusoidal angular modulation frequency
$J_2(k_{m,0})$	Bessel function of the 2nd-harmonic of Michelson interferometer

$J_3\left(k_{m,0}\right)$	Bessel function of the 3rd-harmonic of Michelson interferometer
$\varphi'_{\pm2}$	Initial phase of grating interferometer
$k_{m,\pm2}$	Modulation depth of grating interferometer
$J_2\left(k_{m,\pm2}\right)$	Bessel function of the 2nd-harmonic of grating interferometer
$J_3\left(k_{m,\pm2}\right)$	Bessel function of the 3rd-harmonic of grating interferometer
f_b	Frequency bandwidth
R_f	Resistance
C_f	Capacitance
$I'_z\left(3\omega_m\right)$	Interference light intensity the 3rd-harmonic of Michelson interferometer after normalization
$I'_z\left(2\omega_m\right)$	Interference light intensity the 2nd-harmonic of Michelson interferometer after normalization
$I'_x\left(3\omega_m\right)$	Interference light intensity the 3rd-harmonic of grating interferometer after normalization
$I'_x\left(2\omega_m\right)$	Interference light intensity the 2nd-harmonic of grating interferometer after normalization
f_s	Sampling rate
v_{max}	Maximum speed
$r\left(\theta\right)$	Roundness profile error
S_B	Output signal of optical sensor B
S_C	Output signal of optical sensor C

List of figures

List of tables

Chapter 1

Introduction

1.1 Research background

The industrial processes for ultraprecision engineering and metrology require high-quality control of products. In particular, the axis of rotation of rotary systems is important for instance the spindle error motion of the aligner, wire bonder, and inspector machines results in substandard manufactured goods. Precision of the rotary spindle is required to enhance the accuracy of spindle motion to the nanometer and submicroradian levels [1,2]. Since the ultraprecision fabrication of machines and information technology instruments, such as hard disks, has progressed very rapidly, the industry intends to increase the rotation speeds up to 100 krpm or more. At the same time, reductions in spindle rotation errors (radial, axial and angular motion) to the nanometer and submicroradian levels are required [3]. To evaluate and improve the performance of such precision rotary stages, unessential movements on the other five degrees of freedom (which are radial (2 degrees), axial (1 degree) and angular (2 degrees)) of the rotary stage must be measured and analyzed [4,5]. Unessential movements are typically measured using a displacement measuring sensor relative to a high precision sphere or cylinder [6,7]. Output data of sensors include profile error, centering error and error motion [8,9]. Through the years, several separation techniques have been developed for accurate measurement of the profile error of reference artifacts and the error motion of a spindle. These include the Donaldson's reversal method [10,11], the multistep method [12-15], and the multiprobe method [16-18]. The Estler face motion reversal method allows the separation of tilt and axial error motion from the circular flatness of a reference part [19,20]. The error motion of an axis of rotation, and the measurement method have been specified in ANSI/ASME standards. In 1985, ANSI adopted a standard which fully describes the testing of axes of rotation and its terminology (ANSI/ASME B89.3.4M) [21]. In 2010, the latest ASME B89.3.4 standard was published [22]. Later ISO standard published its own version: ISO 230-7 [23]. There are a variety of testing methods and equipment available for measuring the error motion of a freely rotating machine tool spindle [24-32].

Conventional spindle error motion measurements are carried out using the error separation methods [33-36], which require displacement sensors and reference artifacts. There are several kinds of displacement sensors that are proposed or used in industry and research studies on spindle motion measurement. The main features are given belows;

- Capacitive displacement sensors

  The principle of capacitive displacement sensors is based on measuring the change of capacitance between two electrodes. Capacitance is a function of the distance between two electrodes, the surface area of the electrodes, and the permittivity of the dielectric between the electrodes. Therefore, when the capacitance of two electrodes is changed, the gap or displacement between them can be determined. Capacitive displacement sensors can be applied in many applications, such as precision positioning stages [37,38], spindle measurement [39-42] and vibration measurement [43,44]. The advantages of Capacitive displacement sensors compared with other noncontact measurement techniques are their higher resolution (nanometer order), lower cost and smaller size [45-47]. However, a wet or polluted environment is not suitable for these kinds of sensors. Moreover, the sensors have to be calibrated using an instrument having direct traceability to a primary standard of length [48-50]. Another disadvantage of these kinds of sensors is their narrow measurement range (micrometer order), but many researchers are attempting to increase their measurement range up to the millimeter order [51-53].

- Inductive displacement sensors

  Inductive displacement sensors are based on the principle of magnetic circuits. The change in the output voltage depends on the position change of the core. The most popular inductive-type sensors are the linear variable differential transformers (LVDT) and the eddy current sensors. They are widely used in industry in many applications because they are robust and compact, and are less affected by environmental factors (e.g., humidity and dust) than the capacitive-type sensors. However, an external magnetic field can affect their performance [54-56]. They are also applied for high-precision measurement of spindle motion [57-60]

- Laser interferometer displacement sensors

Laser interferometers are used to compare the changes in optical path length with the wavelength of light. They are the most popular devices for length or displacement measurements in industry and in many research studies [61-63], due to their direct traceability to a primary standard of light [64]. However, interferometers usually are operated in ambient air. Thus, environmental factors that influence the speed of light in air will affect the precision of measurement, such as the uncertainties of the wavelength of the laser source and the refractive index of the ambient air [65]. Laser interferometers can be used for many applications such as length or displacement measurements [66-72], precision positioning [73-77], shape or surface measurements [78-82], and spindle measurement [83-86].

- Ultrasonic displacement sensors

The basic principle of ultrasonic displacement sensors as a measurement tool is based on the time-of-flight method. When an ultrasound signal is transmitted to a target, it is reflected, and the elapsed time from emission to detection of the reflected signal is measured [87,88]. This sensor can be applied to control the spindle rotation center [89].

- Optical encoder displacement sensors

Optical encoders [90-95] are used for many applications, such as in machine tools, industrial robots, and a variety of instruments, as they are interfaced to digital systems which make them very easy to use. Optical encoders consist of a main grating, a light source, and a detection system. The main grating represents the scale or the measurement standard. The resolution of the optical encoder depends on the grating pitch and signal detection method. The interpolation method, in which two signals with a 90° phase difference are calculated, is normally used to process the signals from a detector. Some researchers have used an optical encoder to measure spindle axial motion [96,97].

- Fiber-Optic and Photo Electric sensor

The principle of optical fiber optic and photoelectric sensors is based on the time-of-flight method or sensing a change in the amount of light that is reflected by a

target. The main devices used are a light source and a photodetector [98]. The fiber optic sensor can be applied for real-time monitoring of the spindle axis by the centering its runout [99]

However, the advantages and disadvantages of displacement sensors, such as cost, resolution, measuring range, sensitivity, environmental factors, traceability, etc., should be considered in order to select a suitable displacement sensor for each applications or target measurement. Many researchers have applied a reference artifact for spindle radial or axial motion measurement (one degree of freedom) using their own measurement techniques. For example;

- Castro et al. [19] applied a high-precision spherical artifact with a heterodyne laser interferometer to measure the radial and axial motion of a spindle. The measurement is carried out using reflection directly from a high-precision sphere artifact, which is attached to the spindle. The principle of measurement is similar to that of a linear interferometer, except that the high-precision sphere is used instead of the usual reflector.

- Okuyama et al. [23] applied a cylindrical artifact with three capacitive sensors to measure the radial motion of a high-speed spindle for hard disk inspection by the three-point method. They achieved a measurement resolution of submicrometer order.

- Kimoto et al. [96] applied a cylindrical rod with a circular grating [97], and an optical encoder head to measure the axial motion of a spindle. They achieved a measurement resolution of submicrometer order.

- Fujimaki et al. [100] applied a small spherical ball artifact with a laser auto-collimation technique and a quadrant photodetector to measure the radial motion of a high-speed spindle. The measurement results show that the optical measuring device is able to measure the radial error motion of ultrahigh-speed spindles with a maximum rotational speed of 200 krpm.

- Park et al. [101] applied two concentric circle grating with a laser interferometer to measure the radial motion of a spindle. Based on the moire method, two concentric circle gratings with fine pitches were configured for the radial motion to be directly detected by analyzing the interferometric fringes generated by the gratings. A measuring accuracy of less than 0.01 μm can be practically achieved using this method.

- Liu et al. [102] applied a rotational fixture with a corner cube and a two-dimensional position-sensitive detector (PSD) to measure the radial motion of a spindle. When the spindle rotates, the spindle error changes the direction of the beam reflected from the corner cube and also the positions of the spots on the PSD. Thus, the radial runout of the spindle can be obtained via the PSD outputs.
- Chaikool et al. [103] applied a regular crystalline lattice of highly oriented pyrolytic graphite (HOPG) with a two-dimensional reference scale and a scanning tunneling microscope (STM) for direct measurement of spindle error motion. They achieved a measurement resolution of 10 picometer order.

Using the above measurement techniques, we can measure only one degree of freedom of spindle motion; however, concurrent measurements of multiple degrees of freedom are required to increase the accuracy of measurement. Some researchers have also achieved multi degrees of freedom of spindle motion. For example;

- Grejda et al. [1] applied a double ball bar artifact with five capacitive sensors to measure five degrees of freedom of spindle motions. They achieved a measurement resolution of nanometer order.
- Murakami et al. [3] applied a ball lens and a rod lens artifact with multiple divided photodiodes to measure five degrees of freedom of spindle motion. The results show that this measurement system has a resolution of 5 nm and can be used to evaluate high-speed micro spindle rotation errors.
- Gao et al. [104] applied a cylindrical artifact with two-dimensional slope sensors for measurement of four degrees of freedom (which are radial (2 degrees) and angular (2 degree)) of spindle motion. The sensors are placed around a cylindrical workpiece in the same XY-plane perpendicular to the spindle axis, to measure the deviation from roundness and the X- and Y-directional components of the spindle radial error motion. The angular error motion can be obtained accurately from the angular direction outputs of sensors.
- Marsh et al. [105] applied a spherical ball artifact with capacitive sensors to measure three degrees of freedom (which are radial (2 degrees) and axial (1 degree)) of spindle motion. They achieved a measurement resolution of submicrometer order.

However, these reference artifacts also have some disadvantages when we apply them for spindle measurement. They are voluminous, with a large mass and complicated structure and may inhibit the original rotational motion of the spindle. Moreover, some displacement sensors, such as capacitive displacement sensors, one of the popular types of displacement sensors, have narrow bandwidths, and maintaining the traceability against the meter definition is difficult because of their drift characteristic. Therefore, a new measurement technique for five degrees of freedom spindle motion is still required to improve the accuracy of measurement of an ultrahigh precision spindle.

1.2 Research objective and outline

As described in the previous section, the concurrent measurement method is required to measure five degrees of freedom spindle motion. Therefore, the main objective of this thesis is to propose a novel method for the concurrent measurement method of spindle radial, axial, and angular motion using concentric circle grating and phase modulation interferometers. this thesis is a summary of three archived journal papers: Paper 1: Muhummad Madden, Masato Aketagawa, Yuria Ohkubo, Shohei Kimura, Hideki Maruyama, Satoru Higuchi, and Eiki Okuyama, "Proposal of concurrent measurement method for spindle radial, axial and angular motions using concentric grating interferometers", International Journal of Surface Science and Engineering, Vol. 3, No. 3, pp. 242-252 (2009). Paper 2: Muhummad Madden, Masato Aketagawa, Shuhei Uesugi, Takuya Kumagai, and Eiki Okuyama, "Spindle error motion measurement using concentric circle grating and phase modulation interferometers", International Journal of Automation Technology, Vol. 7, No. 5, pp. 506-513 (2013). Paper 3: Muhummad Madden, Masato Aketagawa, Takuya Kumagai, Yoshitaka Maeda, and Eiki Okuyama, "Concurrent measurement method of spindle radial, axial, and angularmotions using concentric circle grating and phase modulation interferometers", Measurement Science and Technology, (paper has been accepted for publication, date accepted: 7 May 2014).

This thesis describes a novel method for the concurrent measurement of five degrees of freedom spindle motion errors (which are radial (2 degrees), axial (1 degree) and angular (2 degrees)) using a concentric circle grating and phase modulation interferometers. In this method, a concentric circle grating plate with a fine pitch is installed on top of the spindle of interest, and this is used as the reference artifact. As the concentric circle grating plate is not voluminous or heavy, this method is effective for any spindle, and does not affect the

original rotational motion of the spindle. As this method is based on wide-bandwidth photosensors, it is possible to apply it to high-rotational-speed spindles. Moreover, this method is suitable for maintaining the traceability against the meter definition through the calibration of the wavelength of the light source and the grating pitch using the measurement standard.

The thesis is organized into 5 chapters:

Chapter 1- Introduction. This chapter highlight the present requirements of nanometrology and ultraprecision engineering techniques for measurement of spindle rotation error to the nanometer or submicroradian level. The objective of the author's work is presented. The outline of the thesis is also briefly described.

Chapter 2 – Principle of spindle motion measurement. This chapter describes the definition of five degrees of freedom spindle motion. The principle of concurrent measurement of spindle radial, axial, and angular motion using a concentric circle grating and three optical sensors is explained. An outline of the concentric circle grating is also presented.

Chapter 3 – Principle of the optical sensor. This chapter describes the structure of the optical sensor which consists of two-axes displacement-measuring interferometers (Michelson and grating interferometers). In this measurement the quadrature detection techniques (the previous research) [106] and phase modulation techniques (the current research) are applied to obtain the Lissajous diagram [113]. The displacement is measured using the Lissajous diagram.

Chapter 4 – Spindle motion measurement using quadrature detection technique. This chapter describes the instrumentations and the measurement results of the Michelson and grating interferometers. The compact-size optical sensor performance and the five degrees of freedom spindle motion using three optical sensors when we apply the quadrature detection technique to the interferometers are described. The effects of crosstalk error on the Michelson and grating interferometers are also discussed.

Chapter 5 – Spindle motion measurement using phase modulation technique. This chapter describes the instrumentations and the measurement results of the Michelson and grating interferometers as well as the high-rigidity compact optical sensor performance and the five

degrees of freedom spindle motion when we apply the phase modulation technique to the interferometers. The effect of the interpolation error on the displacement is also discussed.

Chapter 6 – Discussions, overall conclusions, and future works. A review of the author's research work and some conclusions for future studies are discussed.

Chapter 2

Principle of spindle motion measurement

This chapter describes the principle of spindle motion measurement using the definition of five degrees of freedom spindle motion. The concurrent measurement principle of spindle radial, axial, and angular motions using the concentric circle grating and three optical sensors is explained. The outline of the concentric circle grating is also presented.

2.1 Definition of five degrees of freedom spindle motion
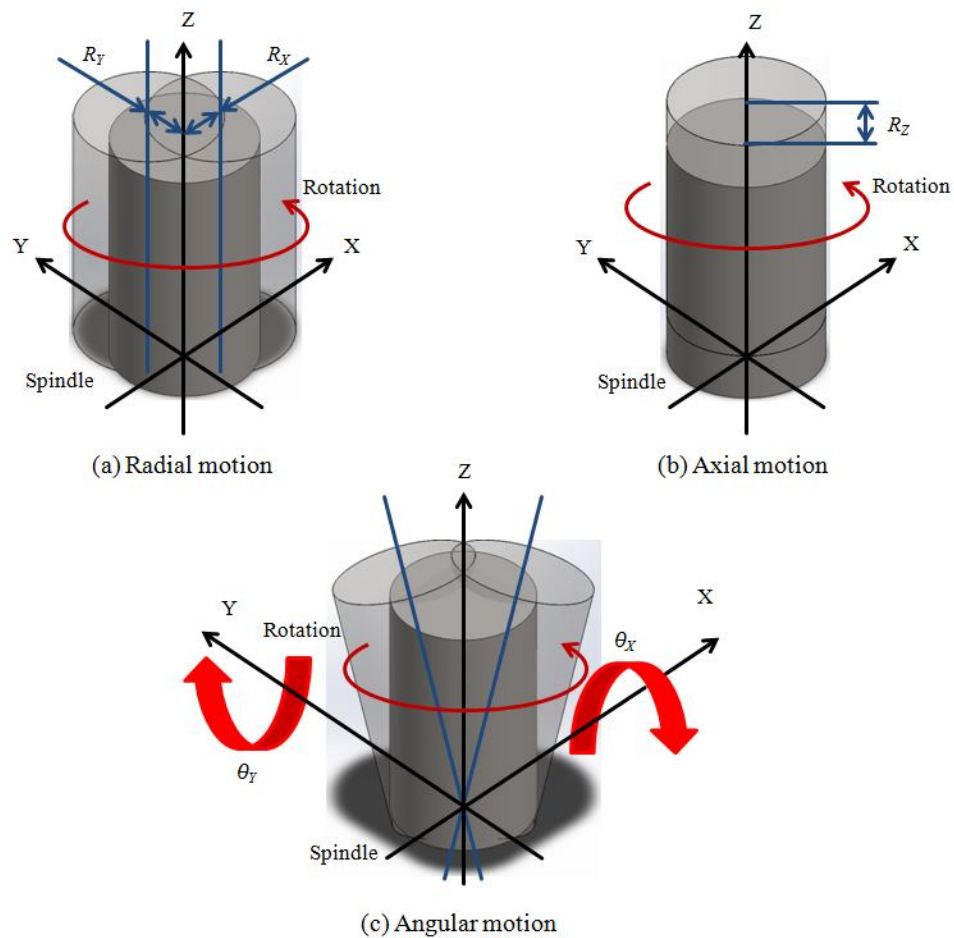
Fig. 2.1 Definitions of spindle radial, axial, and angular motion

It is important to introduce the nomenclature and definitions of axis of rotation metrology, which are used throughout this thesis. A spindle is the physical embodiment of an axis of rotation – it restricts movement in all but one rotational direction of freedom. The measurement of spindle motion errors is realized from a basic mechanical component of ideal spindles, which must rotate with only one degree of freedom; therefore, other types of extra motion with five degrees of freedom (which are radial (2 degrees), axial (1 degree) and angular (2 degrees)) are identified as error motion, which must be eliminated or reduced.

The spindle motion errors are small departures of the axis of spindle rotation relative to stationary reference coordinate axes (X, Y, Z). The five components of these motion errors are translations in the X, Y, and Z directions and rotations (or tilting) about the X- and Y-axes. Figure 2.1 specifies the five degrees of freedom of spindle motion. In Fig. 2.1, the Z-axis is the ideal rotational axis. These components consist of radial motion, axial motion, and angular motion. *Radial motion* is the error motion in the X and Y directions at a specified axial location on the Z-axis. *Axial motion* is the error motion along the Z-axis. *Angular motion* is the error motion in the X and Y angular directions relative to the Z-axis.
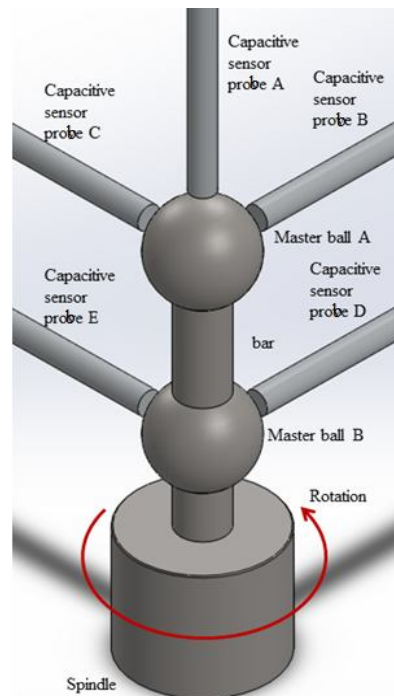
Fig. 2.2 Conventional artifact [12]

As described in chapter 1, conventional spindle error motion measurements are carried out by error separation methods, which require displacement sensors and reference artifacts. Figure 2.2 shows a conventional artifact used to measure five degrees of freedom spindle motion errors (which are radial (2 degrees), axial (1 degree) and angular (2 degrees)) [1]. Complicated artifacts, such as two spherical balls linked with a bar (or cylinder), and five displacement sensors are required to measure five degrees of freedom spindle motion errors. Some techniques used to separate the two contributions are also necessary. Several error separation techniques are used to separate the spindle error motion from the artifact error, for example, Donaldson reversal, the multistep, and the multiprobe methods (see Appendix A).

2.2 Principle of the concurrent measurement of spindle radial, axial, and angular motion using a concentric circle grating and three optical sensors

The measurement principle of the concurrent measurement of spindle radial, axial, and angular motion using a concentric circle grating and three optical sensors is shown in Fig. 2.3.
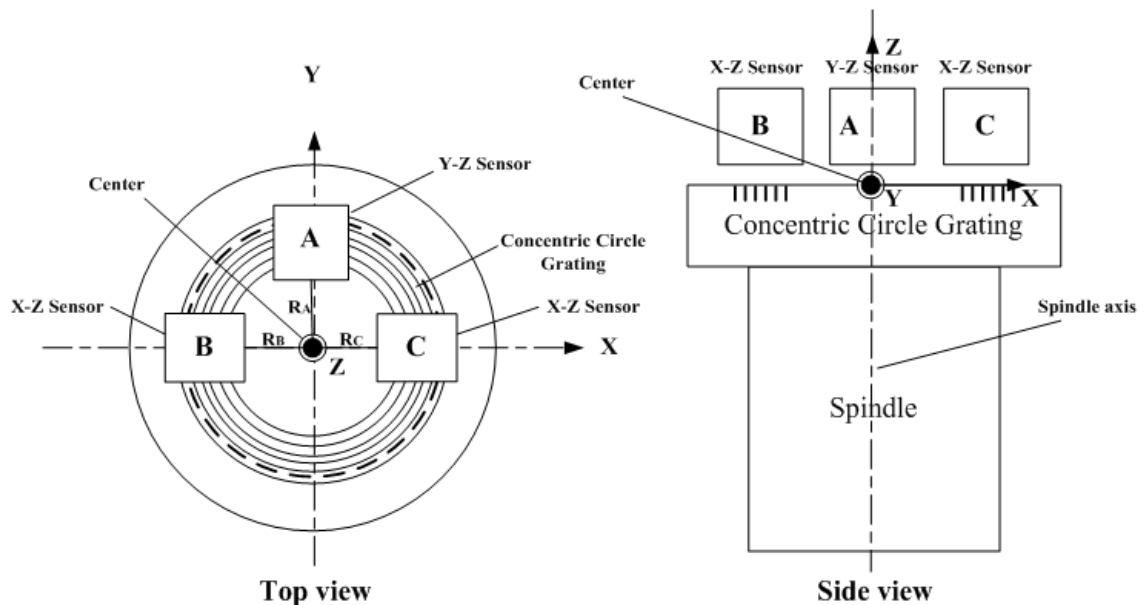
Fig. 2.3 Measurement principle of the concurrent measurement of spindle radial, axial, and angular motions using a concentric circle grating and three optical sensors.

A concentric circle grating is set on top of the spindle of interest. Three optical sensors A, B and C are fixed over the concentric circle grating. To reduce the centering error, the spindle rotation center must be aligned to the center of the concentric grating to within an accuracy of 1μm or less. The grating plane must also be aligned to be parallel with the XY plane within 10 arcsec to reduce the crosstalk error (see sect. 4.3). In Fig. 2.3, the center is selected as the origin of the XYZ coordinate system, and the Z-axis is the ideal rotational axis. Optical sensor A is located along the Y-axis with distance R_A from the center and measures the Y-axis and Z-axis displacements y_A and z_A using the concentric circle grating, whereas optical sensors B and C are located along the X-axis with distances R_B and R_C from the center and measure the X-axis and Z-axis displacements x_B, z_B, x_C, and z_C using the concentric circle grating, respectively. From the displacements measured by the three interferometers, the radial R_x, R_y, axial R_z, and angular θ_x, θ_y motion can be derived as follows [106]:

$$R_x = \frac{1}{2}(x_B + x_C),\tag{2.1}$$

$$R_y = y_A,\tag{2.2}$$

$$R_z = \frac{1}{3}(z_A + z_B + z_C),\tag{2.3}$$

$$\theta_x = \frac{1}{R}\left\{z_A - \frac{(z_B + z_C)}{2}\right\},\tag{2.4}$$

$$\theta_y = \frac{1}{2R}(z_B - z_C),\tag{2.5}$$

$$R = \frac{1}{3}(R_A + R_B + R_C),\tag{2.6}$$

where R is the average distance of interferometers A, B, and C from the center. In general, the grating exhibits artifact errors (which are roundness, flatness and irregular pitch); however, it is possible to apply the error separation methods (such as Donaldson reversal, multistep, and multipoint) to the concentric circle grating. Therefore, another arrangement of interferometers A, B, and C is possible.

2.3 Outline of the concentric circle grating

In this thesis, the fine concentric circle grating is the key technology for attaining the measurement goal. To confirm the possibility of the concurrent measurement method, a concentric circle grating with a fine pitch of 2 μm was fabricated [106]. Figures 2.4(a) and (b) show a photograph and the design of the prototype concentric circle grating, respectively.
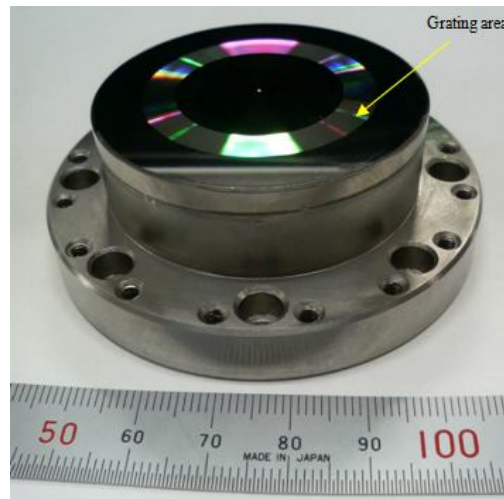
(a) Photograph of the prototype concentric circle grating (2 μm pitch)
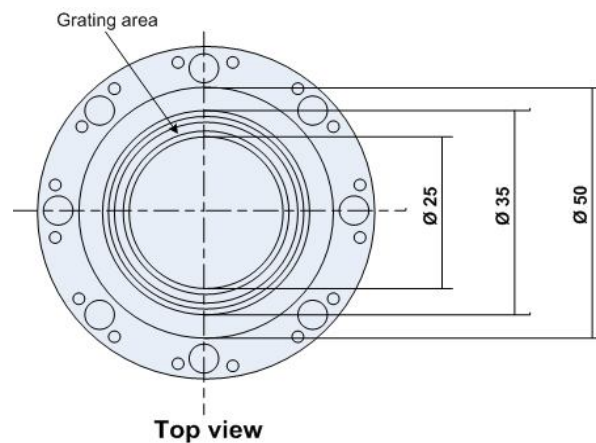
(b) Design of the prototype concentric circle grating

Fig. 2.4 Prototype concentric circle grating
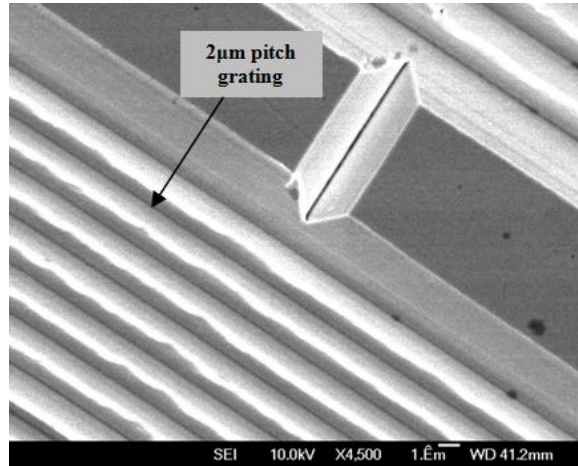
Fig. 2.5 Scanning electron microscopy image of 2-µm-pitch-period grating
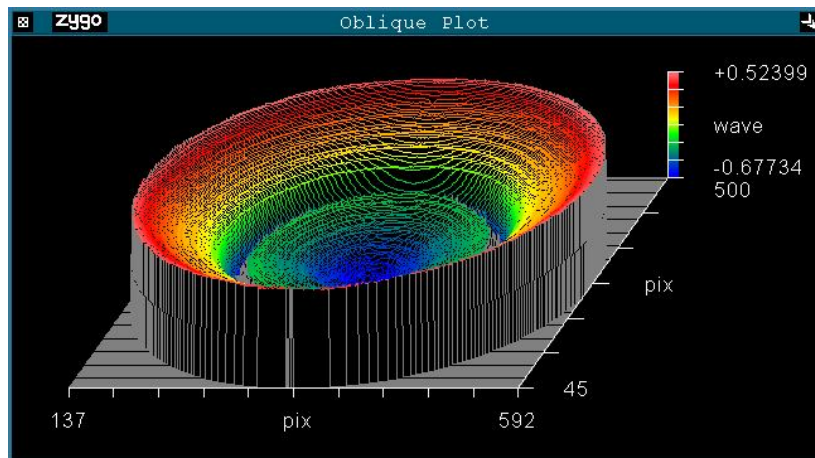
(a) 3D profile of the concentric circle grating
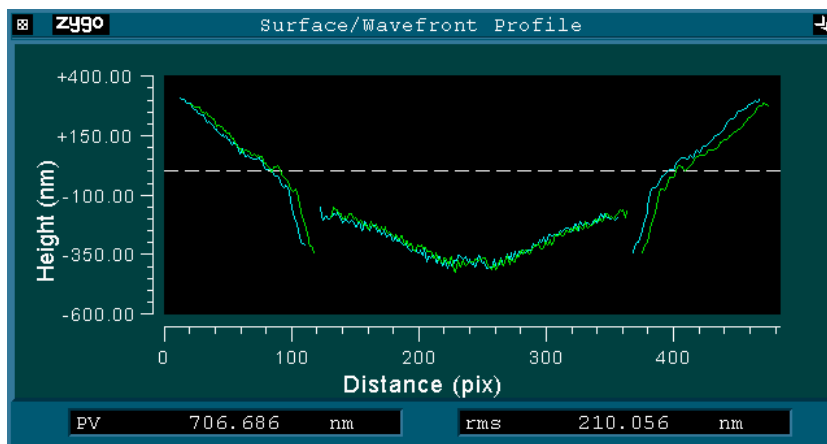
(b) Flatness profile of the concentric circle grating

Fig. 2.6 Image profiles of the concentric circle grating obtained by flatness interferometer

The grating was fabricated using an ultraprecise numerical control (NC) cutting machine tool (ROBONANO, FANUC [107]) and a sharp single-crystal diamond tool with a top radius of 1 μm. The material used was stainless steel with nickel phosphide plating of 100 μm thickness. Numerous grating grooves were formed on the nickel phosphide plate. In the grating, 1000 pitches were formed with a concentric circle structure. To determine the possibility of fabricating narrower gratings using the NC machine and diamond tool, we fabricated a 2-μm-pitch grating. Figure 2.5 shows its SEM image. In Fig. 2.5, the grooved grating shows good uniformity. We also measured the surface flatness of the grating using a flatness interferometer (Zygo, Flatness interferometer [108]), and the result is shown in Fig. 2.6(b). We believe that it is possible to fabricate a concentric circle grating with a fine pitch of 1 μm or less using the NC machine and a diamond tool. If we can use optical (or electron beam) lithography, it should be possible to achieve a grating pitch of 500 nm or less.

Chapter 3

Principle of the optical sensor

This chapter describes the structure of the optical sensor. The optical sensor consists of a laser diode as a light source, and two-axes displacement measuring interferometer (Michelson and grating interferometers). The quadrature detection and phase modulation techniques are applied to the two-axes displacement-measuring interferometers. The principle of the two-axes displacement-measuring interferometers using the quadrature detection and phase modulation techniques is explained in this chapter.

3.1 Two-axes displacement-measuring interferometers using quadrature detection technique
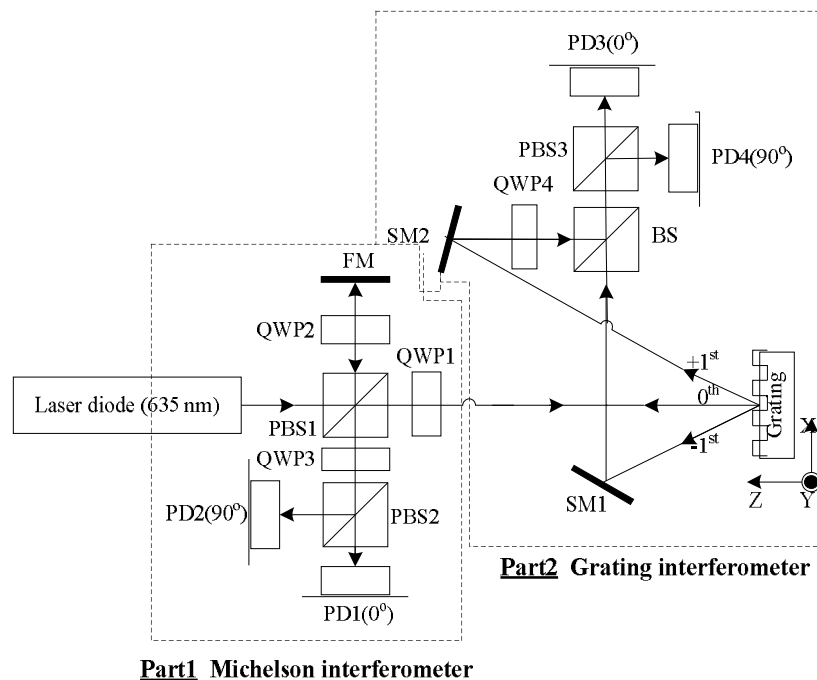
Fig. 3.1 Schematic diagram of two-axes displacement measuring interferometers using quadrature detection technique. PBS: polarized beam splitter, BS: beam splitter, QWP: quarter-wave plate, FM: fixed mirror, SM: steering mirror, and PD; photodetector.

The optical sensor based on the quadrature detection technique consists of a laser diode as a light source and two-axes displacement measuring interferometers (Michelson and grating interferometers) with four photodetectors. The configuration of the optical sensor is shown in Fig. 3.1. In the figure, the X-, Y-, and Z-axes indicate the grating pitch, ruling, and height directions, respectively; therefore, the XY plane is parallel to the grating plane. A light beam emitted from the laser diode is incident on polarized beam splitter1 (PBS1) and is divided into two beams. The first beam reflected from PBS1 reaches the fixed mirror (FM) via quarter-wave plate2 (QWP2) and propagates from FM via PBS1, QWP3, and PBS2 and reaches photodetector1 (PD1) and photodetector2 (PD2). The second beam, which passes through PBS1, reaches the one-dimensional grating via QWP1. In Fig. 3.1, we assume that the incident angle θ_i of the second beam to the grating is almost nulls. Thus, the reflected light (which is 0th-order diffraction light) reaches PD1 and PD2 via QWP1, PBS1, QWP3, and PBS2. At PD1 and PD2, it is possible to detect an interferometer fringe between the reflected light from FM and the grating, and to measure the displacement along the Z-axis of the grating. In this case, the quadrature phase shift of two interference signals can be obtained with a phase difference of 90° (at PD1 0°, and PD2 90°) [109-111].

The incident light on the grating can produce $\pm$ 1st-order diffraction light. The diffraction light direction is derived using the vector format as follows [112]:

$$\boldsymbol{S'} \times \boldsymbol{\varepsilon} - \boldsymbol{S} \times \boldsymbol{\varepsilon} = m \frac{\lambda}{nd} \boldsymbol{q} \, , \tag{3.1}$$

where $\boldsymbol{S}$, $\boldsymbol{S'}$, $\boldsymbol{\varepsilon}$, $\boldsymbol{q}$, m, d, n, and λ represent a unit vector along the incident light direction, a unit vector along the diffraction light direction, a unit vector normal to the grating plane, a unit vector along the ruling direction, the diffraction order, the grating pitch, the refractive index, and the vacuum wavelength, respectively. In the figure, the vectors $\boldsymbol{\varepsilon}$ and $\boldsymbol{q}$ are the same as the unit vectors along the Z- and Y-axes, respectively. If the incident angle on the XZ plane is θ_{iXZ} ($\theta_{iXZ} \ll 1$), the $\pm$ 1st-order diffraction angles θ_{+1} and θ_{-1} on the XZ plane can be derived from

$$d(\sin\theta_{+1} - \sin\theta_{iXZ}) = +\lambda \, , \tag{3.2}$$

$$d(\sin\theta_{-1} - \sin\theta_{iXZ}) = -\lambda, \tag{3.3}$$

In these equations, we assume $n = 1$.

In Fig. 3.1, the interference fringe between the $\pm$1st-order diffraction light beams is formed on PD3 and PD4 via steering mirror1 (SM1), steering mirror2 (SM2), quarter-wave plate4 (QWP4), the beam splitter (BS), and PBS3. In this case, the quadrature phase shift of two interference signals can also be obtained with a phase difference of 90° (at PD3 0°, and PD4 90°). We assume that Δx, Δy, and Δz are the displacement shifts of the grating along the X-, Y-, and Z-axes, respectively. We also assume that the small incident angle θ_{iYZ} (θ_{iYZ} « 1) on the YZ plane and the small incident angle θ_{iz} (θ_{iz} « 1) between the incident light and the Z-axis affect the interference fringe. The phase shifts $\Delta\phi_{+1}$ and $\Delta\phi_{-1}$ of the $\pm$1st-order diffraction light due to the shifts ($\Delta x, \Delta y, \Delta z$) and the small incident angles (θ_{iXZ}, θ_{iYZ}) are written as

$$\phi_{+1} = \frac{2\pi}{\lambda}\{\Delta x \sin\theta_{+1} - \Delta z \cos\theta_{+1} + \Delta x \sin 2\theta_{iYZ} - \Delta z \cos 2\theta_{iYZ}\}, \tag{3.4}$$

$$\phi_{+1} = \frac{2\pi}{\lambda}\{\Delta x \sin\theta_{-1} - \Delta z \cos\theta_{-1} + \Delta x \sin 2\theta_{iYZ} - \Delta z \cos 2\theta_{iYZ}\}, \tag{3.5}$$

From Eqs. (3.4) and (3.5), the combined electrical field $E_{\pm 1}$ on PD2 is represented as

$$E_{\pm 1} = E_{+1} \exp i(\varphi_{+1} + \phi_{+1}) + E_{-1} \exp i(\varphi_{-1} + \phi_{-1}), \tag{3.6}$$

where E_{+1} and E_{-1} and φ_{+1} and φ_{-1} are the amplitudes and initial phases of the $\pm$1st-order diffraction electrical fields, respectively. From Eqs. (3.2) to (3.6), the interference light intensity $I_{\pm 1}(\Delta x, \Delta z)$ on PD3 and PD4 is

$$I_{\pm 1}(\Delta x, \Delta z) = E_{+1}^2 + E_{-1}^2 + 2E_{+1}E_{-1}\cos\{(\varphi_{+1} - \varphi_{-1})$$
$$+ \frac{2\pi}{\lambda}\Delta z(\cos\theta_{+1} - \cos\theta_{-1}) + \frac{4\pi}{d}\Delta x\}, \tag{3.7}$$

The interference light intensity $I_{fix0}(\Delta x, \Delta z)$ between the two light beams reflected from FM and the grating can be written in the same manner as

$$I_{fix0}(\Delta x, \Delta z) = E_{fix}^2 + E_0^2 + 2E_{fix}E_0 \cos\left\{\psi + \frac{4\pi}{\lambda}\left(\Delta z + \sqrt{\Delta x^2 + \Delta y^2}\,\tan 2\theta_{iZ}\right)\right.$$

$$\left. + L\left(1 - \sqrt{\tan^2 2\theta_{iYZ} + 1}\right)\right\} \tag{3.8}$$

where E_{fix}, E_0, ψ and L are the amplitudes of the lights reflected from FM, and the grating, the initial phase, and the distance between the grating and PD1 (or PD2), respectively. The last two terms in the cosine originate from the inclined wave front of the grating.

Equations (3.7) and (3.8) contain errors arising from the small incident angles θ_{iXZ} and θ_{iZ}. However, the contributions from θ_{iXZ} and θ_{iZ} can be neglected in the case of ultraprecise spindle measurements. If λ=633 nm, d=2 μm, θ_{iXZ}<10 arcsec and Δz<1 μm, then $\frac{2\pi}{\lambda}\Delta z(\cos\theta_{+1} - \cos\theta_{-1}) \leq 10^{-4}$ order. This value is the same as $|\Delta x| \leq 50$ pm; therefore, it can be neglected. For the conditions of (λ=633 nm, θ_{iZ}< 10 arcsec, $\sqrt{\Delta x^2 + \Delta y^2}$ < 1 μm and L=20 mm), the contributions from $\sqrt{\Delta x^2 + \Delta y^2}\,\tan 2\theta_{iZ}$ and $L\left(1 - \sqrt{\tan^2 2\theta_{iYZ} + 1}\right)$ in Eq. (3.8) are 90 pm and 90 pm, respectively; therefore, they can also be neglected. In case of ultraprecise spindle measurements, the radial ($\sqrt{\Delta x^2 + \Delta y^2}$), axial ($\Delta z$) and angular ($\theta_{iXZ}$ and θ_{iZ}) motion errors are less than 1 μm, 1 μm and 10 arcsec, respectively. Thus, the output signal (I_{PD1}, I_{PD2}, I_{PD3}, and I_{PD4}) from photodetector PD1, PD2, PD3, and PD4 can be expressed as follows:

$$I_{PD1} = E_{fix}^2 + E_0^2 + 2E_{fix}E_0 \cos\left(\frac{4\pi}{\lambda}\Delta z\right), \tag{3.9}$$

$$I_{PD2} = E_{fix}^2 + E_0^2 + 2E_{fix}E_0 \sin\left(\frac{4\pi}{\lambda}\Delta z\right), \tag{3.10}$$

$$I_{PD3} = E_{+1}^2 + E_{-1}^2 + 2E_{+1}E_{-1} \cos\left(\frac{4\pi}{d}\Delta x\right), \tag{3.11}$$

$$I_{PD4} = E_{+1}^2 + E_{-1}^2 + 2E_{+1}E_{-1}\sin\left(\frac{4\pi}{d}\Delta x\right),\qquad(3.12)$$

From Eqs. (3.9) to (3.12), we can obtain the Lissajous diagram from two reference signals with a phase difference of 90° [109]. Using the Lissajous diagram, the axial (Z-axis) and the radial (X-axis) motions of the grating can be calculated concurrently. In the optical sensor, to reduce the crosstalk error between the Michelson and grating interferometers down to 10^{-4} order, the grating plane must be aligned to be nearly parallel to the XY plane within an error of 10 arcsec [106]. To interpolate the unit periods of ($d/2$) and ($\lambda/2$) in Eqs. (3.9) and (3.10), some optical techniques can be used [114]. An interpolation order of 8000 or more is available in some commercial products of homodyne interferometers (SONY Manufacturing System, BD96series [115] and MicroE Systems, SP4800 [116]). A heterodyne technique [70] can also be applied to the proposed method. To reduce the distance L between gratings and PD1 (or PD2), compact-size optics can be applied.

3.2 Two-axes displacement-measuring interferometers using phase modulation technique

The optical sensor based on the phase modulation technique consists of a frequency-modulated laser diode as a light source and two-axes displacement measuring interferometers (Michelson and grating interferometers) with two photodetectors. The configuration of the optical sensor is shown in Fig. 3.2. To obtain displacements (Lissajous diagram), we apply the sinusoidal phase modulation techniques to the light source of LD [117-119]. We use the frequency modulation of LD. The sinusoidal angular modulation frequency is ω_m. The Michelson interferometer detects an interference fringe between the reflected light from a fixed mirror (FM) and the 0th-order diffraction light from the grating. In this case, a light beam emitted from the laser diode is incident on polarized beam splitter 1 (PBS1) and is divided into two beams. The first beam reflected from PBS1 reach the fixed mirror (FM) via quarter-wave plate 1 (QWP1) and propagates from FM and reaches avalanche photodetector 1 (APD1) via PBS1 and polarizer 1 (P1). The second beam, which passes through PBS1, reaches the concentric circle grating via QWP2. In Fig. 3.2, we assume that the incident angle θ_i of the second beam to the grating is almost nulls. Thus, the reflected light (which is 0th-order diffraction light) reaches APD1 via QWP2, PBS1, and P1. At APD1, it is possible to detect an interferometer fringe between the reflection

light from FM and the grating, and to measure the displacement along the Z-axis of the grating. Another interferometer (a grating interferometer) observes an interference fringe between +2nd and -2nd-order diffraction lights from the concentric circle grating.
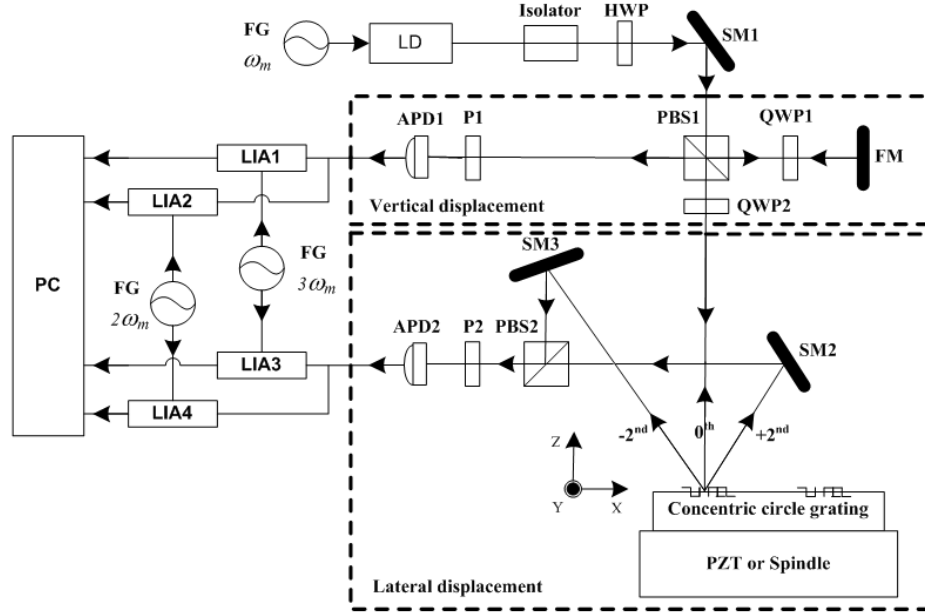
Fig.3.2 Schematic diagram of two-axes displacement measuring interferometers using phase modulation technique. LD: laser diode; SM: steering mirror; FM: fixed mirror; HWP: half-wave plate; QWP: quarter-wave plate; PBS: polarized beam splitter; P: polarizer; APD: avalanche photodetector; LIA: lock-in amplifier; FG: function generator; PC: personal computer.

We use +2nd and -2nd-order diffraction light, because they are stronger than the diffraction light of other orders. In this case, the +2nd and -2nd-order diffraction light from the grating through steering mirrors 2 and 3 (SM2 and SM3) reaches avalanche photodetector 2 (APD2) via PBS2 and polarizer 2 (P2). If the incident angle on the XZ plane is negligible, the $\pm$ 2nd-order diffraction angles θ_{+2} and θ_{-2} (on XZ plane) can be derived as

$$d(\sin\theta_{+2} - \sin\theta_{iXZ}) = +2\lambda , \qquad (3.13)$$

$$d(\sin\theta_{-2} - \sin\theta_{iXZ}) = -2\lambda , \qquad (3.14)$$

21

where d is the grating pitch and λ is the wavelength of the light source. In Fig. 3.2, we assume that Δz and Δx are the displacement shifts of the grating along the Z-axis and X-axis, respectively. The observed light intensities of I_{0F} and $I_{\pm 2}$ at APD1 and APD2 are represented as

$$I_{0F} = |E_0|^2 + |E_F|^2 + 2E_0 E_F \cos\left\{\varphi_{\text{int},0} - \frac{4\pi n}{c} f\left(L_{\text{int}} + \Delta z\right)\right\}, \qquad (3.15)$$

$$I_{\pm 2} = |E_{+2}|^2 + |E_{-2}|^2 + 2E_{+2} E_{-2} \cos\left\{\varphi_{\text{int},\pm 2} - \frac{2\pi n}{c} f L_{\pm 2} - \frac{8\pi}{d} \Delta x\right\}, \qquad (3.16)$$

where E_0, E_F, E_{+2}, E_{-2}, $\varphi_{\text{int},0}$, $\varphi_{\text{int},\pm 2}$, n, c, f, L_{int} and $L_{\pm 2}$ are the amplitudes of the lights reflected from 0th order diffraction of the grating and FM, the amplitudes of the lights diffracted from the $\pm$2nd-order of the grating, the initial phase of Michelson interferometer, the initial phase of the grating interferometer, the refractive index of air, the speed of light, the frequency of the light source, the optical path difference between the Michelson interferometer arms, and the optical path difference of grating interferometer arms, respectively. In the system, the vertical displacement Δz is assumed to be of the same order as the wavelength of the LD (i.e., $\Delta z \sim \lambda$). We add a small modulation to the frequency of LD as

$$f = f_0 + \Delta f, \qquad (3.17)$$

where f_0 and Δf are the center frequency and modulation, respectively. We assume

$$\frac{\Delta f}{f_0} \ll 1 \, (\frac{\Delta \lambda}{\lambda} \ll 1), \qquad (3.18)$$

where $\Delta \lambda$ is the wavelength modulation. In Eq. (3.15), the 2nd term in the bracket can be calculated as

$$\frac{4\pi n}{c}\left(f_0 + \Delta f\right)\left(L_{\text{int}} + \Delta z\right) = \frac{4\pi n}{c} f_0 \left(L_{\text{int}} + \Delta z\right) + \frac{4\pi n}{c} L_{\text{int}} \Delta f - \frac{4\pi n}{\lambda^2} \Delta\lambda\Delta z . \qquad (3.19)$$

The order of the last term of the Eq. (3.19) is

$$\left| -4\pi n \frac{\Delta\lambda}{\lambda}\frac{\Delta z}{\lambda} \right| \sim \left| \frac{4\pi n}{c}\frac{\Delta\lambda}{\lambda} \right| \ll 1 . \qquad (3.20)$$

Therefore, the Eq. (3.15) can be represented as

$$I_{0F} = \left|E_0\right|^2 + \left|E_F\right|^2 + 2E_0 E_F \cos\left\{ \varphi_{\text{int},0} - \frac{4\pi}{c} nL_{\text{int}} f_0 - \frac{4\pi}{c} nf_0\Delta z - \frac{4\pi}{c} nL_{\text{int}}\Delta f \right\}$$

$$= \left|E_0\right|^2 + \left|E_F\right|^2 + 2E_0 E_F \cos\left\{ \varphi_0' - \frac{4\pi}{c} nf_0\Delta z - \frac{4\pi}{c} nL_{\text{int}}\Delta f \right\} . \qquad (3.21)$$

where φ_0' $\left(= \varphi_{\text{int},0} - \dfrac{4\pi}{c} nL_{\text{int}} f_0\right)$ is the initial phase of Michelson interferometer. We add the

sinusoidal modulation to $\left(-\dfrac{4\pi}{c} nL_{\text{int}}\Delta f\right)$ using

$$-\frac{4\pi}{c} nL_{\text{int}}\Delta f = k_{m,0} \sin\omega_m t , \qquad (3.22)$$

where $k_{m,0}$ is the modulation depth of Michelson interferometer. By combining Eqs. (3.21) and (3.22), we obtain

$$I_{0F} = \left|E_0\right|^2 + \left|E_F\right|^2 + 2E_0 E_F \cos\left\{ \varphi_0' - \frac{4\pi}{c} nf_0\Delta z + k_{m,0}\sin\omega_m t \right\}$$

$$= \left|E_0\right|^2 + \left|E_F\right|^2 + 2E_0 E_F \left[\cos\left(\varphi_0' - \frac{4\pi}{c} nf_0\Delta z \right)\cos\left(k_{m,0}\sin\omega_m t \right)\right.$$

$$\left. -\sin\left(\varphi_0' - \frac{4\pi}{c} nf_0\Delta z \right)\sin\left(k_{m,0}\sin\omega_m t \right) \right] . \qquad (3.23)$$

Equation (3.23) can be rewritten using the Bessel function from the following formulas:

$$\cos(x\sin\theta) = J_0(x) + 2\sum_{m=1}^{\infty} J_{2m}(x)\cos 2m\theta , \qquad (3.24)$$

$$\sin(x\sin\theta) = 2\sum_{m=1}^{\infty} J_{2m+1}(x)\{\sin(2m+1)\theta\} , \qquad (3.25)$$

where J_m is the Bessel coefficient of order m. Using the Bessel function (see Appendix B) of Eqs. (3.24) and (3.25), we obtain

$$I_{0F} = |E_0|^2 + |E_F|^2 + 2E_0 E_F \left[\cos\left(\varphi_0' - \frac{4\pi}{c}nf_0\Delta z\right)\left\{J_0(k_{m,0}) + 2\sum_{m=1}^{\infty} J_{2m}(k_{m,0})\cos 2m\omega_m t\right\} \right.$$

$$\left. - \sin\left(\varphi_0' - \frac{4\pi}{c}nf_0\Delta z\right)\left\{2\sum_{m=1}^{\infty} J_{2m+1}(k_{m,0})\sin(2m+1)\omega_m t\right\} \right]. \qquad (3.26)$$

In order to reduce the effect of the amplitude modulation of LD, we select the 2nd-harmonic ($2\omega_m$) and 3rd-harmonic ($3\omega_m$). We apply the reference signal of the 2nd-harmonic cosine wave ($2\omega_m$) and the reference signal of the 3rd-harmonic sine wave ($3\omega_m$) to the lock-in detection signal of the interference light intensity I_{0F}. When the interference light intensity I_{0F} from Eq. (3.26) is synchronized by lock-in amplifier 1 (LIA1) with the reference signal of the 3rd-harmonic sine wave ($3\omega_m$), and lock-in amplifier 2 (LIA2) with the reference signal of the 2nd-harmonic cosine wave ($2\omega_m$) (see Fig. 2), the two signals of LIA1 and LIA2 can be written as

$$I_{0F}(3\omega_m) = -2E_0 E_F J_3(k_{m,0})\sin\left(\varphi_0' - \frac{4\pi}{c}nf_0\Delta z\right), \qquad (3.27)$$

$$I_{0F}(2\omega_m) = 2E_0 E_F J_2(k_{m,0})\cos\left(\varphi_0' - \frac{4\pi}{c}nf_0\Delta z\right), \qquad (3.28)$$

where $J_2\left(k_{m,0}\right)$ and $J_3\left(k_{m,0}\right)$ are Bessel functions of the 2nd and 3rd-order, respectively. For the interference light intensity $I_{\pm2}$ of the $\pm$ 2nd-order diffraction at APD2 which is obtained by Eq. (3.16), when a small modulation to the frequency of LD from Eq. (3.17) is added to the interferometer, Eq. (3.16) can be represented as

$$I_{\pm2} = \left|E_{+2}\right|^2 + \left|E_{-2}\right|^2 + 2E_{+2}E_{-2}\cos\left\{\varphi_{\text{int},\pm2} - \frac{2\pi}{c}nL_{\pm2}f_0 - \frac{2\pi}{c}nL_{\pm2}\Delta f - \frac{8\pi}{d}\Delta x\right\}$$

$$= \left|E_{+2}\right|^2 + \left|E_{-2}\right|^2 + 2E_{+2}E_{-2}\cos\left\{\varphi'_{\pm2} - \frac{8\pi}{d}\Delta x - \frac{2\pi}{c}nL_{\pm2}\Delta f\right\}. \tag{3.29}$$

where $\varphi'_{\pm2}$ $(= \varphi_{\text{int},\pm2} - \frac{2\pi}{c}nL_{\pm2}f_0)$ is the initial phase of grating interferometer. We add the sinusoidal modulation to $(-\frac{2\pi}{c}nL_{\pm2}\Delta f)$ using

$$-\frac{2\pi}{c}nL_{\text{int}}\Delta f = k_{m,\pm2}\sin\omega_m t, \tag{3.30}$$

where $k_{m,\pm2}$ is the modulation depth of grating interferometer. By combining Eqs. (3.29) and (3.30), we obtain

$$I_{\pm2} = \left|E_{+2}\right|^2 + \left|E_{-2}\right|^2 + 2E_{+2}E_{-2}\cos\left\{\varphi'_{\pm2} - \frac{8\pi}{d}\Delta x + k_{m,\pm2}\sin\omega_m t\right\}$$

$$= \left|E_{+2}\right|^2 + \left|E_{-2}\right|^2 + 2E_{+2}E_{-2}\left[\cos\left(\varphi'_{\pm2} - \frac{8\pi}{d}\Delta x\right)\cos\left(k_{m,\pm2}\sin\omega_m t\right)\right.$$

$$\left. -\sin\left(\varphi'_{\pm2} - \frac{8\pi}{d}\Delta x\right)\sin\left(k_{m,\pm2}\sin\omega_m t\right)\right]. \tag{3.31}$$

Using the Bessel function (see Appendix B) of Eqs. (3.24) and (3.25), we obtain

$$I_{\pm2} = \left|E_{+2}\right|^2 + \left|E_{-2}\right|^2 + 2E_{+2}E_{-2}\left[\cos\left(\varphi'_{\pm2} - \frac{8\pi}{d}\Delta x\right)\left\{J_0\left(k_{m,\pm2}\right) + 2\sum_{m=1}^{\infty}J_{2m}\left(k_{m,\pm2}\right)\cos2m\omega_m t\right\}\right.$$

$$-\sin\left(\varphi'_{\pm2}-\frac{8\pi}{d}\Delta x\right)\left\{2\sum_{m=1}^{\infty}J_{2m+1}\left(k_{m,\pm2}\right)\sin\left(2m+1\right)\omega_m t\right\}\right]. \qquad (3.32)$$

When the interference light intensity $I_{\pm2}$ from Eq. (3.32) is synchronized by lock-in amplifier 3 (LIA3) with the reference signal of the 3rd-harmonic sine wave ($3\omega_m$), and by lock-in amplifier 4 (LIA4) with the reference signal of 2nd-harmonic cosine wave ($2\omega_m$) (see figure 3.2), the two signals of LIA3 and LIA4 can be written as

$$I_{\pm2}\left(3\omega_m\right)=-2E_{+2}E_{-2}J_3\left(k_{m,\pm2}\right)\sin\left(\varphi'_{\pm2}-\frac{8\pi}{d}\Delta x\right), \qquad (3.33)$$

$$I_{\pm2}\left(2\omega_m\right)=2E_{+2}E_{-2}J_2\left(k_{m,\pm2}\right)\cos\left(\varphi'_{\pm2}-\frac{8\pi}{d}\Delta x\right), \qquad (3.34)$$

where $J_2\left(k_{m,\pm2}\right)$ and $J_3\left(k_{m,\pm2}\right)$ are Bessel functions of the 2nd- and 3rd-order, respectively. From Eqs. (3.27), (3.28), (3.33) and (3.34), we can obtain the Lissajous diagram from two reference signals with a phase difference of 90° [113]. Using the Lissajous diagram, the axial (Z-axis) and radial (X-axis) motion of the grating can be calculated concurrently. In the optical sensor, to reduce the crosstalk error between the Michelson and grating interferometers with accuracy of 10^{-4} order are required, the grating plane must also be aligned to be nearly parallel to the XY plane within an error of 10 arcsec [106].

Chapter 4

Spindle motion measurement using quadrature detection technique

This chapter describes the instrumentations and the measurement results of spindle motion when we apply the quadrature detection technique to the measurement system. The performance of the Michelson and grating interferometers, and the compact-size optical sensor is evaluated. The measurement of five degrees of freedom spindle motion is carried out. The effects of the crosstalk error on the Michelson and grating interferometers are also discussed in this chapter.

4.1 Instrumentations
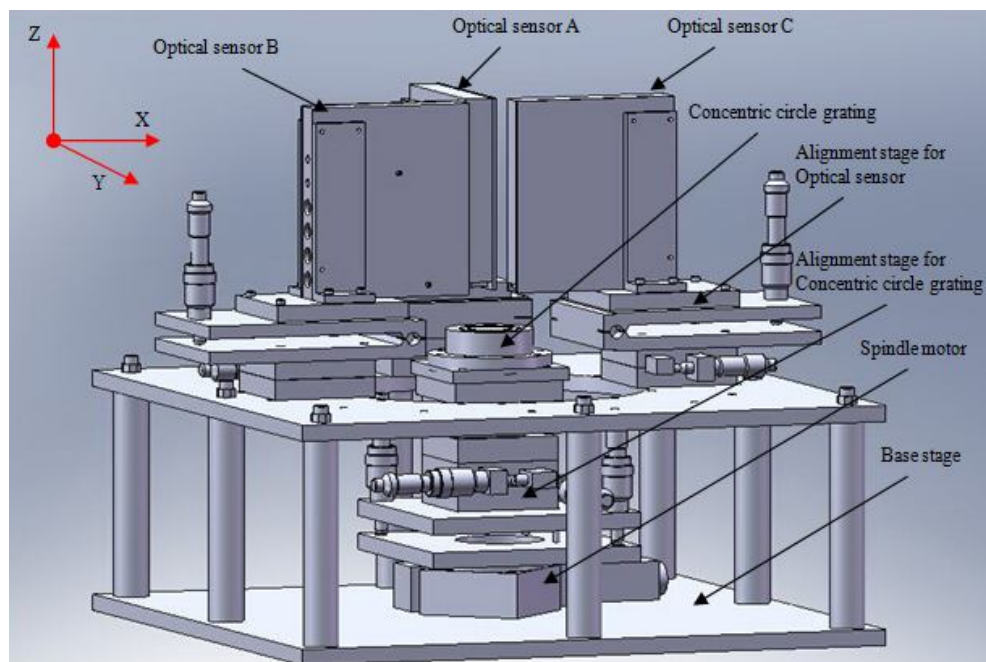
Fig. 4.1 Prototype instrument for spindle motion measurement

Chapter4 – Spindle motion measurement using quadrature detection technique

The prototype instrument for spindle motion measurement system using three optical sensors and a concentric circle grating with the quadrature detection technique is shown in Fig. 4.1. The measurement system consists of four main parts, which are;

1) Alignment system for the concentric circle grating

2) Optical sensor

3) Spindle motor

4) Recording data system

1) Alignment system for the concentric circle grating

The prototype instrument for the spindle motion error measurement system using three optical sensors and a concentric circle grating, as shown in Fig. 4.1 consists of three optical sensors A, B and C, a concentric circle grating, an aliment stage for the optical sensor, an alignment stage for the concentric circle grating, and a base stage. All parts are set up on the base stage. The dimensions of the base stage are 350 mm (W) × 350 mm (L) × 149 mm (H). The alignment stage can be separated into two parts: the alignment stage for the optical sensors, and the alignment stage for the concentric circle grating. The alignment stage for the optical sensors consists of one axis translation stage (along the X-axis or Y-axis) and one angle-tilting stage. Three optical sensors are attached to the alignment stage for the optical sensors on the base stage, and it is located above the concentric circle grating. The distance between the grating surface and the optical sensor is approximately 10 mm. The detection area of each optical sensor is adjusted until it is close to the concentric circle grating area. Optical sensor A is located along the Y-axis for measurement of the Y-axis and Z-axis displacement. Optical sensors B and C are located along the X-axis for measurement of the X-axis and Z-axis displacement. The concentric circle grating and its alignment stage are set up on the spindle motor. The spindle rotation center must be aligned to the center of the concentric grating within an accuracy of 1 μm or less. The grating plane must also be aligned to be parallel to the XY plane within an accuracy of 10 arcsec.

2) Optical sensor

The compact-size optical sensor was fabricated for performing five degrees of freedom spindle motion measurement. The optical sensor consists of laser diode, optics, and photodetectors, which are shown in Fig. 4.2. All parts are assembled in the optical sensor box. Specifications of the laser diode and photodiode used in the optical sensor are shown in tables 4.1 and 4.2, respectively. The laserdiode (Edmund Optics, model: NT83-

824) is used as the light source. The optics, which include a polarized beam splitter (PBS), quarter-wave plate (QWP), fixed mirror (FM), and steering mirror (SM) are set up on the optics plate. The photodetector is used to detect the intensity of interference light. A photoelectric current-voltage conversion circuit using the low-noise photodiode is created. Figure 4.3 shows the circuit diagram of the photodetector.
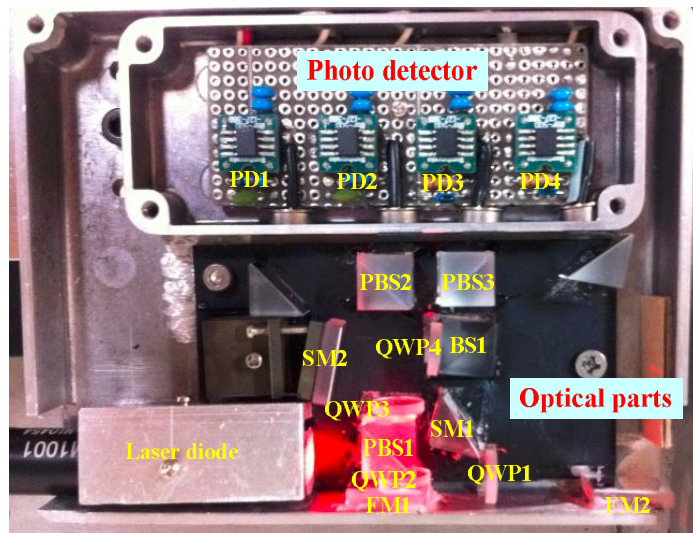
Fig. 4.2 Photograph of the prototype optical sensor

In the photodiode the flow of the signal current is proportional to the incoming light quantity, and the photoelectric current-voltage conversion circuit converts current into voltage. In this system, the operation amplifier (Op-Amp) is OPA129 UB from BURR-BROWN Company, and the photodiode is a Si photo diode model S1266-5SB. The optical receiver sensitivity is 0.36 A/W and the maximum amount of light received is approximately 40 µW from the operation amplifier. The frequency bandwidth (f_b) is given as follows:

$$f_b = \frac{1}{2\pi R_f C_f},$$ (4.1)

where R_f is the resistance value, and C_f is the capacitance value.

If R_f= 1 MΩ and C_f= 1 pF, then

$$f_b = \frac{1}{2\pi R_f C_f} = \frac{1}{2\pi \times 1 \times 10^6 \times 1 \times 10^{-12}} = 159.15 \text{kHz.} \qquad (4.2)$$

In this circuit, the frequency bandwidth is approximately 159 kHz, which is suitable for a high-speed spindle motor.
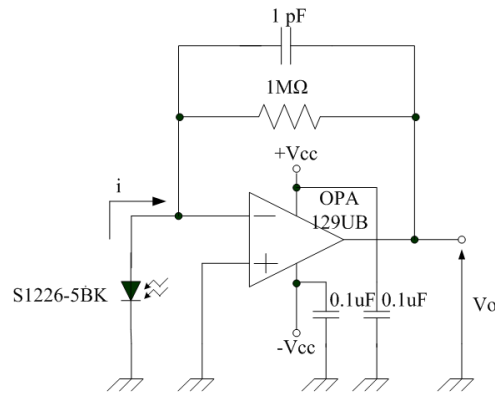
Fig. 4.3 Circuit diagram of photodetector

Table 4.1 Specifications of laser diode (Edmund Optics, model: NT83-824)

Wavelength	635	[nm]
Input voltage (DC)	5	[V]
Input current	80	[mA]
Output power	4.5	[mW]
Beam diameter (ellipse)	2×3	[mm]
Beam divergence	2	[mrad]
Pointing accuracy	0.02 - 0.05	[mrad]
Diameter × Length	0.5×2.1	[inches]
Wavelength stability	0.2 - 0.3	[nm/°C]
Power stability	±2	[%]

Table 4.2 Specifications of photodiode (HAMAMATSU, model: S1226-5BK)

Spectral response range	320-1000	[nm]
Peak sensitivity wavelength	720	[nm]
Photosensitivity	0.36	[A/W]
Detection area	2.4×2.4	[mm]

3) Spindle motor

The spindle motor (CHUO SEIKI, model: ARS-636-HM [120]) is used as the device under test when evaluating the rotation error of the spindle in this experiment and is shown in Fig. 4.4. The spindle motor is set up with the alignment stage for the concentric circle grating. To evaluate the performance of the optical sensor, the spindle motor is rotated at a low speed. In the experimental system, the spindle motor is rotated at a speed of 4 rpm. Specifications of the spindle motor used for themeasurement of spindle error motions are shown in Table 4.3.

Fig. 4.4 Spindle motor under test

Table 4.3 Specifications of spindle motor (CHO SEIKI, model: ARS-636-HM)

Diameter of motor stage	60	[mm]
Angle resolution	0.008	[Degree]
Repeatability accuracy	±0.005	[Degree]
Accuracy of position	0.2	[Degree]
Radial motion	0.03	[mm]
Axial motion	0.06	[mm]
Maximum speed	40	[Degree/sec]
Maximum load	39.2	[N]
Weight	0.8	[kg]

4) Recording data system

Data acquisition is the process of measuring parameters such as voltage, current, temperature, pressure, and sound. The data acquisition system has a unique functionality to

serve the application-specific requirements of all systems which share common components that include sensors, data acquisition hardware, and a computer. In this thesis, data acquisition is used for the conversion of an analog signal from the photodetector to a digital signal (A/D converter). A data acquisition card (National Instrument, model: NI PCI-622, M series) is used for connecting the signal output from the photodetectors throughout the connector block (National Instrument, model: NI BNC-2111) to a personal computer (PC) with two 16-bit analog outputs (833 kS/s) and 32-bit counters [121]. For measurement of five degrees of freedom spindle motion, 12 input ports are required in the connector block for transferring data to the PC.
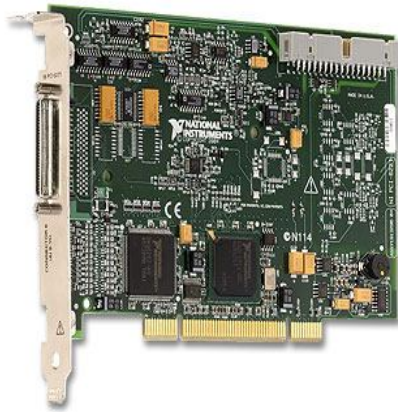
Fig. 4.5 Data acquisition card (model: NI PCI-6221)

Fig. 4.6 Connector block (model: NI BNC-2111)

4.2 Evaluation of the performance of two-axes displacement-measuring interferometers using quadrature detection technique
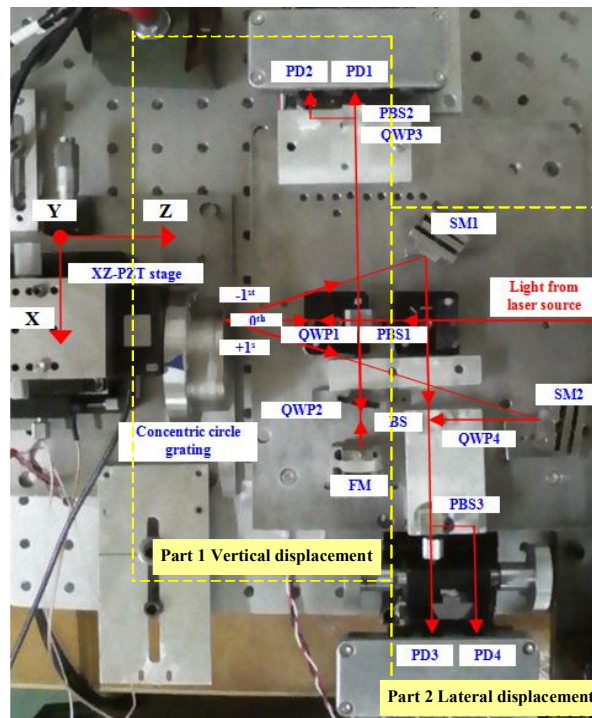
Fig. 4.7 Experimental setup for evaluation of the two-axes displacement measuring interferometer using the quadrature detection technique

To verify Eqs. (3.9) to (3.12) in chapter 3, we fabricated the grating interferometers as shown in Fig. 4.7. In the experiment, the concentric circle grating with a pitch of 2 μm is set up on the XZ-PZT stage. Tables 4.4 and 4.5 show the specifications of the Z-axis PZT stage and the X-axis PZT stage, respectively. A laser diode (wavelength = 635 nm) is used with the interferometer as a light source. Photodetectors PD1 and PD2 detect the interference signal of axial motion when the PZT stage is moved along the Z-axis. Photodetectors PD3 and PD4 detect the interference signal of radial motion when the PZT stage is moved along the X-axis. Table 4.6 shows the measurement conditions applied to the XZ-PZT stage. For the axial (Z-axis) motion, the two interference signals have a phase shift of 90 degrees with respect to each after passing through a series of polarizing beam splitters (PBS1 and PBS2) and quarter-wave plate (QWP1, QWP2, and QWP3) which are

33

detected by PD1 and PD2. For the radial (X-axis) motion, the two interference signals have a phase shift of 90 degrees with respect to each other after passing through a series of beam splitters (BS), a quarter-wave plate (QWP4) and a polarized beam splitter (PBS3), which are detected by PD3 and PD4. The two phase interference signals are recorded using an oscilloscope.

Table 4.4 Specifications of Z-axis PZT stage (Piezosystem Jena, model: PZ 100)

Maximum range	100	[μm]
Resolution	0.2	[nm]
Compressive force / Tension force	77 / 8	[N]
Weight	85	[g]
Output voltage	-20 - +150	[μm]
Frequency	DC ~ 100	[kHz]
Gain	x15	[time]

Table 4.5 Specifications of X-axis PZT stage (PI, model: P750, 20)

Maximum range	75	[μm]
Resolution	1	[nm]
Compressive force / Tension force	800 / 100	[N]
Weight	2.6	[kg]
Output voltage	-20 - +150	[μm]
Frequency	DC ~ 100	[kHz]
Gain	x15	[time]

Table 4.6 Measurement conditions applied to the XZ-PZT stage motion

Laser diode wavelength	635	[nm]
Amplitude applied to XZ-PZT stage	1.3	[μm]
Frequency applied to XZ-PZT stage	1	[Hz]
Motion shape	Triangular	
Sampling rate	1	[kHz]

(a) Phase quadrature interference signal

(b) Lissajous diagram

Fig. 4.8 Phase quadrature interference signal and Lissajous diagram of the axial (Z-axis) motion
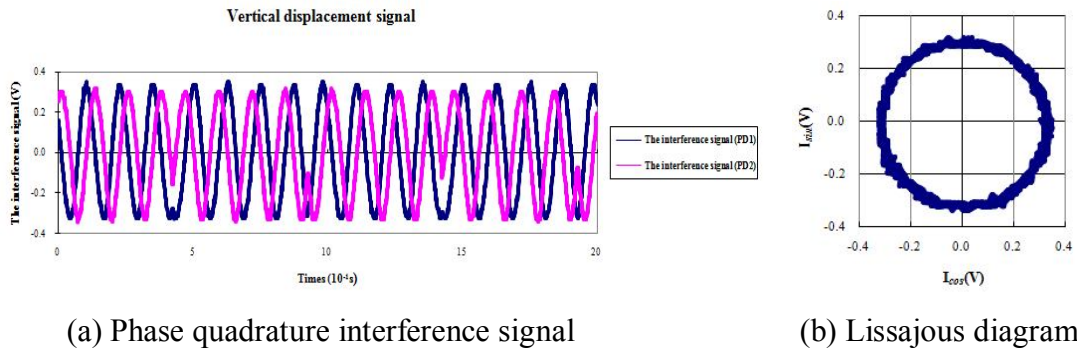
(a) Phase quadrature interference signal

(b) Lissajous diagram
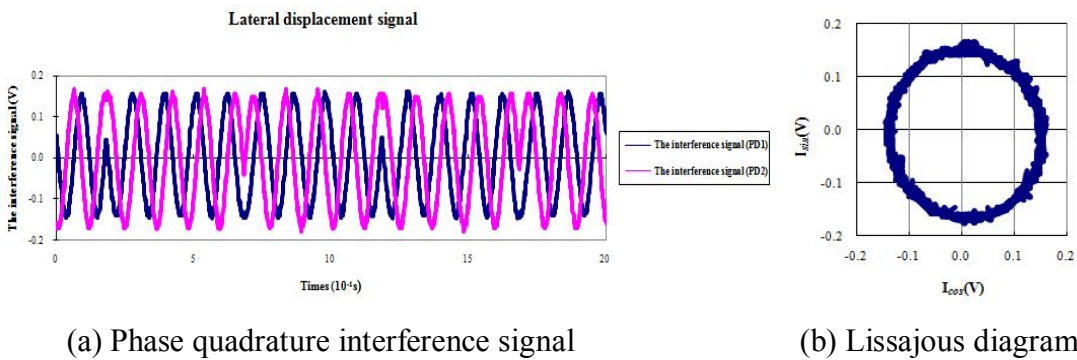
Fig. 4.9 Phase quadrature interference signal and Lissajous diagram of the radial (X-axis) motion

Figures 4.8 and 4.9 respectively show the phase quadrature interference fringe signal and Lissajous diagram of the axial (Z-axis) and radial (X-axis) motion. The axial (Z-axis) and radial (X-axis) motion of the XZ-PZT stage are shown in Figs. 4.10 and 4.11, respectively. The axial (Z-axis) and radial (X-axis) motions of the XZ-PZT stage are approximately 1.3 μm and 1.4 μm, respectively. The experimental results show that using the proposed method we can measure the displacement of the grating by interpolation of the fringe. It is possible to fabricate a compact-size optical sensor for spindle motion measurement.
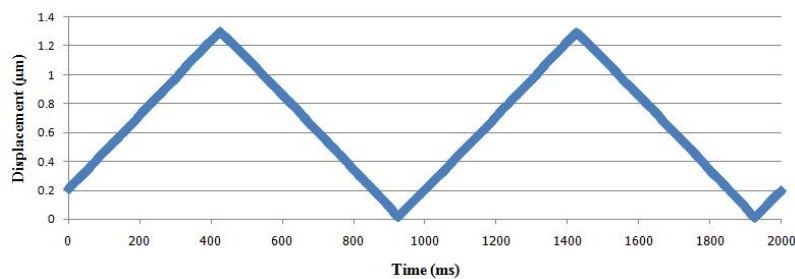
Fig. 4.10 Axial (Z-axis) motion of XZ-PZT stage
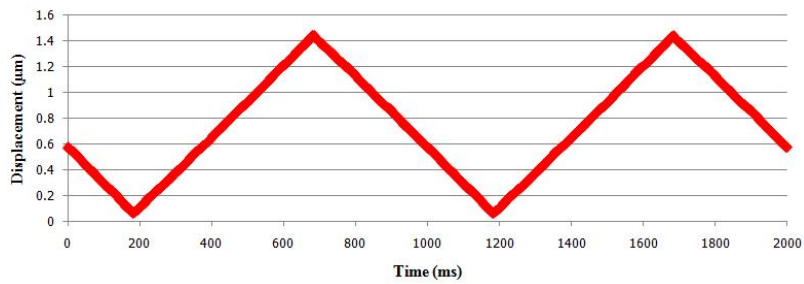
Fig. 4.11 Radial (X-axis) motion of XZ-PZT stage

4.3 Crosstalk error estimation

The experimental setup for crosstalk error measurement is shown in Fig. 4.7. The crosstalk error of the X-axis in Fig. 4.12 is obtained when the XZ-PZT stage is moved along the Z-axis, and can be observed from photodetectors PD3 and PD4. The crosstalk error of the X-axis is estimated to be approximately 630 nm. The crosstalk error of the Z-axis shown in Fig. 4.13 is obtained the XZ-PZT stage is moved along the X-axis, and it can be observed photodetectors PD1 and PD2. The crosstalk error of the Z-axis is estimated to be approximately 580 nm. The crosstalk errors occur, when the inclination angle between the grating plane and the incident light is not null. To reduce the crosstalk error, the grating plane must be aligned until it is perpendicular to the incident light from the light source.

To estimate the term of the crosstalk error from Eqs. (3.7) and (3.8) given in chapter 3 for ultraprecision spindle measurements, we have plot to a graph showing the relationship between Δz and Δx due to the incident angle change, which is shown in Fig. 4.14. The crosstalk error can be neglected when the incident angle is less than 10 arcsec.
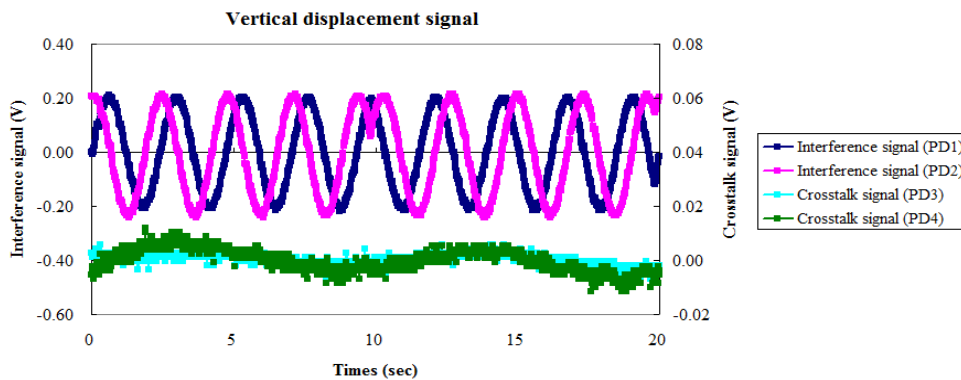
Fig. 4.12 Crosstalk error from the X-axis stage motion
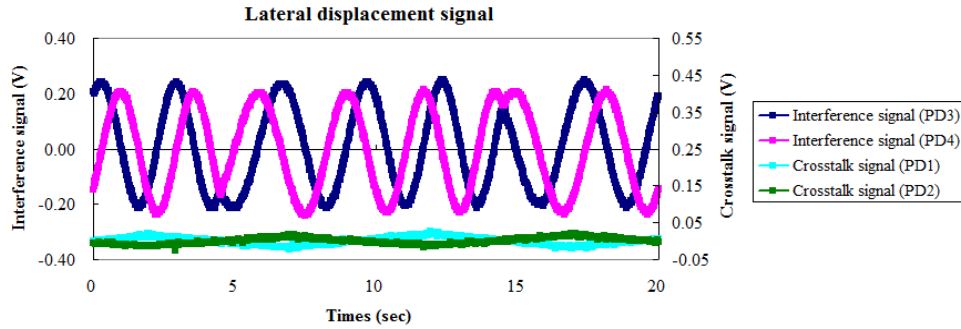
Fig. 4.13 Crosstalk error from the Z-axis stage motion
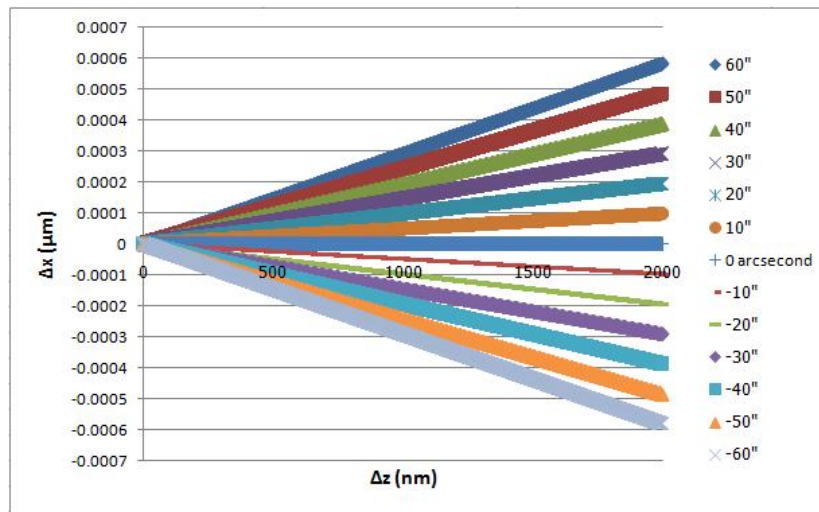
Fig. 4.14 Relationship between Δz and Δx due to the incident angles

4.4 Evaluation of the performance of the optical sensor using quadrature detection technique

The experimental setup for evaluation of the performance of the optical sensor using the quadrature detection technique is shown in Fig. 4.15. The concentric circle grating with a pitch of 2 μm is set up on the XZ-PZT stage. The optical sensor measures the axial (Z-axis) and radial (X-axis) motion of the XZ-PZT stage. Photodetectors PD1 and PD2 detect the interference signal of the axial (Z-axis) motion from the 0th-order diffraction of the grating. Photodetectors PD3 and PD4 detect the interference signal of the radial (X-axis) motion from the ±1st-order diffraction of the grating. The measurement conditions applied to the XZ-PZT stages are given Table 4.6.
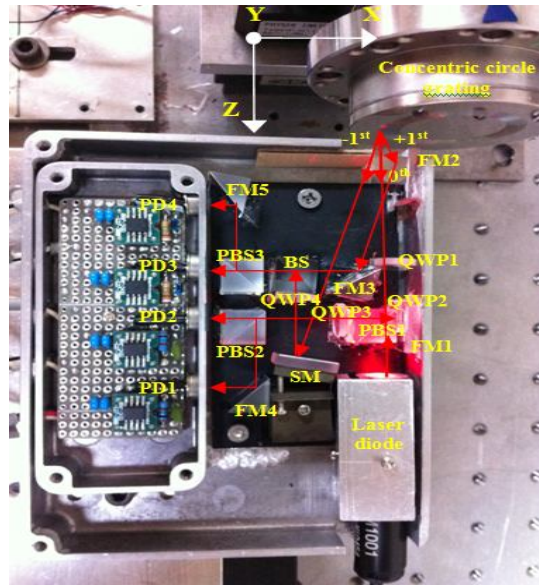
Fig. 4.15 Experimental setup for evaluation of optical sensor using the quadrature detection technique

(a) Phase quadrature interference signal   (b) Lissajous diagram
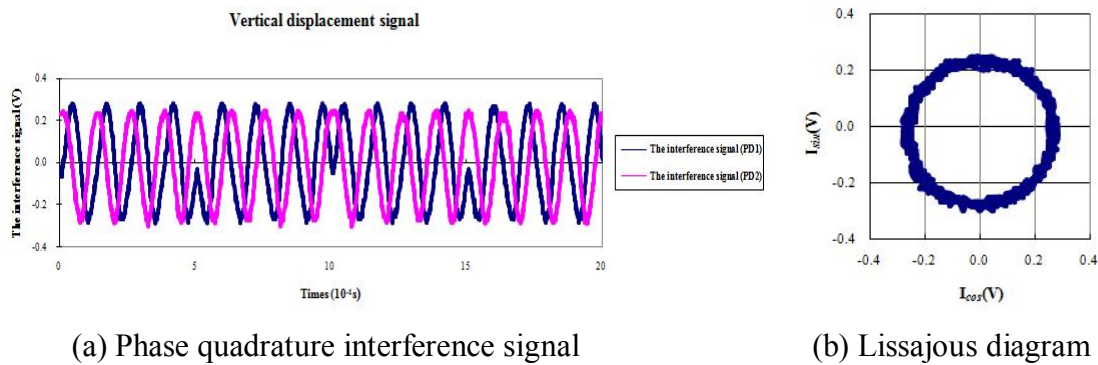
Fig. 4.16 Phase quadrature interference signal and Lissajous diagram of the axial (Z-axis) motion

(a) Phase quadrature interference signal   (b) Lissajous diagram
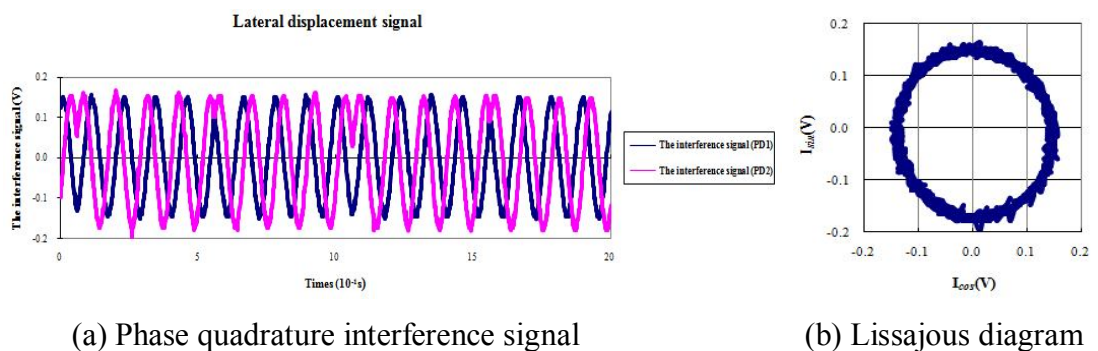
Fig. 4.17 Phase quadrature interference signal and Lissajous diagram of the radial (X-axis) motion

Figures 4.16 and 4.17 show the phase quadrature interference fringe signal and Lissajous diagram of the axial (Z-axis) and radial (X-axis) motion, respaxtively. The axial (Z-axis) and radial (X-axis) motions of the XZ-PZT stage are shown in Figs. 4.18 and 4.19, respectively. The axial (Z-axis) and radial (X-axis) motion of the XZ-PZT stage are approximately 1.3 μm and 1.4 μm, respectively. The experimental results show that the compact-size optical sensor can measure the displacement of the XZ-PZT stage motion. We can apply three compact size-optical sensors for the concurrent measurement of radial, axial, and angular motions of the spindle.
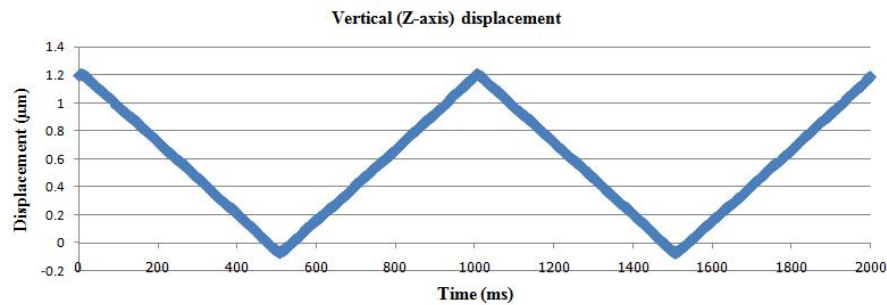
Fig. 4.18 Axial (Z-axis) motion of PZT-stage
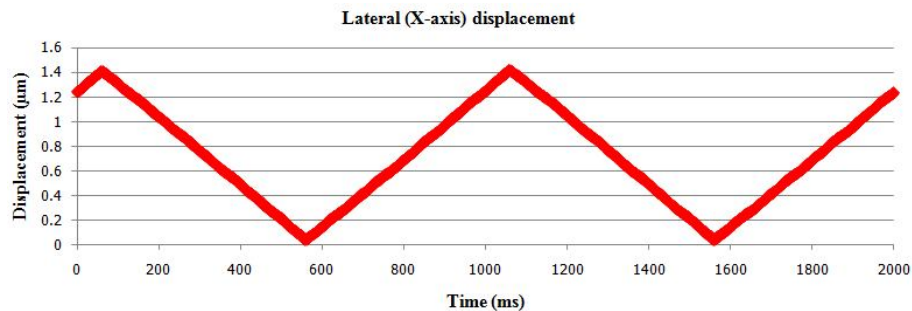
Fig. 4.19 Radial (X-axis) motion of PZT-stage

4.5 Concurrent measurement of spindle motion using three optical sensors and quadrature detection technique

The experimental setup for the concurrent measurement of spindle motion using three optical sensors and the quadrature detection technique is shown in Fig. 4.20. In the experiment, three optical sensors are set up above the concentric circle grating and measure the axial (Z-axis) and radial (X-axis) motion while the spindle motor is rotated at a speed of 4 rpm. Photodetectors PD1 and PD2 in the optical sensor observe the interference signal of axial (Z-axis) motion and photodetectors PD3 and PD4 in the optical sensor observe the

interference signal of radial (X-axis) motion. The measurement data is recorded in the PC through the data acquisition device (DAQ). The capacitive sensor is used for the measurement of the spindle radial motion, which can be compared to the measurement results of the optical sensor. Table 4.7 shows the measurement conditions applied to the spindle motion.
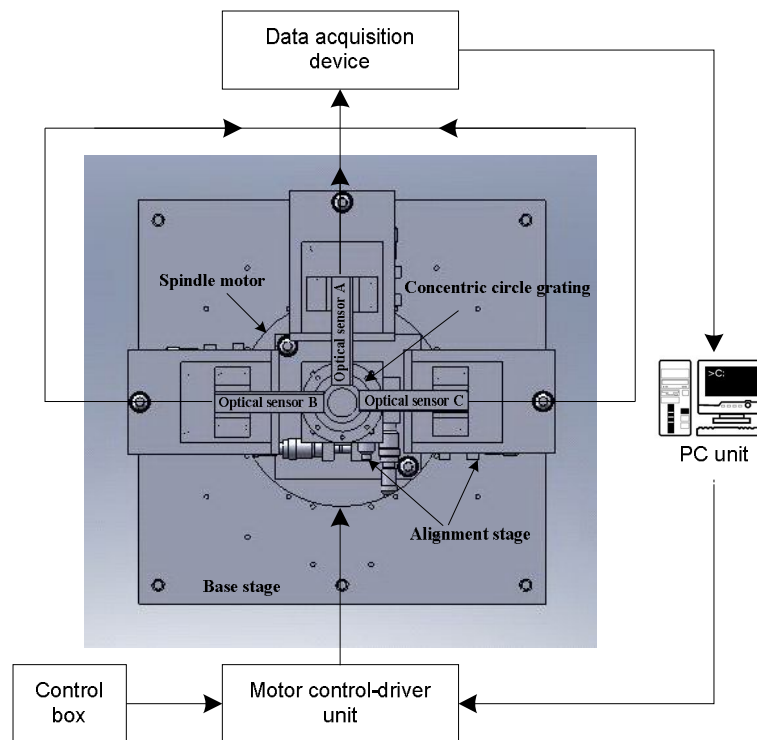
(a) Schematic diagram of the concurrent measurement of spindle motion
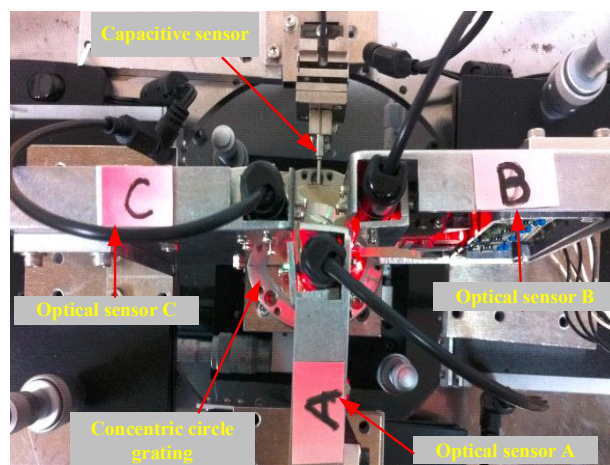
(b) Photograph of the experimental setup from the top view
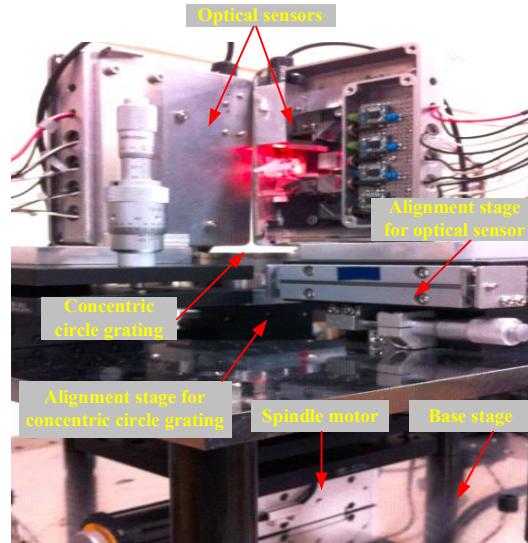
(c) Photograph of the experimental setup from the side view

Fig. 4.20 Experimental setup for the concurrent measurement of spindle motion using three optical sensors and the quadrature detection technique

Table 4.7 Measurement conditions applied to the spindle motion

Revolution speed of spindle	4	[rpm]
Number of rotations	3	[rotations]
Sampling rate	100	[Hz]

Figure 4.21 (a) and (b) shows the measurement results and the polar plot of the radial motion error of spindle motion respectively, using a capacitive sensor. The radial motion error, including the artifact form error, is estimated to be approximately 2 μm.
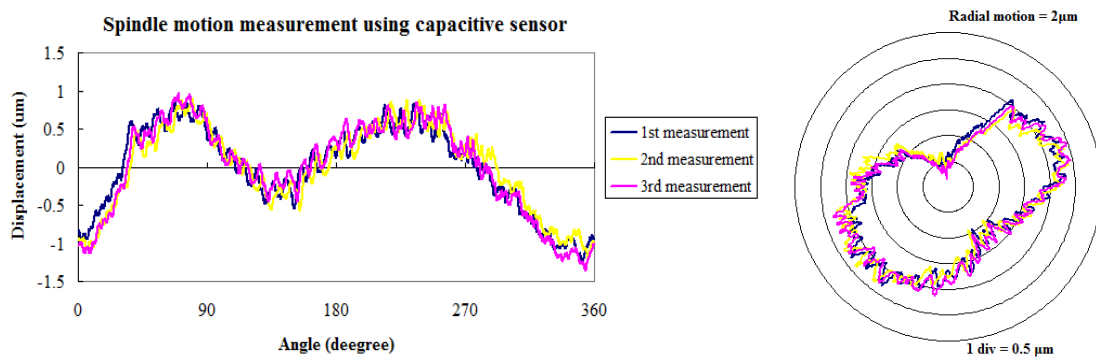
(a) Displacement of spindle radial motion (b) Polar plot of spindle radial motion

Fig. 4.21 Measurement results of the spindle radial motion using a capacitive sensor

(a) Interference signal   (b) Lissajous diagram
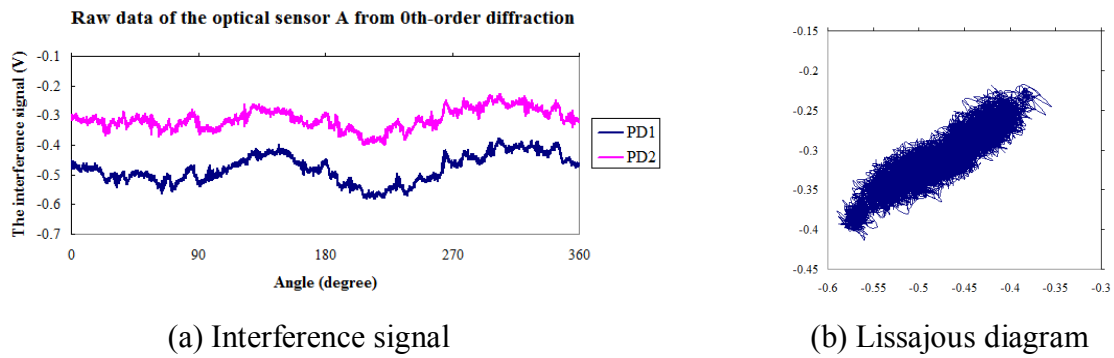
Fig. 4.22 Axial (Z-axis) motion from optical sensor A

(a) interference signal   (b) Lissajous diagram
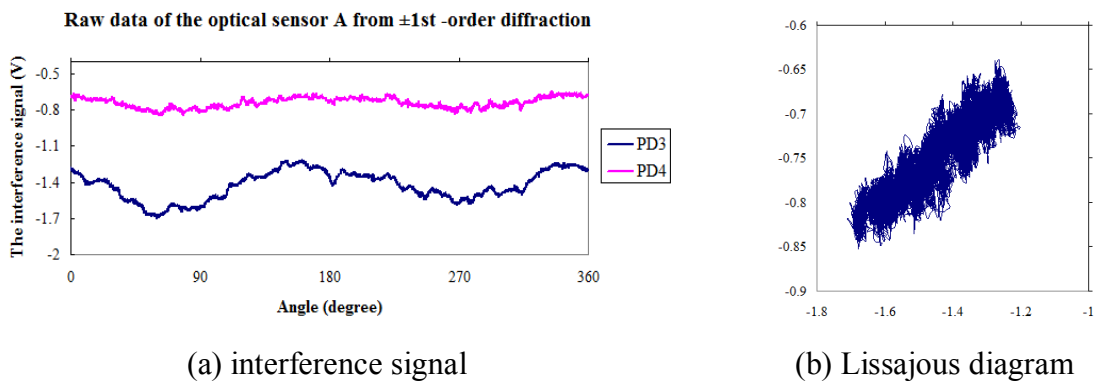
Fig. 4.23 Radial (X-axis) motion from optical sensor A

(a) Interference signal   (b) Lissajous diagram
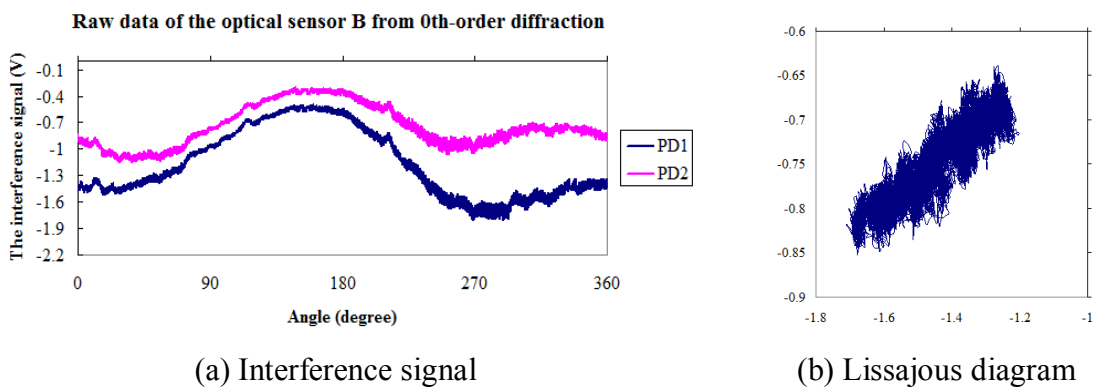
Fig. 4.24 Axial (Z-axis) motion from optical sensor B

Raw data of the optical sensor B from ±1st-order diffraction

(a) Interference signal   (b) Lissajous diagram
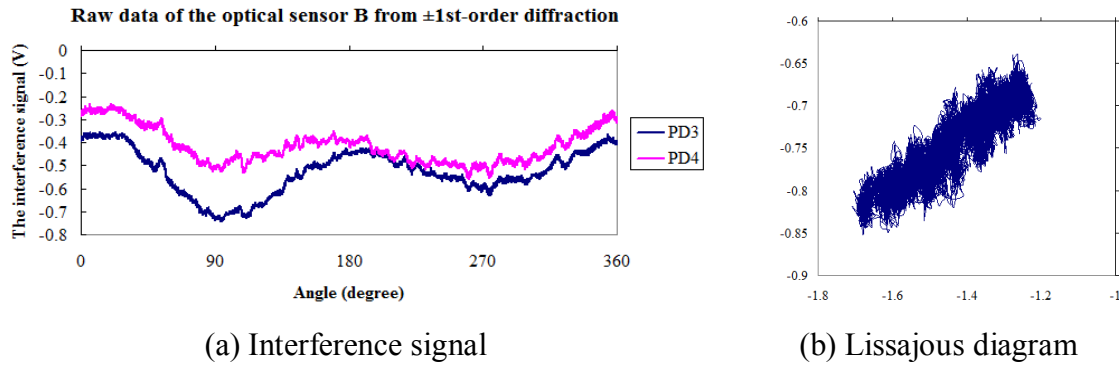
Fig. 4.25 Radial (X-axis) motion from optical sensor B

Raw data of the optical sensor C from 0th-order diffraction

(a) Interference signal   (b) Lissajous diagram
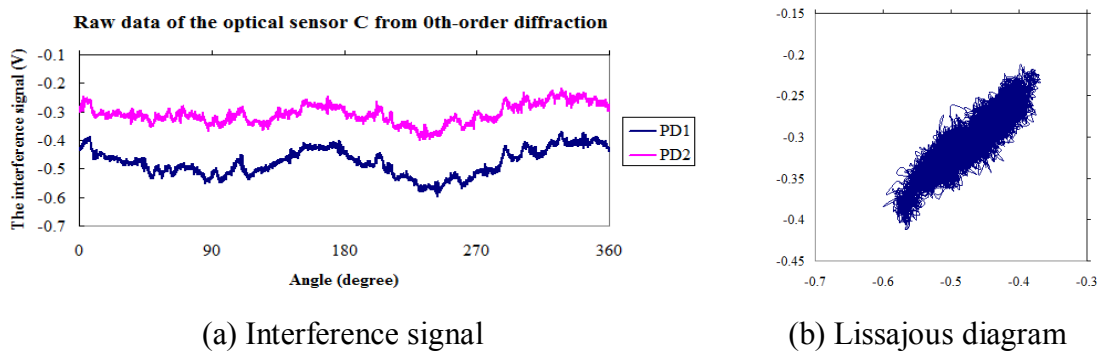
Fig. 4.26 Axial (Z-axis) motion from optical sensor C

Raw data of the optical sensor C from ±1st -order diffraction

(a) Interference signal   (b) Lissajous diagram
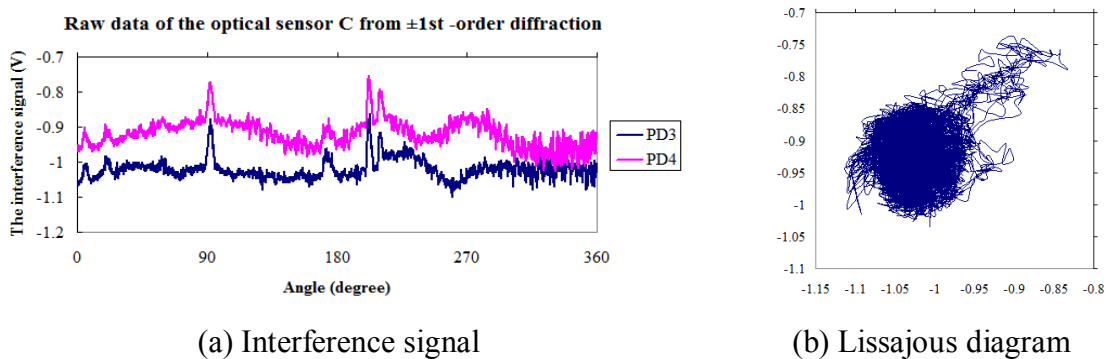
Fig. 4.27 Radial (X-axis) motion from optical sensor C

Figures 4.22 to 4.27 show the measurement signals of the axial (Z-axis) and radial (X-axis) motions from three optical sensors (A, B, and C), respectively. The collated signals contain some frequency components (such as vibration, DC offset, centering, tiling ect.) which do not correspond to the radial, angular, and axial motion errors of the spindle. The instrument cannot align the centering and tilting to reach the measurement target (centering error less than 1 μm, tiling error less than 10 arcsec), which directly affects the stability of

the optical sensor. Due to these problems in the measurement of spindle motion, we could not obtain the quadrature phase shift of two interference signals with the phase difference of 90° (at PD1 0°, PD2 90°, PD3 0°, and PD4 90°). All measurement data for five degrees of freedom motion of the spindle is inaccurate. Hence, an improvement of the alignment techniques for centering and tilting is required. Using some measuring instruments, such as a capacitive sensor and an autocollimator, the centering and the tilting errors can be measured, and the measurement results can be compared with those of the optical sensor.

(a) Interference signal   (b) Lissajous diagram
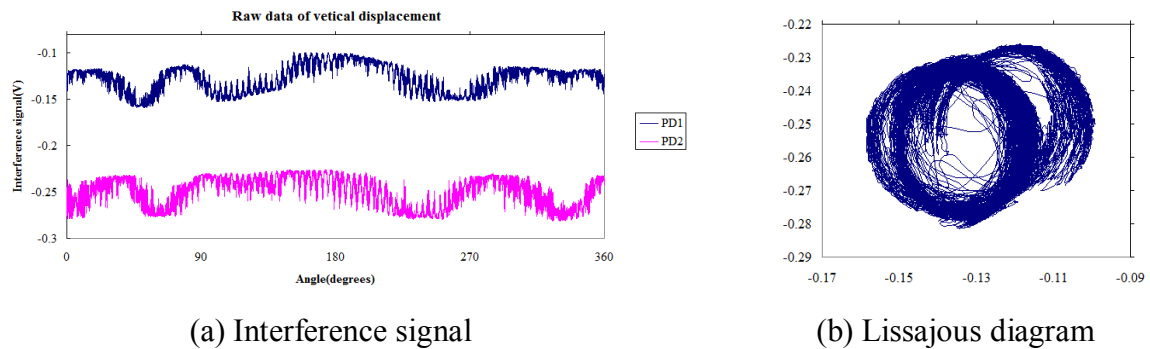
Fig. 4.28 Axial (Z-axis) motion from an optical sensor after improving the alignment techniques

Since we have improved the alignment techniques to reduce the centering and tilting errors until they are lower than the measurement target (centering error less than 1 μm, tilting error less than 10 arcsec), the optical sensor can observe the displacement signal as shown in Fig. 4.28. However, the concurrent measurement of spindle motion using the quadrature detection technique has some disadvantages, such as the use of many optical elements and photodetectors in one optical sensor, difficult to align and adjust all optical elements in the optical sensor, and difficulty in adjusting the sensitivity of the photodetector. Therefore, a novel technique for the concurrent measurement of spindle motion using a phase modulation technique is proposed and developed to solve the previous problems.

Chapter 5

Spindle motion measurement using phase modulation technique

This chapter describes the instrumentations and measurement results of spindle motion when we apply the phase modulation technique to the measurement system. The performance of the Michelson and grating interferometers and the high-rigidity compact optical sensor is evaluated. The measurement of five degrees of freedom spindle motion and the error separation method are performed. The effect of the interpolation error on the displacement is also discussed in this chapter.

5.1 Instrumentations
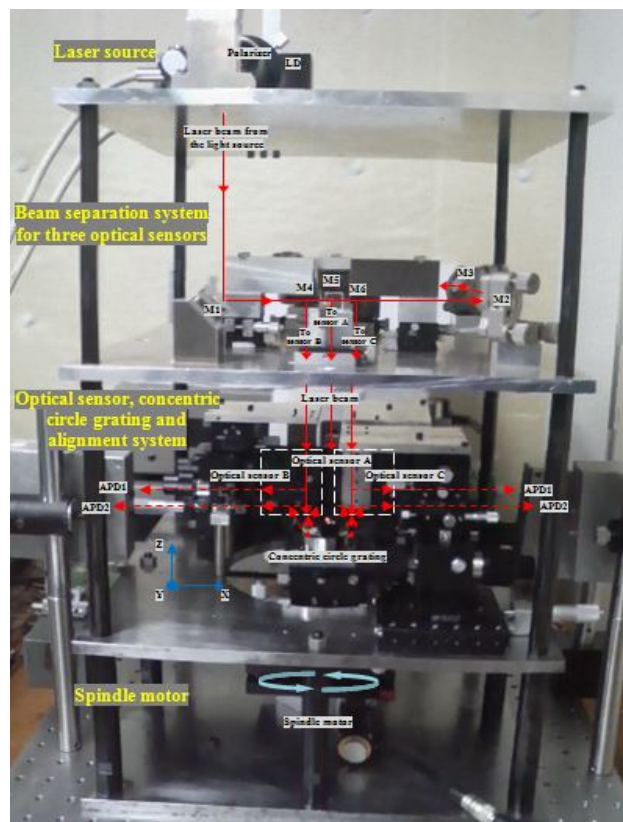
Fig. 5.1 Concurrent measurement system for spindle motion

The concurrent measurement system for spindle motions using three optical sensors and a concentric circle grating with the phase modulation technique is developed from the previous measurement system (the prototype instrument). Figure 5.1 shows the experimental setup. The measurement system consists of seven main parts:

1) Laser source

2) Beam separation system for three optical sensors

3) Optical sensor, concentric circle grating, and alignment system

4) Spindle motor

5) Avalanche photodetector

6) Lock-in amplifier

7) Recording data system

1) Laser source

In the measurement system, a laser diode (Opnext, model: HL6344) is used as the light source. Figure 5.2 shows a photograph of the laser diode. It is fixed on a laser diode mount. This laser diode can be modulated to a frequency of up to 250 kHz. Tables 5.1, 5.2 and 5.3 show the specifications of the laser diode and its current and temperature controllers, respectively.
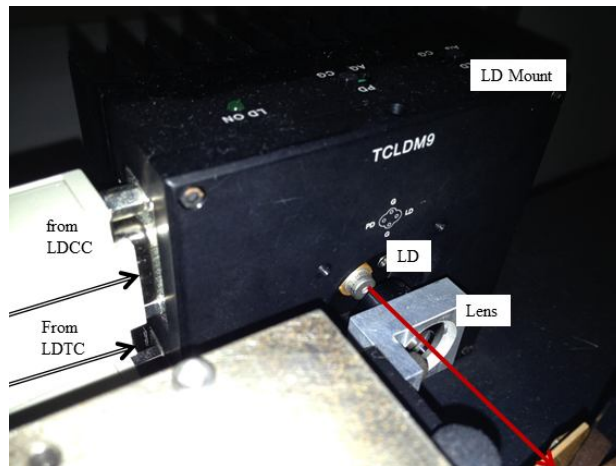
Fig. 5.2 Photograph of the laser diode (Opnext, model: HL6344)

Table 5.1 Specifications of laser diode (Opnext, model: HL6344)

Wavelength	635	[nm]
Input voltage (DC)	2.4	[V]
Input current	45	[mA]
Output power	10	[mW]
Beam divergence	17×20	[degree]
Operating temperature	-10 to +50	[°C]
Storage temperature	-40 to +85	[°C]

Table 5.2 Specifications of current controller (THORLABS, model: LDC202C)

Current control range	0 - ±200	[mA]
Resolution	10	[μA]
Accuracy	±100	[μA]
Modulation input bandwidth	DC ~ 250	[kHz]

Table 5.3 Specifications of temperature controller (THORLABS, model: TED200C)

Temperature control range	-45 ~ 150	[°C]
Resolution	0.01	[°C]
Accuracy	±0.1	[°C]

2) Beam separation system for three optical sensors
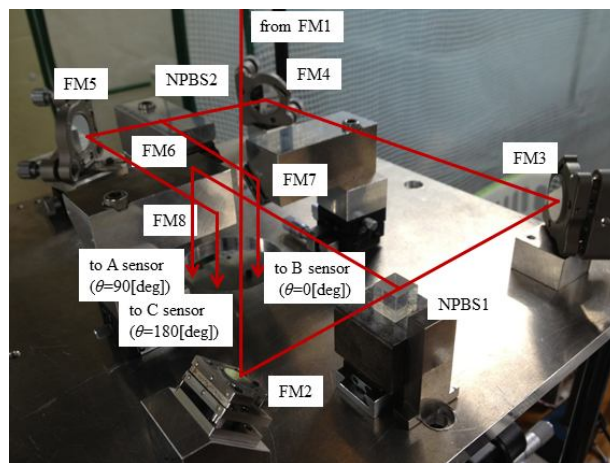
Fig. 5.3 Beam separation system

The beam separation system includes the beam splitters (BS) and fixed mirrors (FM). The laser beam from the light source is separated into three beams after passing through this system, then propagate towards the three optical sensors. Figure 5.3 shows the beam separation system.

3) **Alignment system, optical sensor, and concentric circle grating system**

In this system, the three optical sensors and the concentric circle grating are set up using precise alignment stages and the spindle motor as shown in Figs. 5.4 and 5.5, respectively.
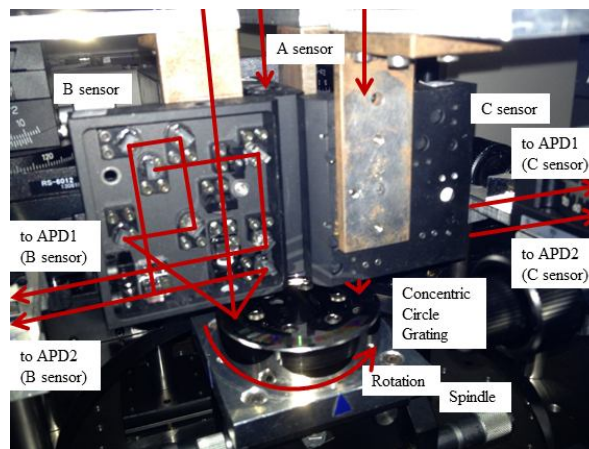
Fig. 5.4 Setup and alignment of the three optical sensors and the concentric circle grating
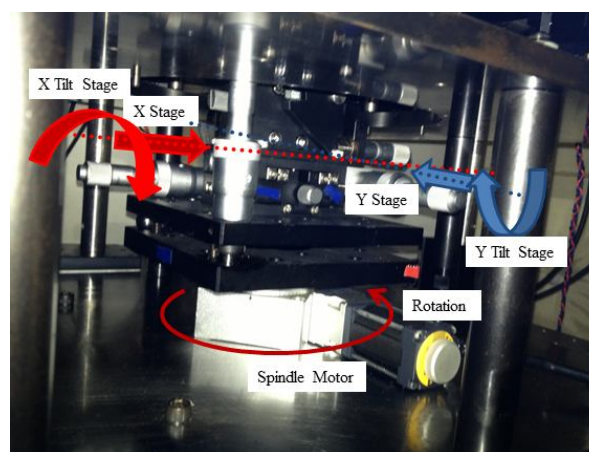
Fig. 5.5 Setup and alignment of the concentric circle grating and the spindle motor using precise alignment stages

The prototype optical sensor could not obtain the displacement signal from the spindle motion as mentioned in chapter 4 (see Sect. 4.5). The low rigidity of the optical sensor is a problem. In this study, a high-rigidity compact optical sensor is fabricated as shown in Fig. 5.6. The measurement system diagram of the high-rigidity compact optical sensor which is used for the spindle measurement system is shown in Fig. 5.6 (a). Figure 5.6 (b) shows a photograph of the high-rigidity compact optical sensor (size: W: 60 [mm] × L: 65 [mm] × H: 15 [mm]), which is fabricated and assembled by Chuo Precision Industrial Co., Ltd. [120]. We designed the optical path difference of the 0th-order interferometer (a Michelson interferometer) arms and the optical path difference of the ±2nd-order interferometer arms (a grating interferometer) with $L_{int} = 50$ mm and $L_{\pm 2} = 100$ mm, respectively.
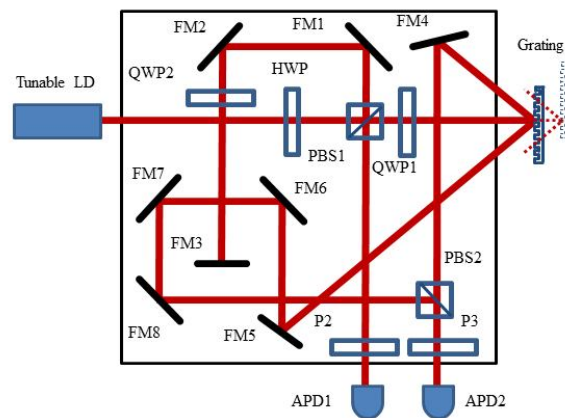
(a) Optics design of the high-rigidity compact optical sensor
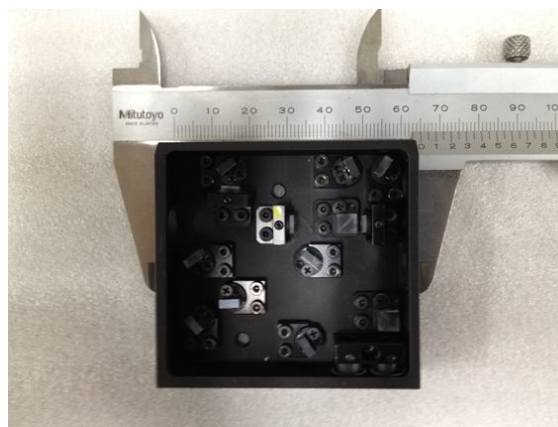
(b) Photograph of the high-rigidity compact optical sensor

(c) Three optical sensors for spindle motion measurement

Fig. 5.6 High-rigidity compact optical sensor
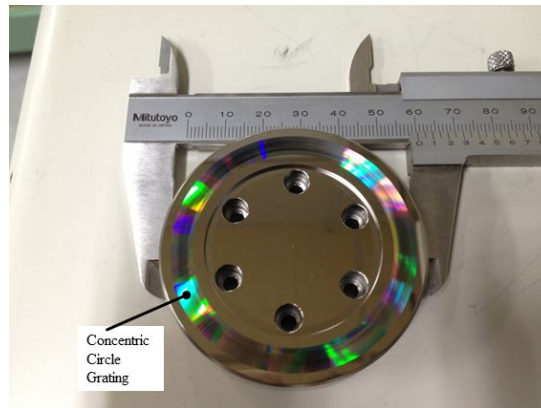
(a) Photograph of the new concentric circle grating (2 μm pitch)
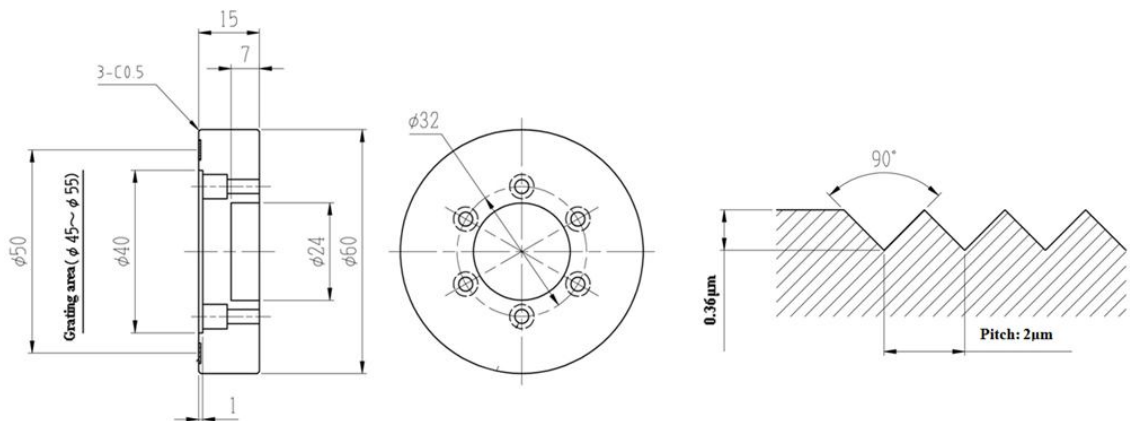
(b) New concentric circle grating design

Fig. 5.7 New concentric circle grating

In this measurement technique, a new concentric circle grating is fabricated to simplify the setting up of the three compact optical sensors. Figures 5.7 (a) and (b) shows a photograph and the design of the new concentric circle grating, respectively. The fabrication process of the concentric circle grating had been explained in chapter 2 (see Sect. 2.3).

4) Spindle motor

The spindle motor (CHUO SEIKI, model: ARS-636-HM) is used as the device under test to determine the rotation error of the spindle in this experiment. It is set up with the alignment stage for the concentric circle grating. To evaluate the performance of the optical sensor, the spindle motor is rotated at low speed. In the experimental system, the spindle motor is rotated at a speed of 4 rpm. A photograph of the spindle motor and its specifications are shown in Fig. 4.4 and Table 4.3, respectively (see chapter 4).

5) Avalanche photo detector

The avalanche photodetector, APD, (Photonics, model: C5460) is used to detect the intensity of the interference signal from the axial motion (APD1) and the radial motion (APD2) of the spindle. It is assembled in a die-cast aluminum box to shield it from the electric noise effects of the interference signal. Figure 5.8 and Table 5.4 show a photograph and the specifications of the APD, respectively.

Fig. 5.8 Photograph of avalanche photodetector (Photonics, model: C5460)

Table 5.4 Specifications of avalanche photodetector (Photonics, model: C5460)

Active area	1.5	[mm]
Photosensitivity	1.5×10^6	[V/W]
Frequency bandwidth	DC～10	[MHz]
Wavelength quantum efficiency	11	[V/W]
Spectral response range	400 to 1000	[nm]
Power supply	±12	[V]

6) Lock-in amplifier

The lock-in amplifier is used to multiply each reference signals through the low-pass filter, to achieve synchronous detection. Figure 5.9 shows an operation diagram of the lock-in amplifier. In Fig. 5.9, the interference signals of the axial (Z-axis) and radial (X-axis) motion from APD1 and APD2 pass through the lock-in detection system. They are synchronized with the reference signal of the 3rd-harmonic sine wave ($3\omega_m$) and the reference signal of the 2nd-harmonic cosine wave ($2\omega_m$), respectively. In this case, the Lissajous diagram can be obtained from two reference signals with a phase difference of 90° [109]. One optical sensor requires four lock-in amplifiers to acquire the signals necessary for generating the Lissajous diagram.
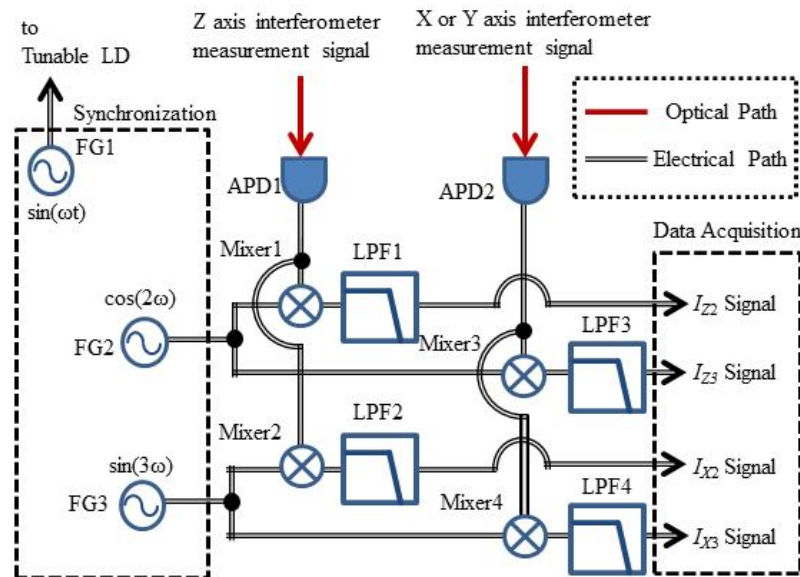
Fig. 5.9 Operation diagram of the lock-in amplifier

In this thesis, two types of lock-in amplifiers are used in the measurement system.

a) Digital lock-in amplifier

b) Analog lock-in amplifier

a) Digital lock-in amplifier

The digital lock-in amplifier (Stanford Research Systems, model: SR830) is used in the experiment. There are many advantages of the digital lock-in amplifier such as ease of changing the setting of the low-pass filter, time constant, lock-in detection, and the roll-off characteristic when it is applied to the spindle measurement system. Figure 5.10 and Table 5.5 show a photograph and the specifications of the digital lock-in amplifier, respectively. However, it has a high cost of application when use with three optical sensors (one optical sensor uses four lock-in amplifiers). Therefore, the digital lock-in amplifier is used only for checking the performance of the three optical sensors before performing the concurrent measurement of spindle motion. In addition, for the measurement of spindle rotation, the roll-off characteristic is selected to be -24 [dB/oct] and the cut-off frequency is 300 [Hz]. Since the frequency bandwidth is approximately 100 [kHz] below that of the digital lock-in amplifier, when using the modulation frequency of a sinusoidal phase modulation method, it is necessary to set the frequency bandwidth 33 [kHz] below the triple wave (reference wave signal is limited).

Fig. 5.10 Photograph of digital lock-in amplifier

(Stanford Research Systems, model: SR830)

Table 5.5 Specifications of digital lock-in amplifier (Stanford Research Systems, model: SR830)

Frequency range	1[mHz]～102[kHz]
Roll-off characteristics	-6,-12,-18,-24[dB/oct]
Cut-off frequency	0.333[Hz]～100 [kHz]
Time constants	10[μs]～30 [ks]

b) Analog lock-in amplifier

The analog lock-in amplifier manufactured by Chuo Precision Industrial Co., Ltd. is also applied in the experiment. The advantage of the analog lock-in amplifier is its low cost as compared with the digital lock-in amplifier. Figure 5.11 shows a circuit diagram of two lock-in amplifiers for 2nd- and 3rd-harmonic lock-in detections. The circuit used four-quadrant multipliers (AD835, Analog Devices), precision operational amplifiers and a passive low pass filter. Table 5.6 shows the specifications of the analog lock-in amplifier. Figure 5.11 shows that the analog lock-in amplifier consists of a multiplier IC and an RC circuit (resistors and capacitors). In this case, the roll-off characteristic and the cut-off frequency are fixed at -18 [dB/oct] and 5 [kHz], respectively. Hence, it is feasible to use the sinusoidal phase modulation method to detect the lock-in signal.
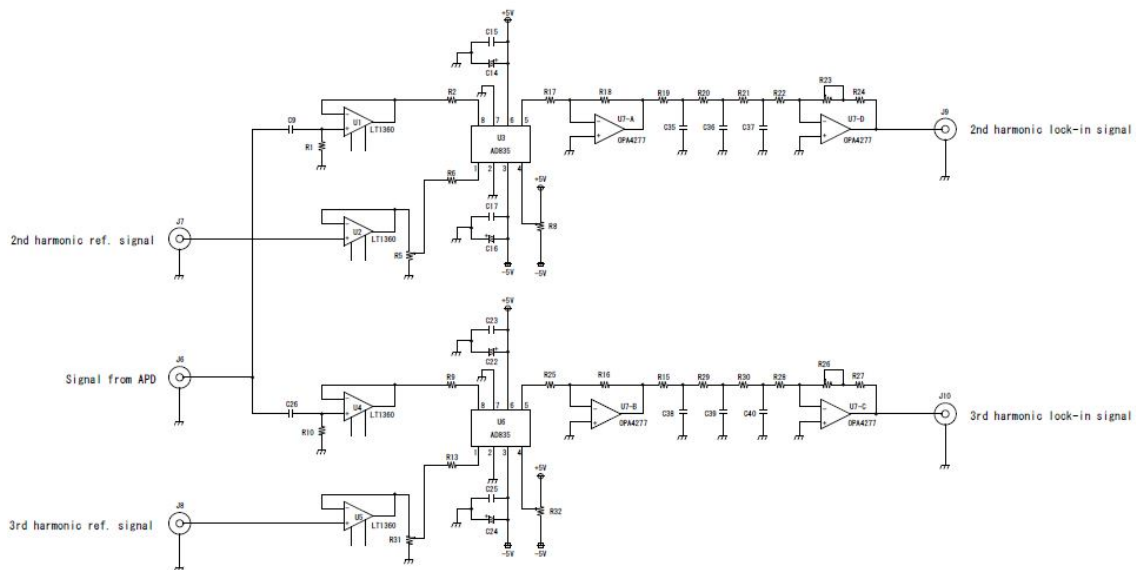
Fig. 5.11 Circuit diagram of analog lock-in amplifier

Table 5.6 Specifications of analog lock-in amplifier

Roll-off characteristics	-18　[dB/oct]
Frequency range	5　[kHz]
Power supply	±5　[V]

7) Recording data

The data acquisition system has the unique functionality to serve the application-specific requirement. The entire system shares common components that include sensors, data acquisition hardware, and a computer. In this thesis, the data acquisition system is used for conversion of the analog signal from the photodetectors to the digital signal (A/D converter) using the Lab VIEW data acquisition program. Table 5.7 shows the specifications of the A/D converter (National Instruments, model: NI PCI-622, M series). The measurement of five degrees of freedom spindle motion requires 12 input ports in the connector block for transferring data to the PC. All data is acquired by the input of a signal ±5 V. The measured voltage resolution can be calculated by

$$\text{Measurement voltage resolution} = \frac{\text{Measurement range}}{\text{Resolution}} = \frac{10[\text{V}]}{2^{16}} = 153[\mu\text{V}] \qquad (5.1)$$

Table 5.7 Specifications of A/D converter (National Instruments, model: NI PCI-622, M series)

Resolution	16　[bit]
Number of acquired samples	250　[kS/s]
Number of input channel (to PC)	16　[channels]

5.2 Evaluation of the performance of two-axes displacement-measuring interferometers using phase modulation technique

To confirm the validity of Eqs. (3.27), (3.28), (3.33), and (3.34) in chapter 3, we fabricated the grating interferometers as shown in Fig. 5.12. In the experiment, the concentric circle grating with the pitch of 2 μm is set up on the XZ-PZT stage. Tables 4.4 and 4.5 (see chapter 4) show the specifications of the Z-axis PZT stage and the X-axis PZT

stage, respectively. A laser diode (LD) with a wavelength of 635 nm and a sinusoidal phase modulation frequency of 20 kHz is applied to the interferometer as a light source. APD1 detects the interference signal of axial (Z-axis) motion, and APD2 detects the interference signal of radial (X-axis) motion. The measurement conditions applied to the XZ-PZT stage motion are shown in Table. 5.8. We apply triangular motion with an amplitude of 1 μm and frequency of 1 Hz to the XZ-PZT stage. The measurement time is 6 second, and the cut off frequency of the low pass filter of the lock-in amplifier is 300 Hz, respectively.

By using Eqs. (3.22) and (3.30) in chapter 3, the modulation frequency bandwidth Δf of each interferometer can be calculated by the following:

$$\text{For the Michelson interferometer,} \quad \Delta f = \frac{ck_{m,0}}{4\pi n L_{\text{int}}}, \tag{5.2}$$

$$\text{For the grating interferometer,} \quad \Delta f = \frac{ck_{m,\pm 2}}{2\pi n L_{\pm 2}}. \tag{5.3}$$

If we apply $n = 1$, $c = 3.0 \times 10^8$ m/s, $k_{m,0} = k_{m,\pm 2} = 1$, $L_{\text{int}} = 50$ mm, and $L_{\pm 2} = 100$ mm, then the modulation frequency bandwidth Δf of the Michelson interferometer can be calculated as

$$\Delta f = \frac{3 \times 10^8 \times 1}{4\pi \times 1 \times 50 \times 10^{-3}} = 0.48 \ [\text{GHz}] \tag{5.4}$$

and the modulation frequency bandwidth Δf of the grating interferometer can be calculated as

$$\Delta f = \frac{3 \times 10^8 \times 1}{2\pi \times 1 \times 100 \times 10^{-3}} = 0.48 \ [\text{GHz}]. \tag{5.5}$$
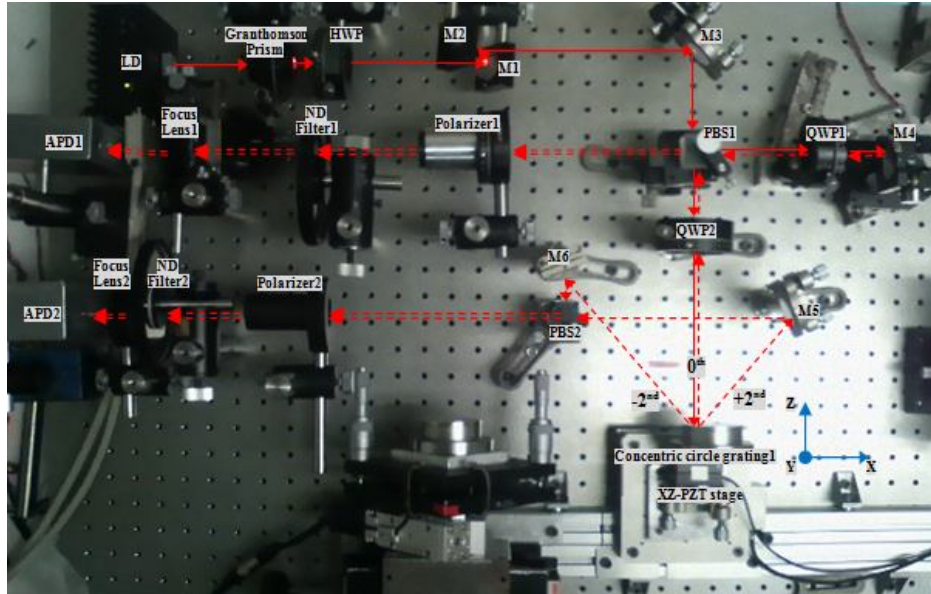
Fig. 5.12 Experimental setup for evaluation of the two-axes displacement measuring interferometers using phase modulation technique

Table 5.8 Measurement conditions applied to the XZ-PZT stage motion

Laser diode wavelength	635	[nm]
Grating pitch	2	[μm]
Modulation frequency for LD	20	[kHz]
Modulation depth ($k_{m,0}$ and $k_{m,\pm2}$)	1	[rad]
Modulation frequency bandwidth of Z- and X-axis interferometers	0.48	[GHz]
Amplitude applied to XZ-PZT stage	1	[μm]
Frequency applied to XZ-PZT stage	1	[Hz]
Motion shape	Triangular	
Sampling time	6	[s]
Sampling rate	1	[kHz]
Cut-off frequency of low-pass filter	300	[Hz]

Figure 5.13 shows Lissajous diagrams of the axial (Z-axis) and radial (X-axis) motion of the XZ-PZT stage measurement. In this figure, the Lissajous diagrams are deformed due to the variation of the laser beam intensity, and the center of each Lissajous diagram is not

at the origin. In this case, the normalized Lissajous diagrams can be calculated using the following eqations,

$$I'_z(3\omega_m) = \frac{I_{0F}(3\omega_m)J_2(k_m)}{\sqrt{(I_{0F}(2\omega_m)J_3(k_m))^2 + (I_{0F}(3\omega_m)J_2(k_m))^2}} = \sin\left(\varphi'_0 + \frac{4\pi}{c}nf_0\Delta z\right) \quad (5.6)$$

$$I'_z(2\omega_m) = \frac{I_{0F}(2\omega_m)J_3(k_m)}{\sqrt{(I_{0F}(2\omega_m)J_3(k_m))^2 + (I_{0F}(3\omega_m)J_2(k_m))^2}} = \cos\left(\varphi'_0 + \frac{4\pi}{c}nf_0\Delta z\right) \quad (5.7)$$

$$I'_x(3\omega_m) = \frac{I_{\pm2}(3\omega_m)J_2(k_m)}{\sqrt{(I_{\pm2}(2\omega_m)J_3(k_m))^2 + (I_{\pm2}(3\omega_m)J_2(k_m))^2}} = \sin\left(\varphi'_{\pm2} + \frac{8\pi}{d}\Delta x\right) \quad (5.8)$$

$$I'_x(2\omega_m) = \frac{I_{\pm2}(2\omega_m)J_3(k_m)}{\sqrt{(I_{\pm2}(2\omega_m)J_3(k_m))^2 + (I_{\pm2}(3\omega_m)J_2(k_m))^2}} = \cos\left(\varphi'_{\pm2} + \frac{8\pi}{d}\Delta x\right) \quad (5.9)$$
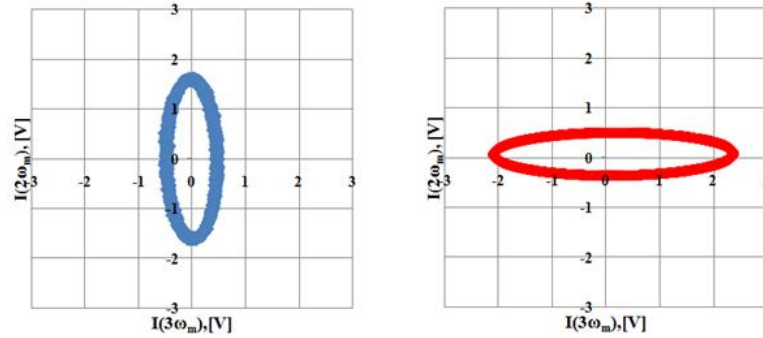
(a) Axial (Z-axis) motion   (b) Radial (X-axis) motion

Fig. 5.13 Lissajous diagrams of the XZ-PZT stage motion

The normalized Lissajous diagrams are shown in Fig. 5.14. in which the center and radius are the origin and 1, respectively. The axial (Z-axis) and radial (X-axis) motion of the XZ-PZT stage are shown in Figs. 5.15 and 5.16, respectively. In these figures, the nonlinear errors (or cyclic errors) due to the polarization mixing of two interferometer arms can be seen. If there is no cyclic error, the measured motion must be triangular. However, the nonlinear error can be reduced by the polarization adjustment of two interferometer arms. Figure 5.17 shows the Lissajous diagrams of the axial (Z-axis) and radial (X-axis) motion of the XZ-PZT stage after the polarization adjustment. In Fig. 5.17, the center of each Lissajous diagram is closer to the origin as compared to that in Fig. 5.13. Figures 5.18 and 5.19 show the axial (Z-axis) and radial (X-axis) motion of the XZ-PZT stage,

respectively, after the polarization adjustment. It is seen from these figures that, the polarization adjustment can reduce the cyclic error of the two interferometers. In the near future, we will clarify the quantitative relationship between the cyclic error and the polarization mixing in the interferometers.
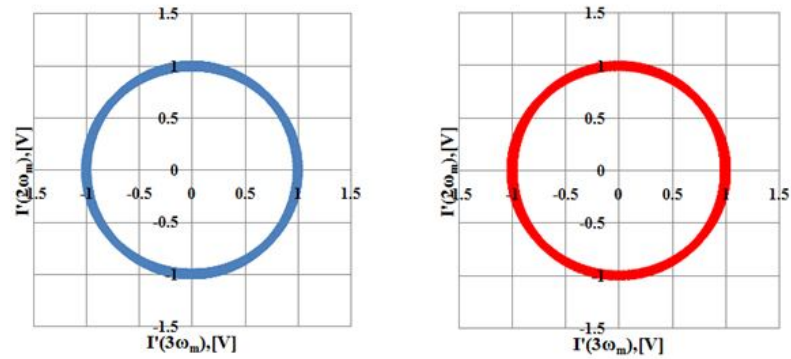
(a) Axial (Z-axis) motion   (b) Radial (X-axis) motion

Fig. 5.14 Normalized Lissajous diagrams of XZ-PZT stage motion
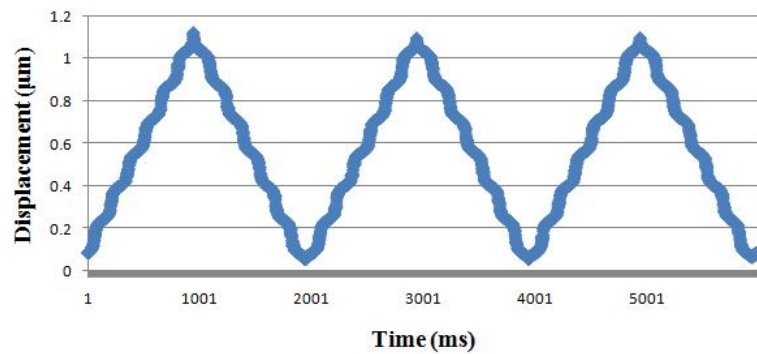
Fig. 5.15 Axial (Z-axis) motion of the XZ-PZT stage
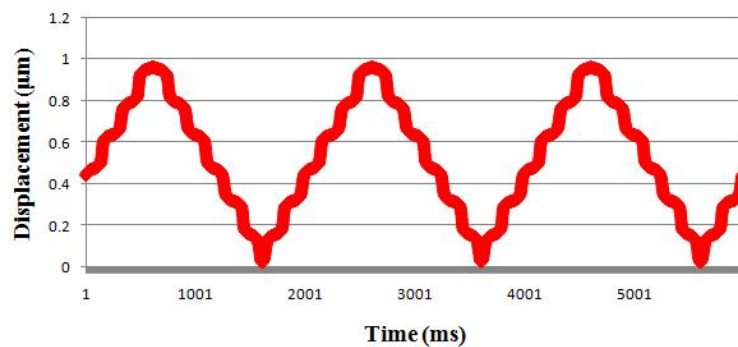
Fig. 5.16 Radial (X-axis) motion of the XZ-PZT stage

59

(a) Axial (Z-axis) motion   (b) Radial (X-axis) motion
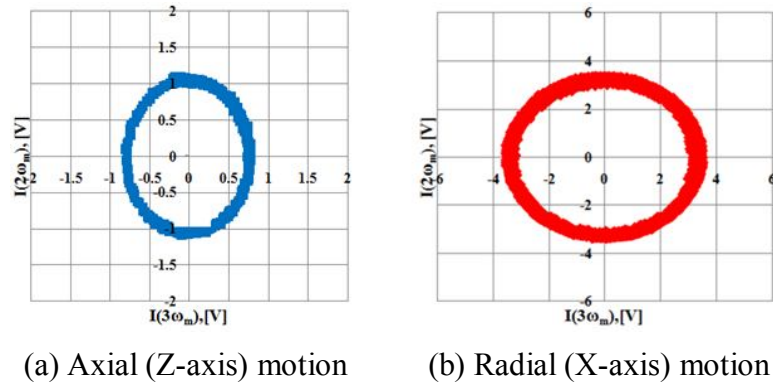
Fig. 5.17 Lissajous diagrams of the XZ-PZT stage motion after reduction of the nonlinear errors
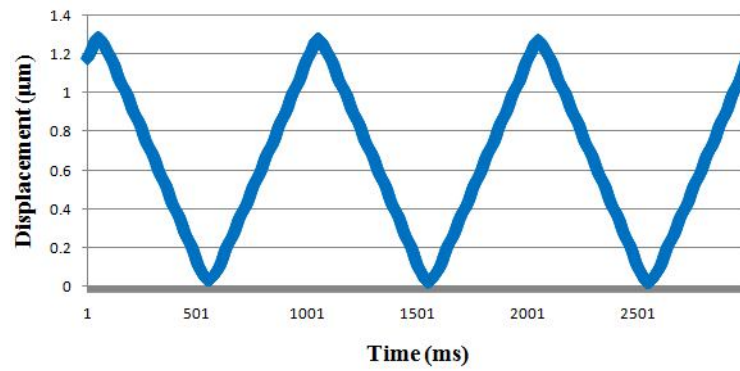
Fig. 5.18 Axial (Z-axis) motion of the XZ-PZT stage after reduction of the nonlinear errors
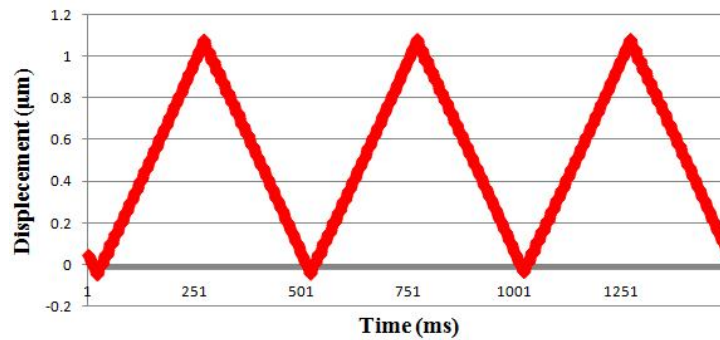
Fig. 5.19 Radial (X-axis) motion of the XZ-PZT stage after reduction of the nonlinear errors

5.3 Evaluation of the performance of the optical sensor using phase modulation technique

The experimental setup for evaluation of the performance of the high-rigidity compact optical sensor using the phase modulation technique is shown in Fig. 5.20. The concentric circle grating with a pitch of 2 μm was set on the XZ-PZT stage.
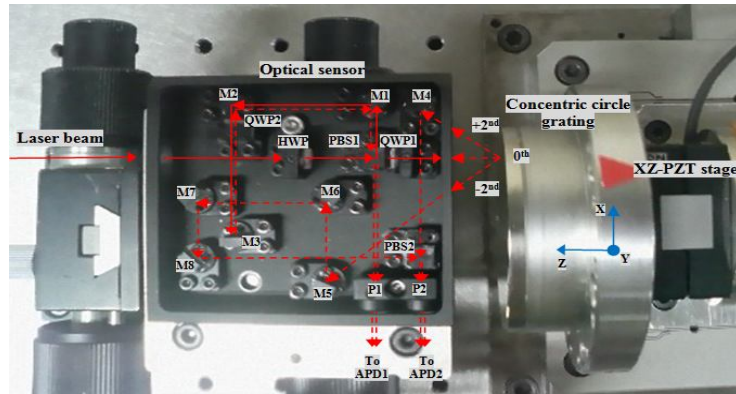
Fig. 5.20 Experimental setup for evaluation of the performance of the optical sensor using phase modulation technique

Table 5.9 Measurement conditions applied to the XZ-PZT stage motion

Laser diode wavelength	635	[nm]
Grating pitch	2	[μm]
Modulation frequency for LD	33	[kHz]
Modulation depth ($k_{m,0}$ and $k_{m,\pm2}$)	4.15	[rad]
Modulation frequency bandwidth of Z- and X-axis interferometers	1.98	[GHz]
Amplitude applied to X-PZT stage	1	[μm]
Amplitude applied to Z-PZT stage	0.8	[μm]
Frequency applied to XZ-PZT stage	1	[Hz]
Motion shape	Triangular	
Sampling time	3	[s]
Sampling rate	10	[kHz]
Cut-off frequency of low-pass filter	300	[Hz]

Tables 4.4 and 4.5 (see Sect. 4.2) show the specifications of the Z-axis PZT stage and the X-axis PZT stage, respectively. The optical sensor measures the axial (Z-axis) and radial (X-axis) motion of the XZ-PZT stage. Photodetector PD1 detects the interference signal of axial (Z-axis) motion from the 0th-order diffraction of grating. The photo detector PD2 detects the interference signal of radial (X-axis) motion from the ±2nd-order diffraction of the grating. The measurement conditions applied to the XZ-PZT stage are the

same as those shown in Table 5.9. We perform the experiment to evaluate the performance of the three optical sensors.
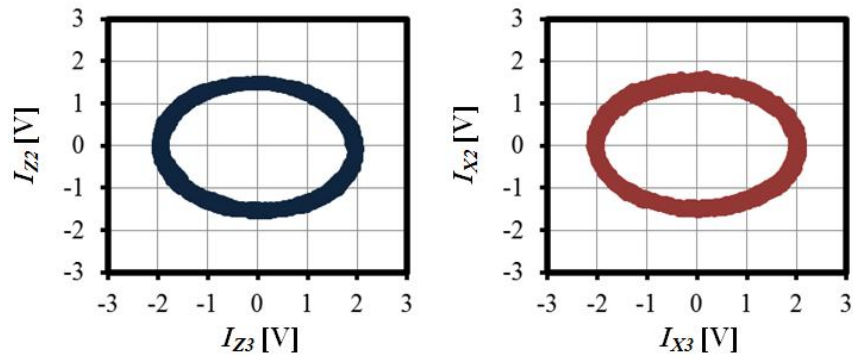
Axial (Z-axis) motion   Radial (X-axis) motion
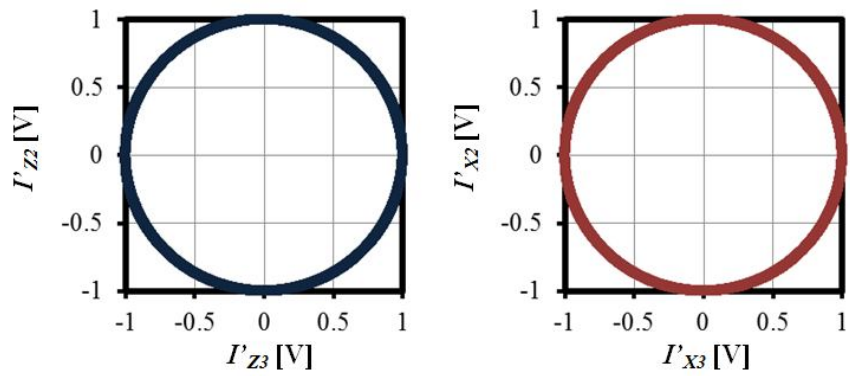
(a) Lissajous diagrams

Axial (Z-axis) motion   Radial (X-axis) motion

(b) Normalized Lissajous diagrams

Axial (Z-axis) motion

Radial (X-axis) motion

(c) Axial (Z-axis) and radial (X-axis) motions

Fig. 5.21 Measurement results of the XZ-PZT stage motion from optical sensor A
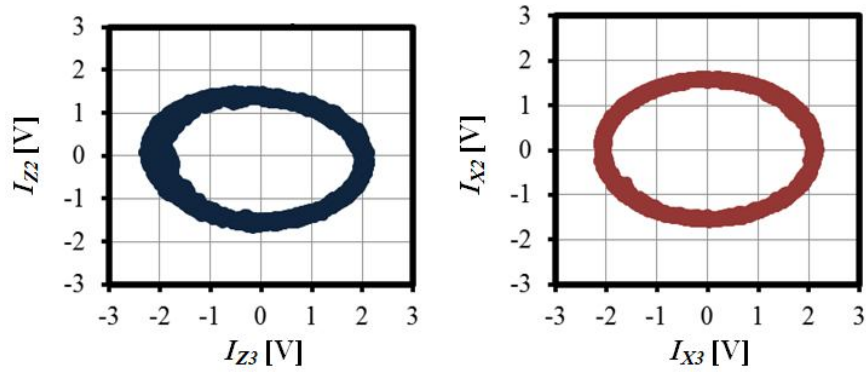
Axial (Z-axis) motion   Radial (X-axis) motion

(a) Lissajous diagrams
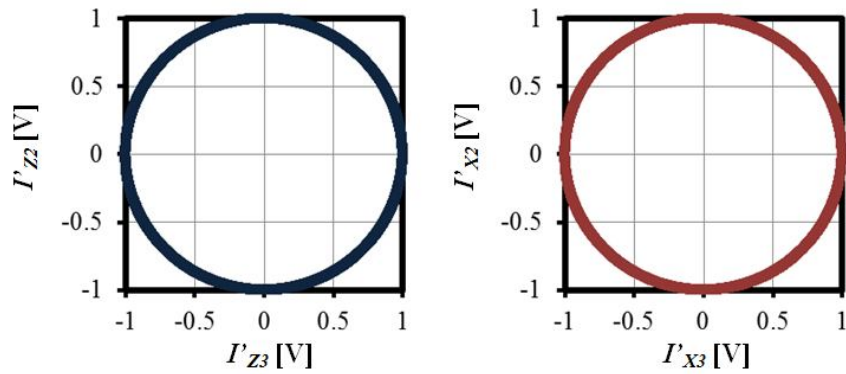
Axial (Z-axis) motion   Radial (X-axis) motion

(b) Normalized Lissajous diagrams
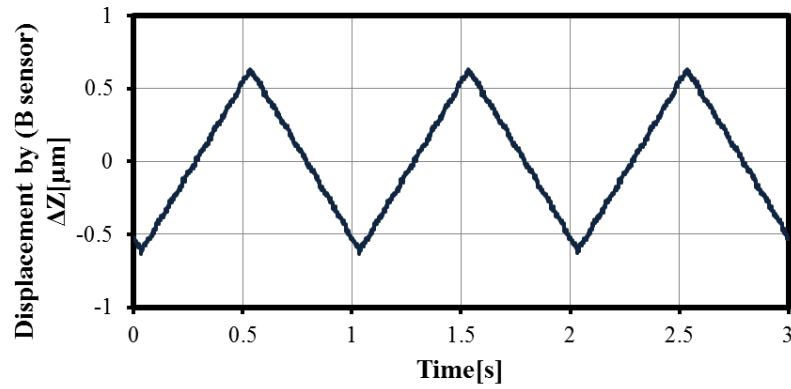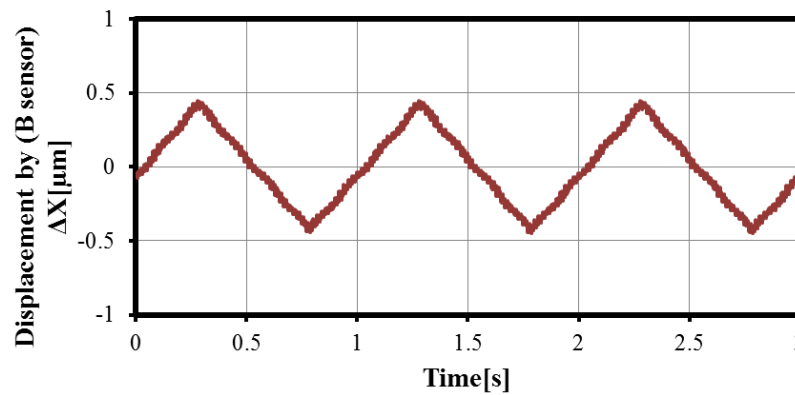
Axial (Z-axis) motion

Radial (X-axis) motion

(c) Axial (Z-axis) and radial (X-axis) motion

Fig. 5.22 Measurement results of the XZ-PZT stage motion from optical sensor B
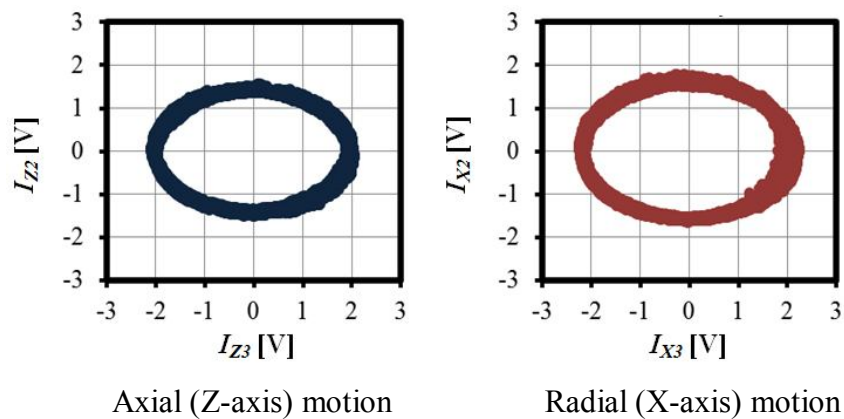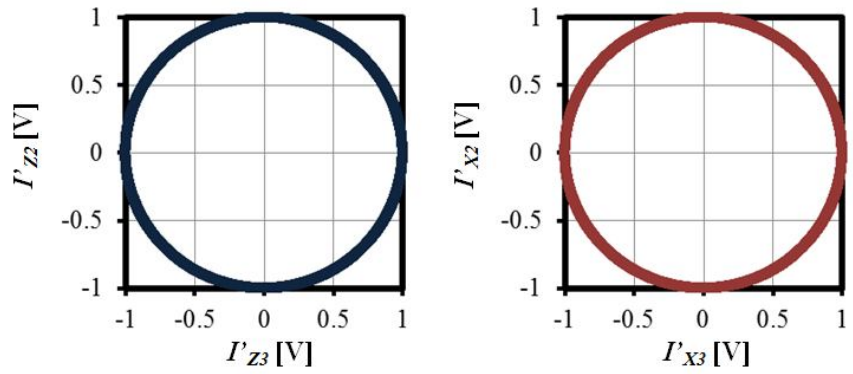
Axial (Z-axis) motion   Radial (X-axis) motion

(a) Lissajous diagrams

Axial (Z-axis) motion   Radial (X-axis) motion

(b) Normalized Lissajous diagrams
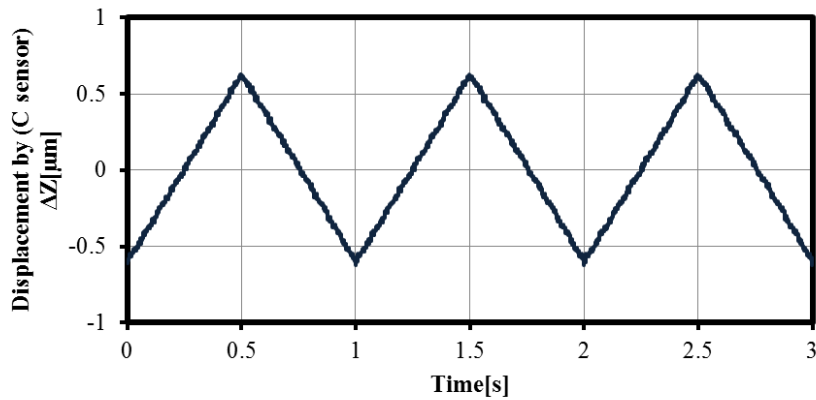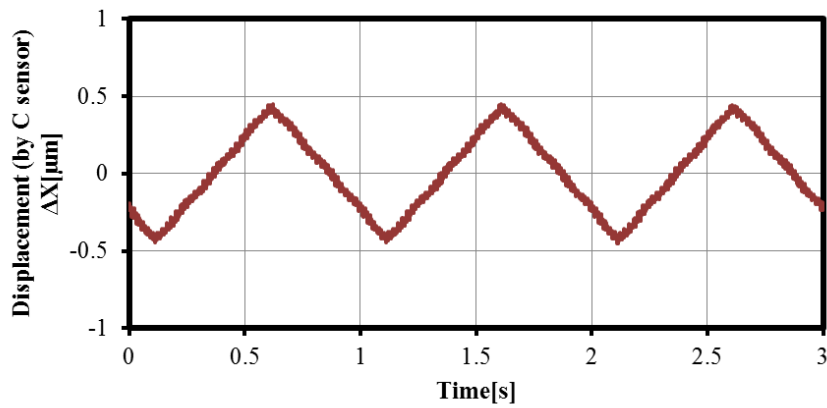
Axial (Z-axis) motion

Radial (X-axis) motion

(c) Axial (Z-axis) and radial (X-axis) motion

Fig. 5.23 Measurement results of the XZ-PZT stage motion from optical sensor C

65

Figures 5.21, 5.22, and 5.23 show the measurement results of the XZ-PZT stage motion from the optical sensors A, B, and C, respectively. In Figs. 5.21, 5.22, and 5.23 (a) shows the Lissajous diagrams of the axial (Z-axis) and radial (X-axis) motion, (b) shows the normalized Lissajous diagrams of the axial (Z-axis) and radial (X-axis) motion, and (c) shows the axial (Z-axis) and radial (X-axis) motion, form the measurement results of these three optical sensors, the axial (Z-axis) and radial (X-axis) motion of the XZ-PZT stage are approximately 1.2 μm and 0.8 μm, respectively.

5.4 Concurrent measurement of spindle motion using three optical sensors and phase modulation technique
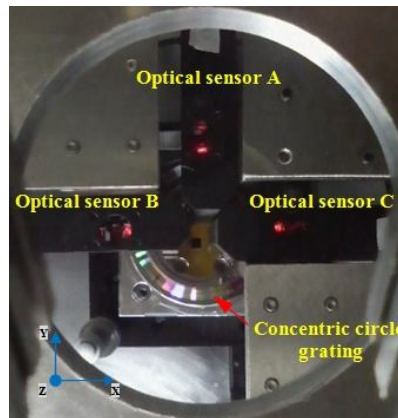
(a) Photograph of the experimental setup from the top view
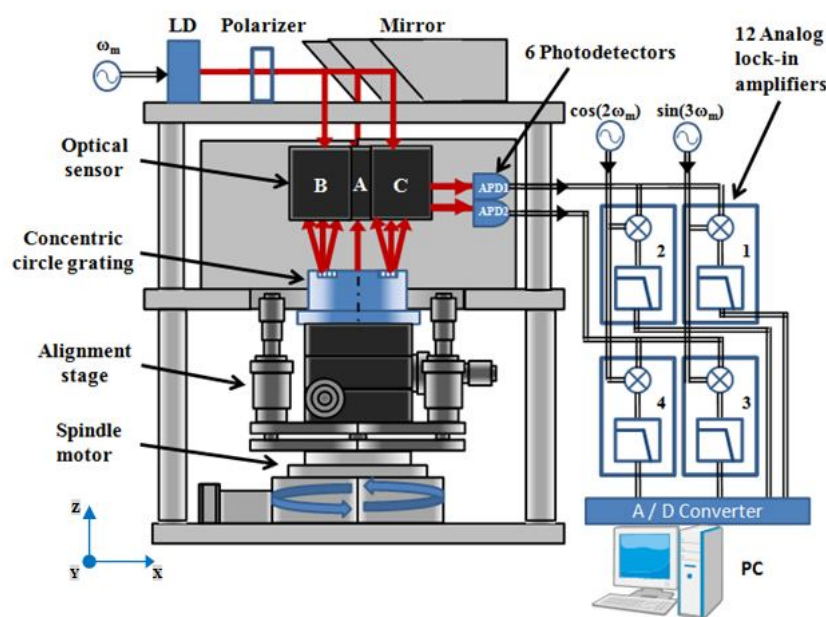
(b) Schematic diagram of setup for concurrent measurement of spindle motion
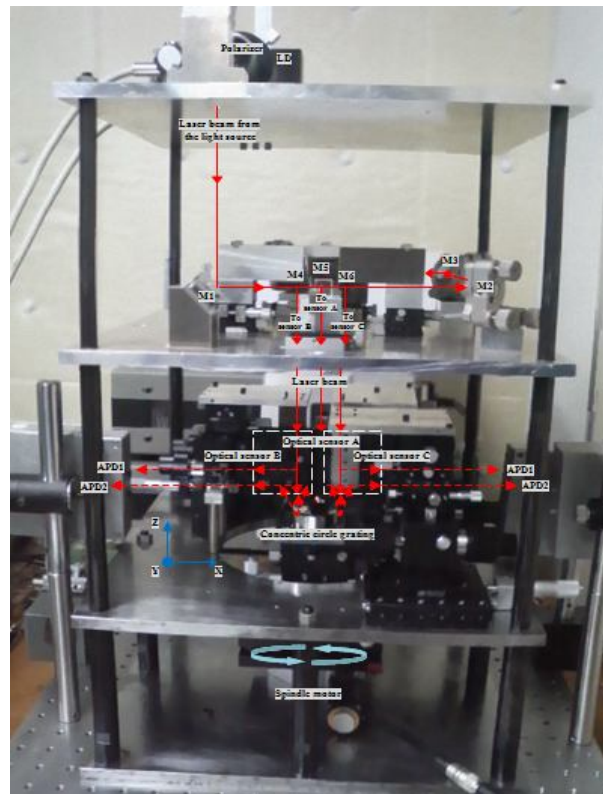
(c) Photograph of the experimental setup from the side view

Fig. 5.24 Experimental setup for the concurrent measurement of spindle motion using three optical sensors and phase modulation technique

Table 5.10 Measurement conditions applied to the spindle motion

Laser diode wavelength	635	[nm]
Grating pitch	2	[μm]
Modulation frequency for LD	33	[kHz]
Modulation depth ($k_{m,0}$ and $k_{m,\pm2}$)	3.76	[rad]
Modulation frequency bandwidth of Z- and X-axis interferometers	1.8	[GHz]
Revolution speed of spindle	4	[rpm]
Number of rotations	3	[rotations]
Sampling rate	10	[kHz]
Cut-off frequency of low-pass filter	300	[Hz]

The experimental setup for the concurrent measurement of spindle motion using three optical sensors and the phase modulation technique is shown in Fig. 5.24. In the experiment, the concentric circle grating with a pitch of 2 μm is set up on the spindle motor (Chuo Precision, model: ARS-636-HM [120]), and three optical sensors are set up above the concentric circle grating. Table 4.3 in chapter 4 shows the specifications of the spindle motor. In the experiment, photodetector APD1 observes the interference signal of axial (Z-axis) motion and photodetector APD2 observes the interference signal of radial (X- or Y-axis) motion. The measurement conditions applied to the spindle motion are shown in Table 5.10. The spindle is rotated at a low speed of 4 rpm. We measure the spindle motion for three rotations. The cut-off frequency of the low pass filter of the lock-in amplifier is 300 Hz. The measurement data is recorded by the PC through the data acquisition system (DAQ).
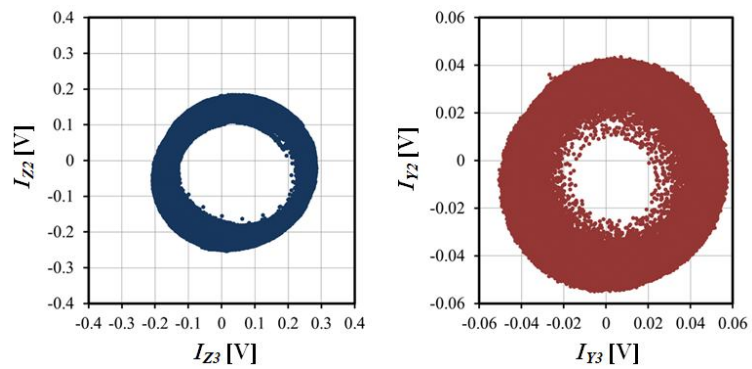
Axial (Z-axis) motion   Radial (Y-axis) motion

(a) Lissajous diagrams
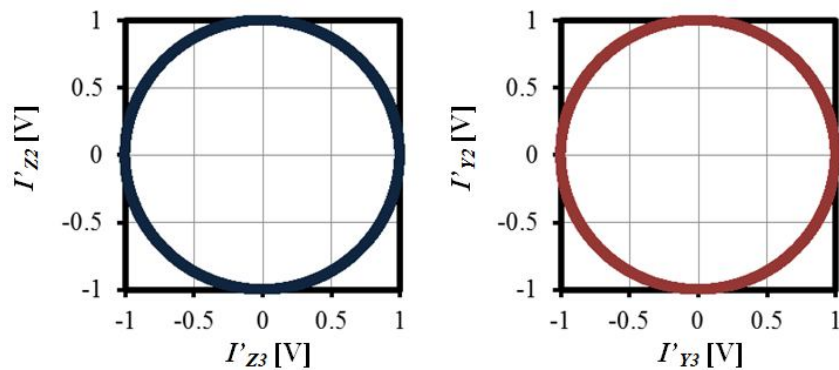
Axial (Z-axis) motion   Radial (Y-axis) motion

(b) Normalized Lissajous diagrams
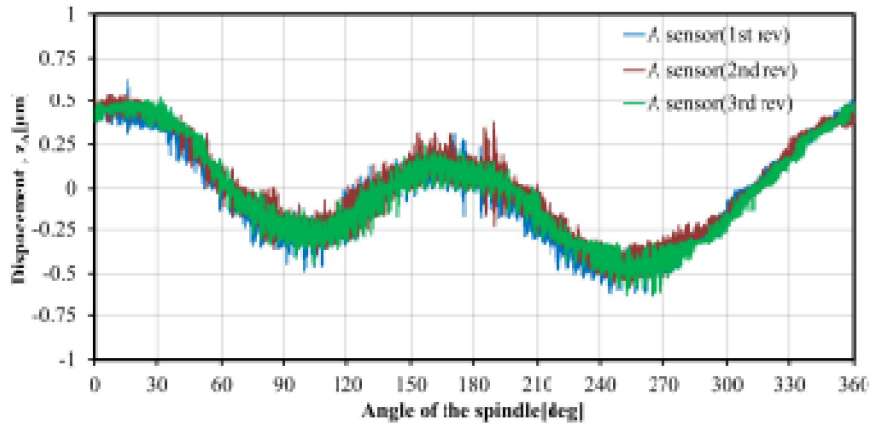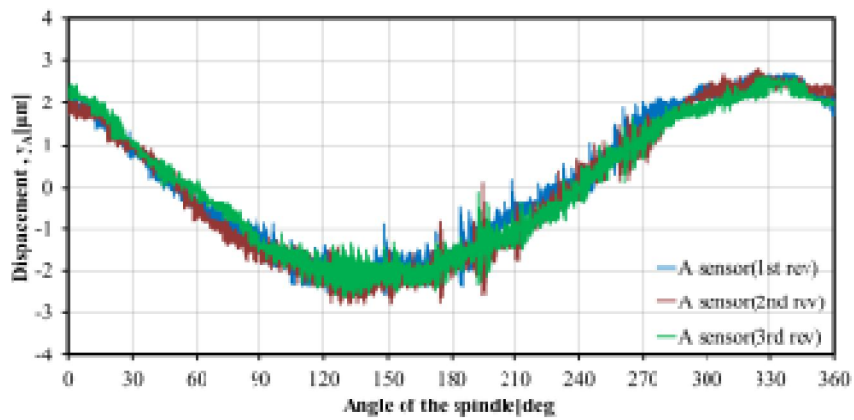
Axial (Z-axis) motion

Radial (Y-axis) motion

(c) Axial (Z-axis) and radial (Y-axis) motion

Fig. 5.25 Measurement results of the spindle motion from optical sensor A
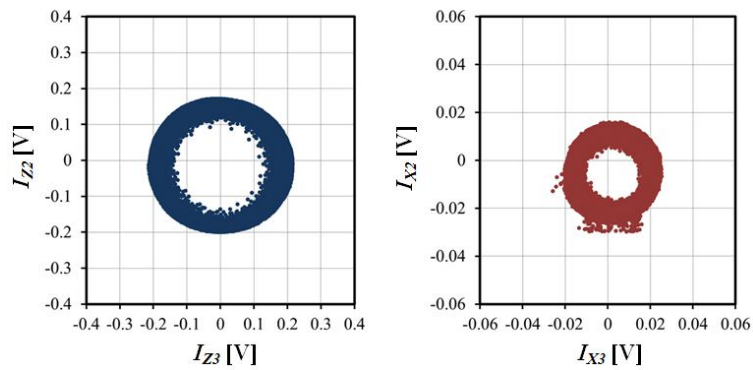
Axial (Z-axis) motion   Radial (X-axis) motion

(a) Lissajous diagrams
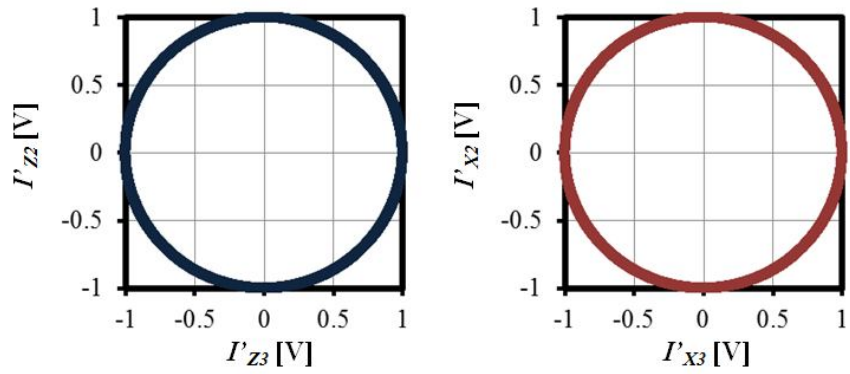
Axial (Z-axis) motion   Radial (X-axis) motion

(b) Normalized Lissajous diagrams
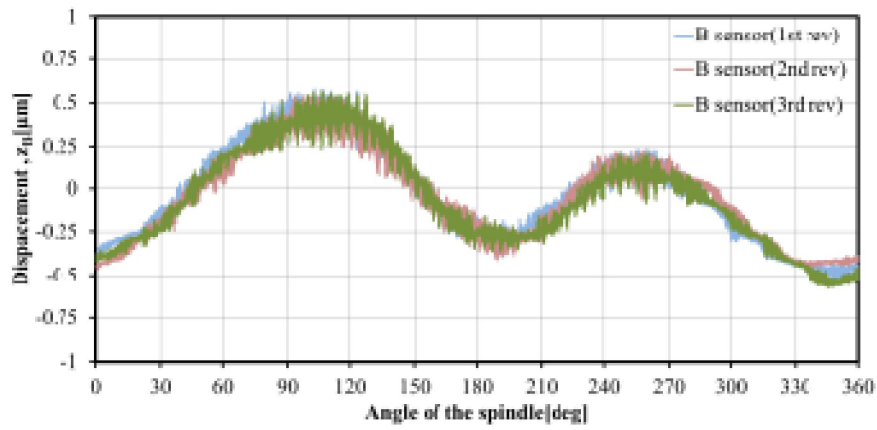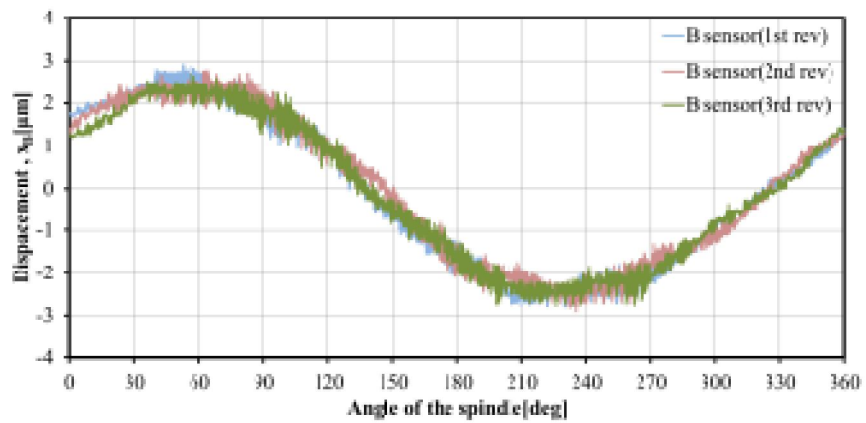
Axial (Z-axis) motion

Radial (X-axis) motion

(c) Axial (Z-axis) and radial (X-axis) motion

Fig. 5.26 Measurement results of the spindle motion from optical sensor B
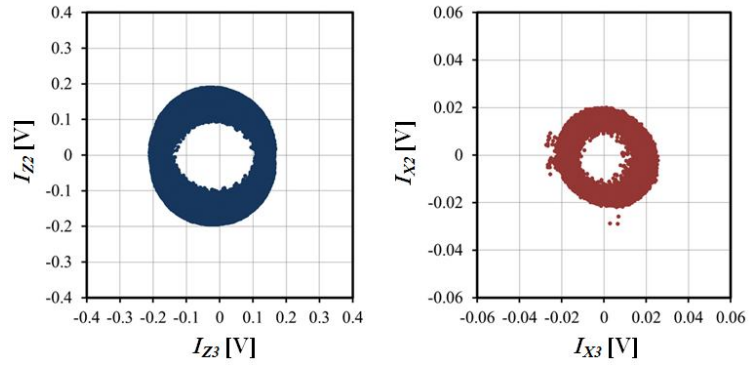
Axial (Z-axis) motion   Radial (X-axis) motion

(a) Lissajous diagrams
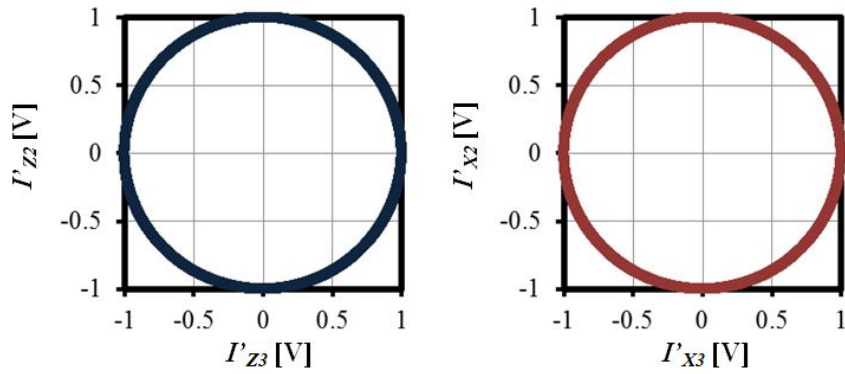
Axial (Z-axis) motion   Radial (X-axis) motion

(b) Normalized Lissajous diagrams
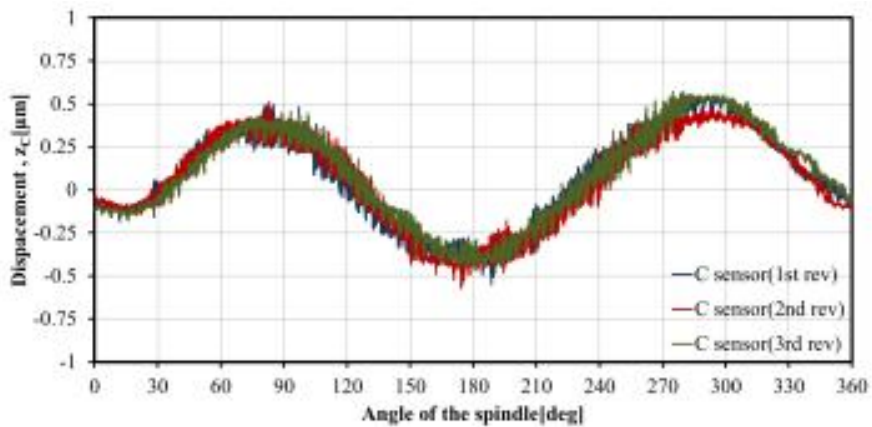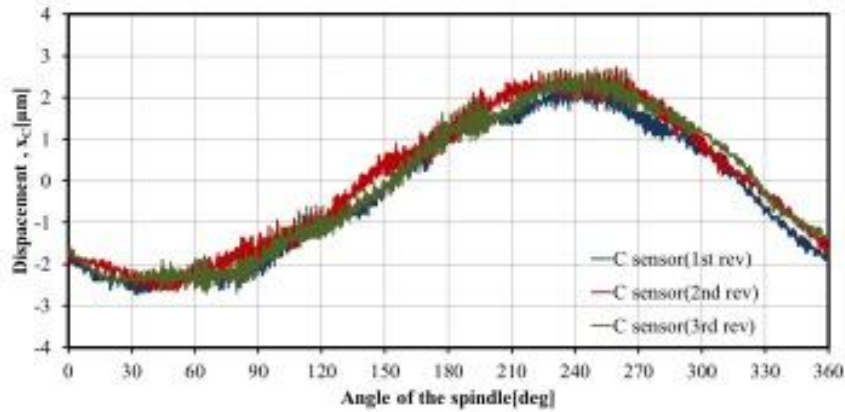
Axial (Z-axis) motion

Radial (X-axis) motion

(c) Axial (Z-axis) and radial (X-axis) motion

Fig. 5.27 Measurement results of the spindle motion from optical sensor C

Figures 5.25, 5.26, and 5.27 show the measurement results of the spindle motion from optical sensors A, B, and C, respectively. In Figs. 5.25, 5.26, and 5.27 (a) shows the Lissajous diagram of the axial (Z-axis) and radial (X- or Y-axis) motion, (b) shows the normal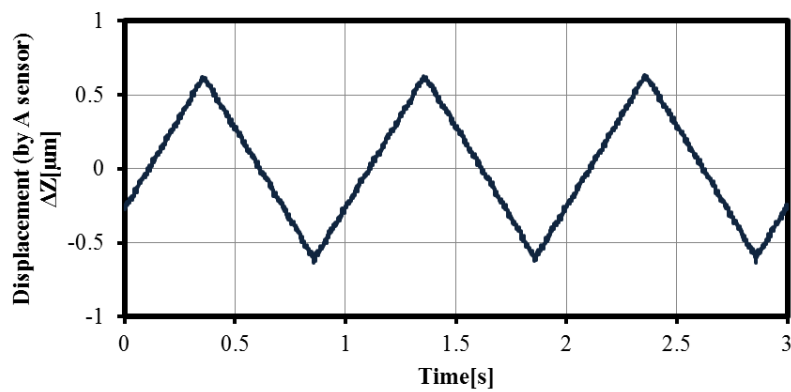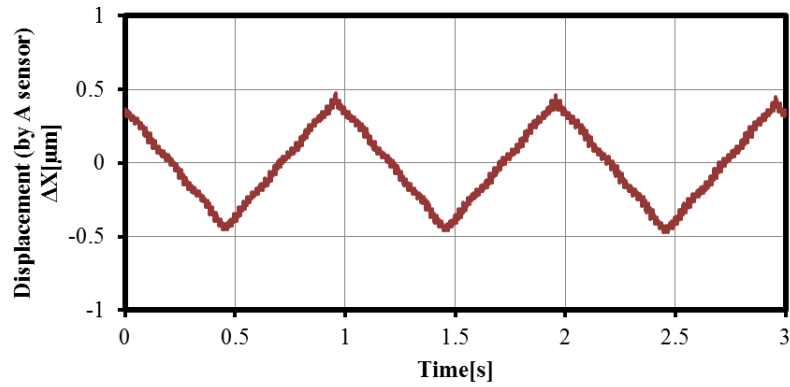ized Lissajous diagrams of the axial (Z-axis) and radial (X- or Y-axis) motion, and (c) show the axial (Z-axis) and radial (X- or Y-axis) motion. Form the measurement results of the three optical sensors, the axial (Z-axis) and radial (X- or Y-axis) motion of the spindle are approximately 1 μm and 5 μm, respectively. Because the radial motion has a component whose period is the same as that of the rotations, the centering error mainly affects the radial motion.
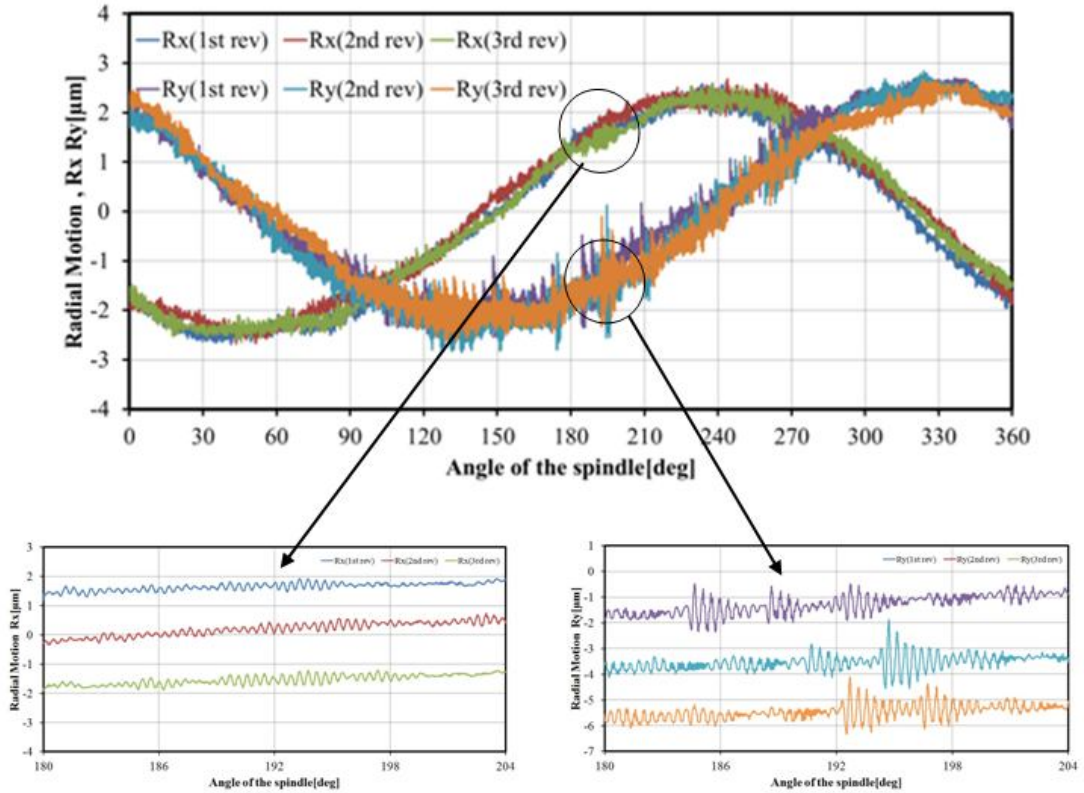
(a) Radial motion R_x, R_y
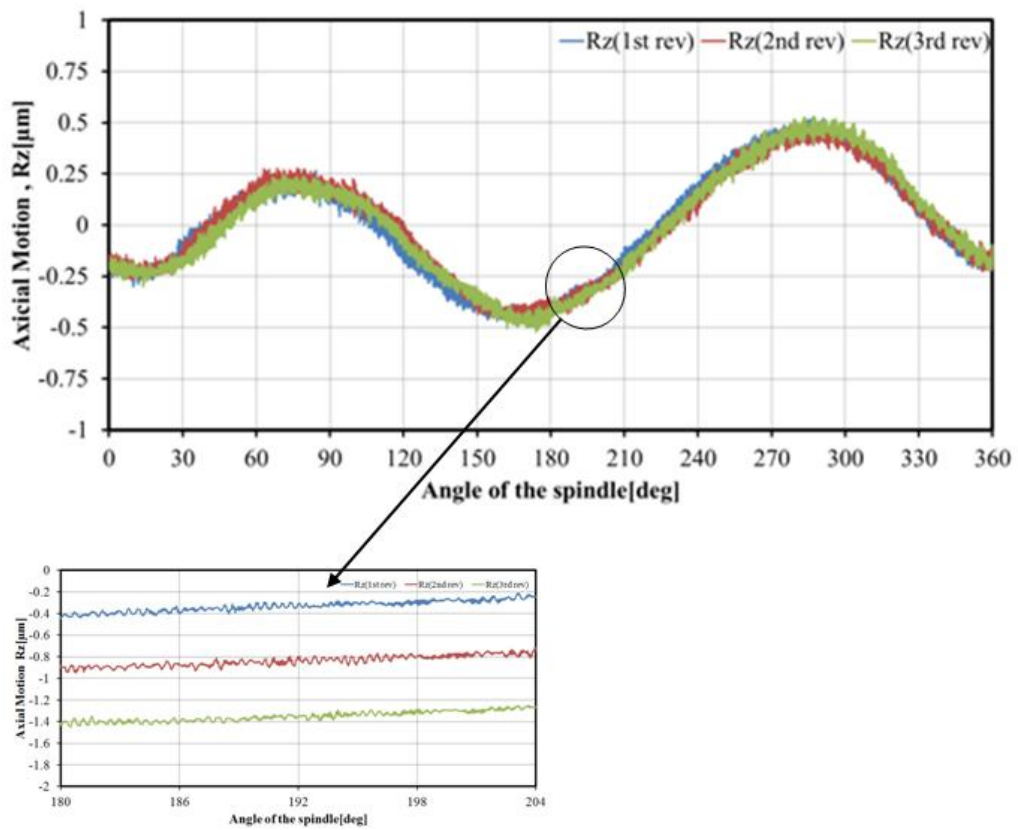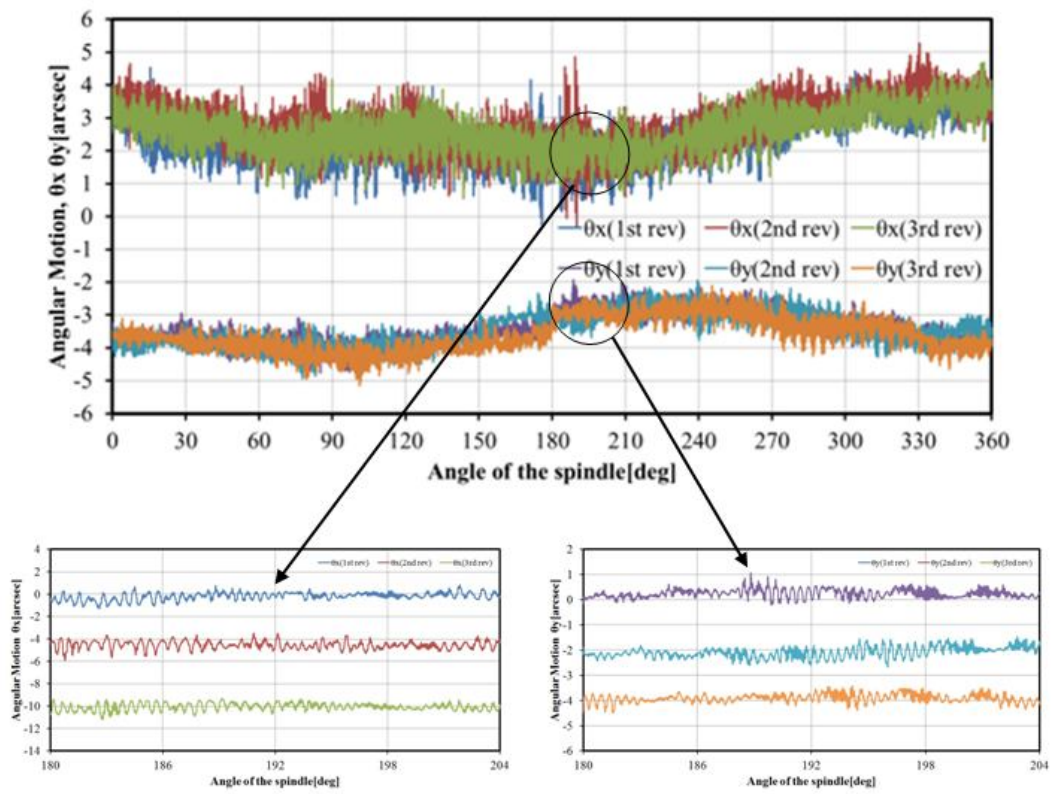
(b) Axial motion R_z

(c) Angular motion θ_x , θ_y

Fig. 5.28 Radial, axial, and angular motion of spindle and their magnified figures
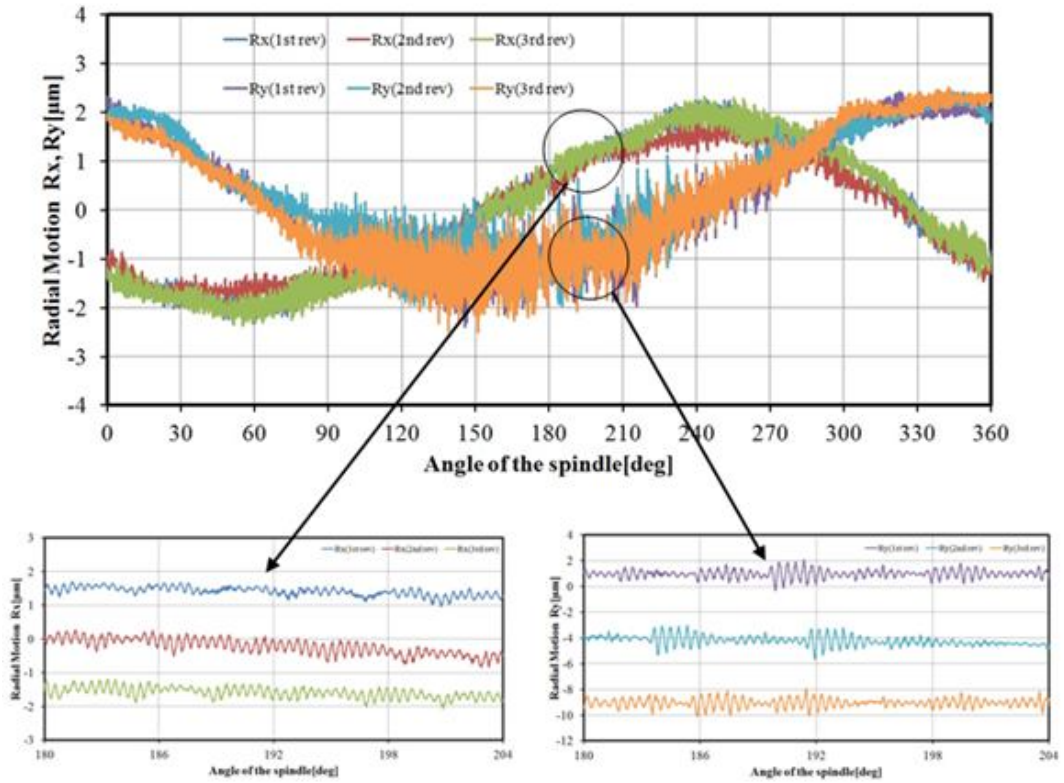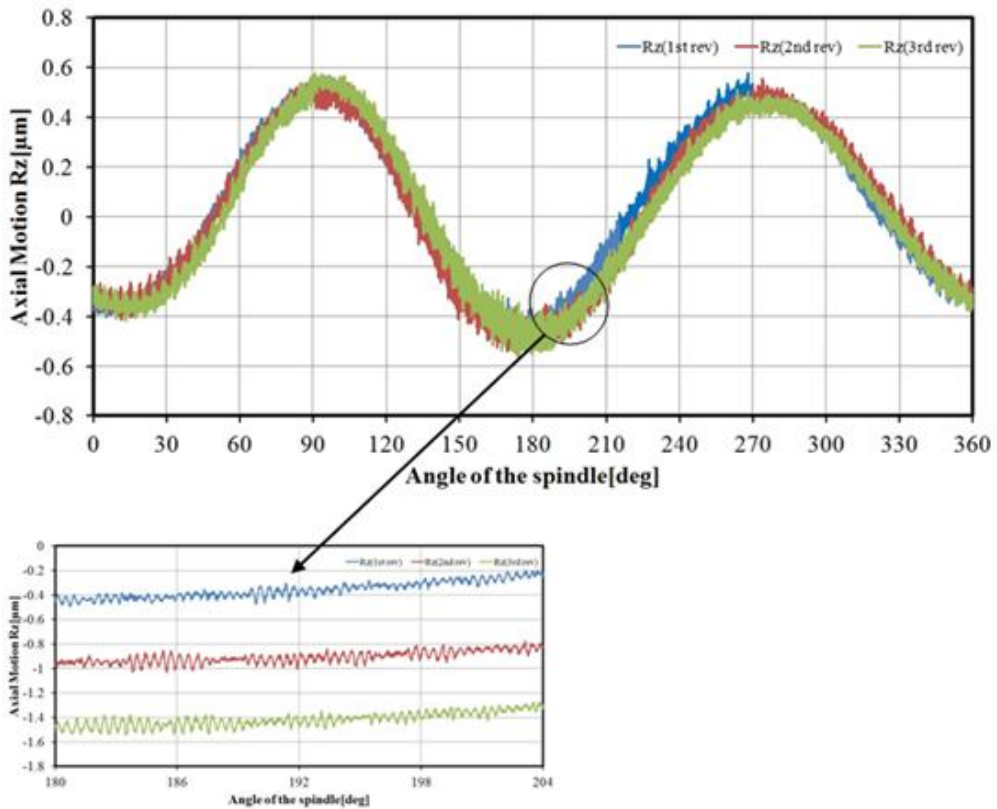
(a) Radial motion R_x, R_y

(b) Axial motion R_z

(c) Angular motion θ_x, θ_y
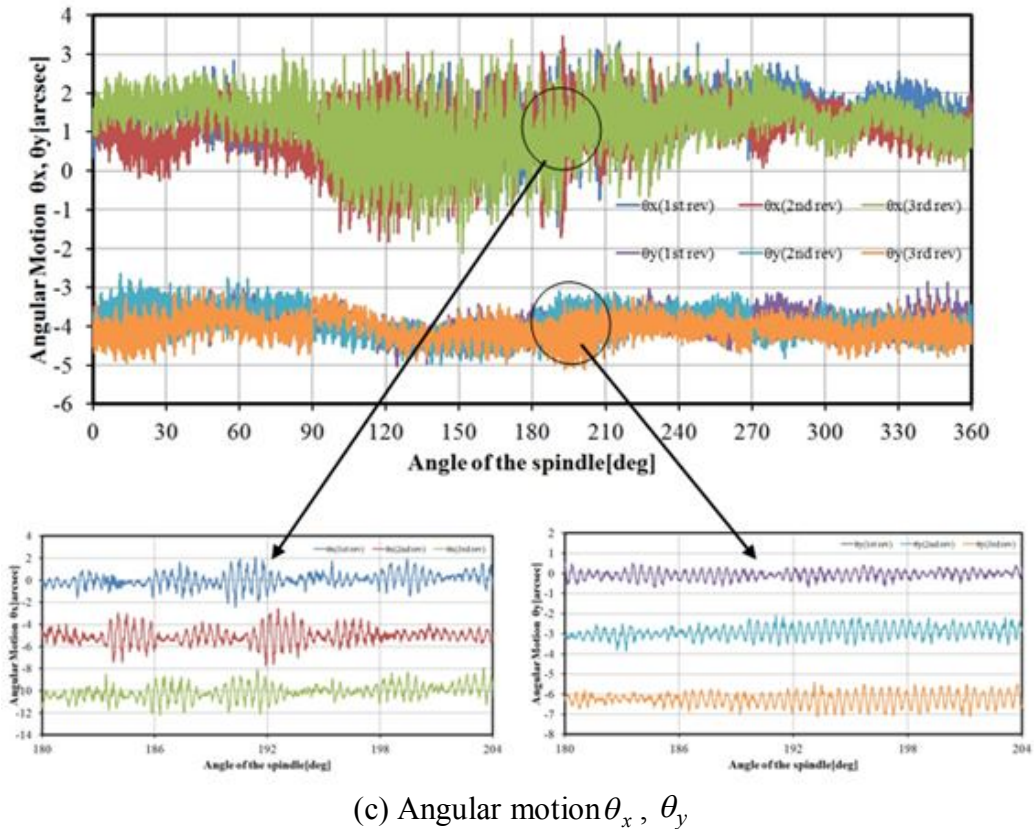
Fig. 5.29 Radial, axial, and angular motion of spindle. These results were obtained on a different day from those in Fig. 5.28.

Figures 5.28 and 5.29 show two concurrent measurement results of radial (R_x and R_y), axial (R_z), and angular (θ_x and θ_y) motion obtained on different days. In Figs. 5.28 and 5.29, magnified figures of the radial, axial, and angular motion are also shown. In the magnified figures, the vibrations, whose frequency is approximately 54 Hz, are clearly seen (there are approximately 54 periods in 24 degrees (which is equal to 1 s)). Comparing Figs. 5.28 and 5.29, it is note that the spindle motion does not repeat itself, and the spindle motion changes day by day. Figures 5.28 and 5.29 show that the radial (R_x and R_y), axial (R_z), and angular (θ_x and θ_y) motion are approximately 5 µm, 0.5~1µm and 1~3 arcsec, respectively. If the displacement is larger than $\dfrac{\lambda}{2}$ or $\dfrac{d}{2}$ for the sampling time (which is equal to 1/sampling rate (f_s)), it is impossible to interpolate or determine the displacement

using Lissajous diagram. The relationship between the maximum speed (v_{max}) and the sampling rate (f_s) is described by

$$\frac{v_{max}}{f_s} < \frac{\lambda}{2} \text{ or } \frac{d}{2}. \tag{5.10}$$

In the measurement $f_s = 10$ kHz, $\lambda = 635$ nm and $d = 2$ μm, then

$$v_{max} < 3.18 \text{ mm/s (axial)} \tag{5.11}$$

$$v_{max} < 10 \text{ mm/s (radial).} \tag{5.12}$$

From the magnified figure shown in Fig. 5.28 (a), the maximum vibration speed is approximately 0.3 mm/s ($\approx$ 3 μm × 2 × 54 Hz), therefore we could obtain the vibration speed by our proposed method. However, we can estimate the measurement repeatability using the measurement result of spindle radial motion. Equation (2.1) in chapter 2 shows that radial motion along the X-axis can be obtained as follows:

$$R_x = \frac{1}{2}(x_B + x_C), \tag{5.13}$$

where x_B and x_C are the radial motion detected by optical sensors B and C, respectively.

From Eq. (5.13), we assume that the concentric circle grating has no profile error. If we assume that the concentric circle grating has a roundness profile error, $r(\theta)$, the output signal of optical sensors B and C, S_B and S_C, can be described as

$$S_B = r(\theta) + x(\theta), \tag{5.14}$$

$$S_C = -r(\theta - \pi) + x(\theta). \tag{5.15}$$

When we consider the difference between the Eqs. (5.14) and (5.15), the measurement repeatability can be estimated from the roundness profile of the concentric circle grating as follows:

$$S_B - S_C = r(\theta) + r(\theta - \pi). \tag{5.16}$$

From Eq. (5.16), the even components of the roundness profile of the concentric circle grating are obtained.
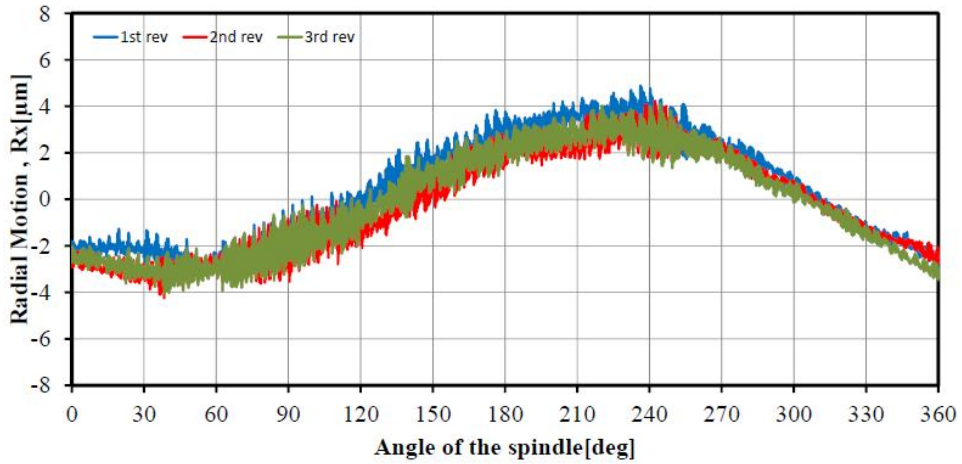
(a) Roundness profile
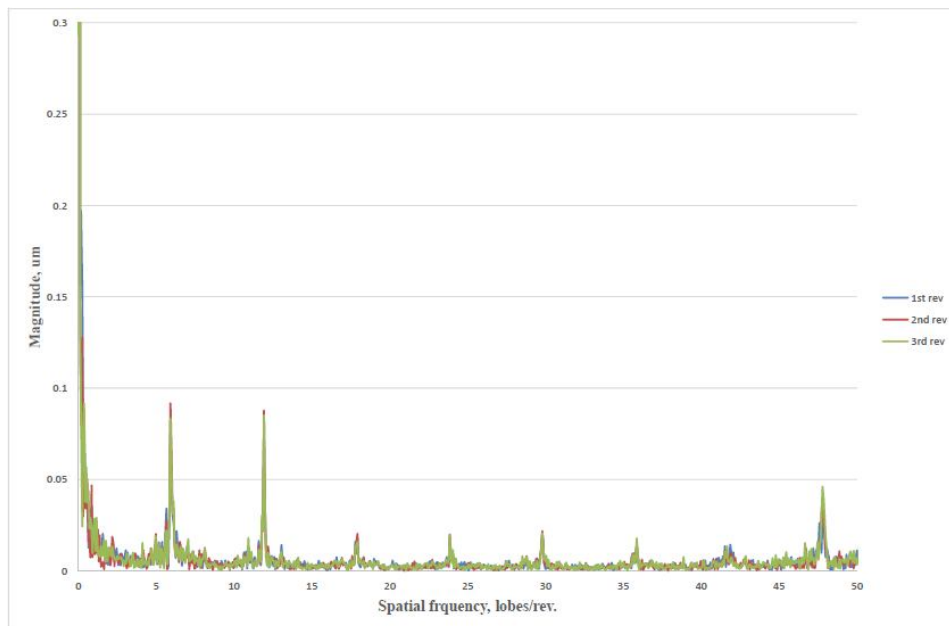
(b) FFT results

Fig. 5.30 Measurement repeatability results from the roundness profile of the concentric circle grating
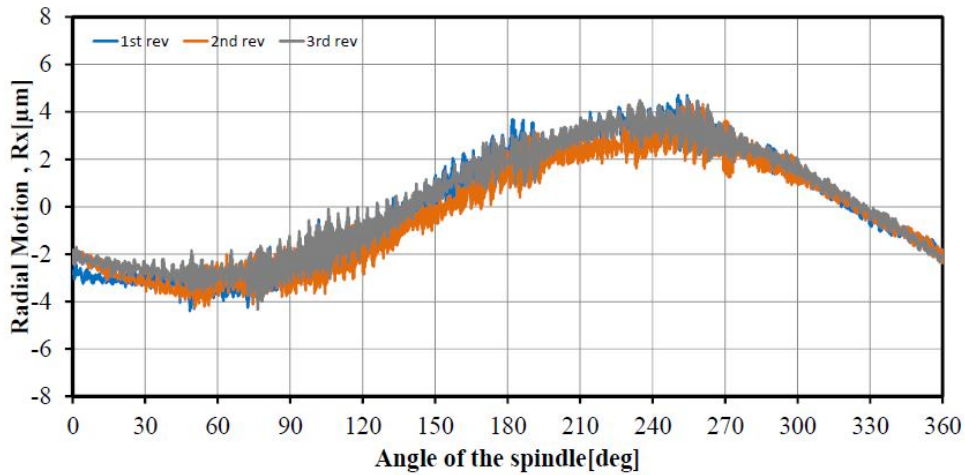
(a) Roundness profile
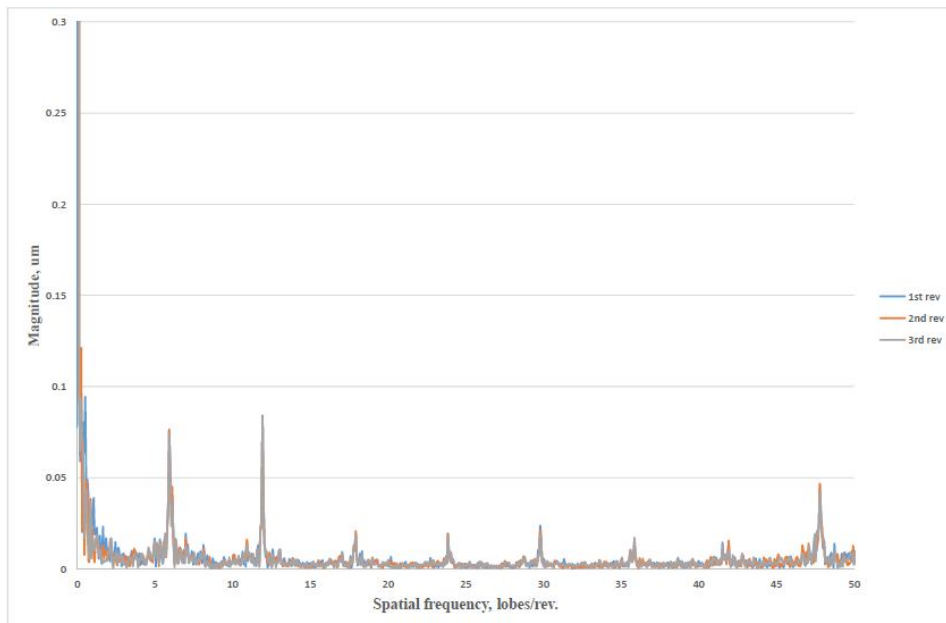
(b) FFT results

Fig. 5.31 Measurement repeatability results from the roundness profile of the concentric circle grating. These results were obtained on a different day from those in Fig. 5.30.

Figures 5.30 and 5.31 show two measurement repeatability results of the roundness profile of the concentric circle grating, obtained on different days. In Figs. 5.30 and 5.31, (a) shows the roundness profile of the concentric circle grating, and a large roundness profile of approximately 8 μm is obtained. In Figs. 5.30 and 5.31, (b) shows the roundness

profile of the concentric circle grating from the FFT analysis, and the even components, 0 lobes/rev., 6 lobes/rev., 12 lobes/rev.,. . . , obtained from the roundness profile of the concentric circle grating. Therefore, when these results include other components, these components indicate to repeatability. The experimental results show that the concurrent measurements of the radial, axial, and angular motion of the spindle were successfully attained.

Chapter 6

Discussion, overall conclusions, and future works

In this chapter, we discuss and summarize the experimental results obtained from this study. We constructed and examined the performance of a prototype instrument for a spindle motion measurement system using three optical sensors and a concentric circle grating. The quadrature detection and phase modulation techniques are also applied to the measurement system. We then suggested some modifications to our setup that should further improve our measurement system to adapt the experiment for use in the spindle metrology. We will finally present some plans for future studies to improve the spindle measurement system.

6.1 Discussion

This thesis presented a novel method of the concurrent measurement of spindle radial, axial, and angular motion using a concentric circle grating and phase modulation interferometers. Our study can be used to support the rotary spindle measurement of ultra-precision fabrication machines with high speed.

In the first works, we presented the concurrent measurement of spindle radial, axial, and angular motion using a concentric circle grating and quadrature detection technique. In this technique, four photodetectors are applied to measure the interference signal of the axial (Z-axis) and radial (X-axis) motion. For a small motion error, two-axes displacement measuring interferometers (Michelson and grating interferometers) could measure the axial (Z-axis) and radial (X-axis) motion by obtaining the Lissajous diagram. To reduce the distance between the grating and photodetector PD1 (or PD2) for the ultra-precise spindle measurement, the compact-size optical sensor is fabricated and tested. In the optical sensor, to reduce the crosstalk error between Michelson and grating interferometers down to 10^{-4} order, the grating plane must be aligned parallel to the XY plane within an error of 10 arcsec [106]. However, the center of the concentric circle

grating was not sufficiently aligned to the spindle rotation center, and the tilting between the grating plane and the XY plane was larger than 10 arcsec. Some frequency components (such as vibration and DC offset) were obtained in the displacement signal of spindle motion. Therefore, we could not obtain the Lissajous diagram for the concurrent measurement of spindle radial, axial, and angular motion using three optical sensors as shown in the measurement results. Since we have improved the alignment techniques for the centering between the center of the concentric circle grating and the spindle rotation axis, and the tilting between the grating plane and the XY plane (centering error less than 1 μm, tilting error less than 10 arcsec), the optical sensor can observe the displacement signal. However, the concurrent measurement of spindle motion using the quadrature detection technique has some disadvantages, such the use of many optical elements and photodetectors in one optical sensor, resulting in difficultly of alignment and adjustment all optical elements in the optical sensor, and difficulty in adjustment the sensitivity of the photodetector. Therefore, a novel technique for the concurrent measurement of spindle motion using a phase modulation technique was proposed and developed to solve these problems.

In the second study, we presented the concurrent measurement of spindle radial, axial, and angular motion using a concentric circle grating and the quadrature detection technique to solve the previous problems. In this technique, a sinusoidal angular modulation frequency is applied to the light source from a laser diode (LD). The Lissajous diagram can be obtained from two photodetectors. Even though the electronics circuit in the interferometer is complicated, we can reduce the number of optical elements required for the interpolation. However, due to the limited of frequency range of the digital and analog lock-in amplifiers, the maximum modulated frequency which can be applied to the light source is up to 33 kHz. By evaluating the performance of two-axes displacement-measuring interferometers (Michelson and grating interferometers), we could measure the axial (Z-axis) and radial (X-axis) motion by obtaining the Lissajous diagram. If there is deformation of the Lissajous diagram due to variations of the laser source intensity and other causes, a normalized Lissajous diagram can be obtained. The high-rigidity compact optical sensor is also fabricated and its performance tested. The measurement results show that three optical sensors have good reproducibility when the small motion of the XZ-PZT stage is measured. In the previous study [113], we estimated that the measurement uncertainties for Michelson and grating interferometers are less than

0.1 μm. From the measurement results of spindle motion using three optical sensors and the concentric circle grating, we attained the concurrent measurements of spindle radial, axial, and angular motions at a low speed of 4 rpm with a sinusoidal phase modulation frequency of 33 kHz. However, the radial motion has a component whose period is the same as that of the rotation; therefore, the centering error mostly affects the radial motion. In the concurrent measurement of spindle radial, axial, and angular motion of two measurement results which are obtained on a different days. Magnified figures of radial, axial, and angular motion are also shown to clarify the spindle vibration, whose frequency is approximately 54Hz. In the magnified figures, the vibrations, whose frequency is approximately 54 Hz, are clearly seen (There are approximately 54 periods in 24 degrees (which is equal to 1 s)). By comparing of the two measurement results, we note that the spindle motion reading are not repeatable; therefore, we could not estimate the measurement repeatability (or uncertainty) using this spindle. In this method, if the displacement is larger than wavelength/2 or grating pitch/2 for the sampling time, it is impossible to interpolate with the Lissajous diagram. The maximum detectable speeds for X- (or Y-) and Z-axes are 10 mm/s and 3.18 mm/s, respectively. From the magnified figures, the maximum vibration speed is approximately 0.3 mm/s ($\approx$ 3 μm $\times$ 2 $\times$ 54 Hz), therefore we could obtain the vibration speed by our proposed method. However, the measurement repeatability can be judged from the roundness profile of the concentric circle grating. If we assume that the concentric circle grating has a roundness profile error, the even components of the roundness profile (0 lobes/rev., 6 lobes/rev., 12 lobes/rev.,. . . ,) are obtained. Therefore, when these results include other components, these components indicate the repeatability. The experimental results show that the concurrent measurements of the spindle radial, axial, and angular motions were successfully attained.

6.2 Overall conclusions

Three approaches by the concurrent measurement of spindle radial, axial, and angular motions using a concentric circle grating and phase modulation interferometers were introduced in the thesis. Each approach was evaluated in papers published in International Journal of Surface Science and Engineering, International Journal of Automation Technology, and Journal of Measurement Science Technology. In the first approach, the measurement principle of two-axes displacement measuring interferometers (Michelson

and grating interferometers) using a one-dimensional grating is clarified. The error analysis of the interferometer is performed from the views point of radial, axial, and angular motion measurements [106]. In the second approach, the measurement system of spindle motion using one optical sensor and the concentric circle grating was fabricated and examined. The displacement (Lissajous diagram) can be obtained when we add a small modulation to the frequency of the light source. Using one optical sensor, we could measure spindle radial and axial motion concurrently [113]. In the third approach, the concurrent measurement system of spindle motion using three optical sensors was fabricated and examined. Using three optical sensors and the concentric circle grating, we attained the concurrent measurements of spindle radial, axial, and angular motion at a low speed of 4 rpm with a sinusoidal phase modulation frequency of 33 kHz. The result of this experiment was reported in a paper published in the journal of Measurement Science and Technology [122].

6.3 Future works

Based on the above results, we are planning to increase the modulation frequency up to 10 MHz to measure the spindle motion at a high speed of 100 krpm, and we will test the performance of this system in the near future. Regarding the measurement range of our method, there is no limitation for displacement measurement if the spindle motion speed does not exceed the detectable speed. However, the crosstalk error between the Michelson and grating interferometers must be reduced to increase the measurement range of the angle. In the previous paper [109], we clarified that one of the causes of the interpolation error for two interferometers is polarization mixing. However, to reduce the interpolation error due to amplitude modulation appearing in the laser diode, we need to use the compensation method. We will discuss a theoretical and experimental approach for compensating the interpolation errors due to polarization mixing and amplitude modulation in the near future. To remove the air turbulence effect on the measurement system, we will employ a stabilized chamber. For compensation of the artifact form errors (roundness and surface flatness) of the concentric circle grating in the measurement, the concentric circle grating needs to be calibrated. We are also planning to use some error separation methods, such as the reversal method, to improve the measurement accuracy. A grating pitch of less than 2 μm is favorable to improve the measurement resolution of radial motion. In that case, we must pay attention when selecting the wavelength of the

LD, the diffraction order, and the diffraction angle. We are also planning to use a light source with a shorter wavelength. Finally, we should compare another spindle motion measurement method with the proposed method in the near future.

Appendix A

Spindle error separation techniques

In the conventional measurement of spindle radial error motion, a displacement sensor targeting a rotating surface measures the combined contribution of the spindle error and the imperfections of the target surface; therefore, an error separation method is necessary. In this section, the Donaldson reversal, multiprobe, and the multistep methods are described.

A.1 Reversal method

Self-calibration can be carried out by error separation using a reversal method. The Donaldson reversal method [10], which is the rotational equivalent of the well-known straightedge reversal, is shown schematically in Fig. A.1. To calculate the error of the radial spindle motion, this method requires two measurements to separate a single component of spindle error (such as, radial or face error motion) from artifact error.
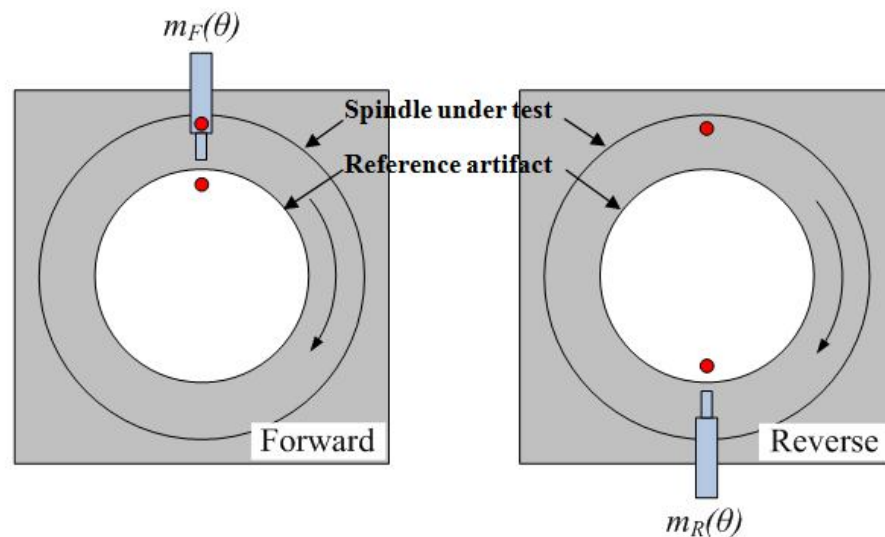
Fig. A.1 Schematic of the Donaldson reversal method

In the first measurement, the angular orientations of the spindle stator, the artifact, and the displacement sensor are aligned for the normal position measurement. In the second measurement, the displacement sensor and the artifact are rotated 180° with

respect to the spindle rotor. The two measurements $m_F(\theta)$ and $m_R(\theta)$ shown in Eqs. (A.1) and (A.2) are the sum of the artifact's profile $P(\theta)$ and radial error motion $S(\theta)$.

$$m_F(\theta) = P(\theta) + S(\theta) \tag{A.1}$$

$$m_R(\theta) = P(\theta) - S(\theta) \tag{A.2}$$

The equations above change the sign of the artifact's form error within the two measurements. Adding and subtracting the two equations enable the computation of the artifact's profile $P(\theta)$ and spindle error motion $S(\theta)$ as the simple relationship shown in Eqs. (A.3) and (A.4).

$$P(\theta) = \frac{m_F(\theta) + m_R(\theta)}{2} \tag{A.3}$$

$$S(\theta) = \frac{m_F(\theta) - m_R(\theta)}{2} \tag{A.4}$$

A.2 Multiprobe method
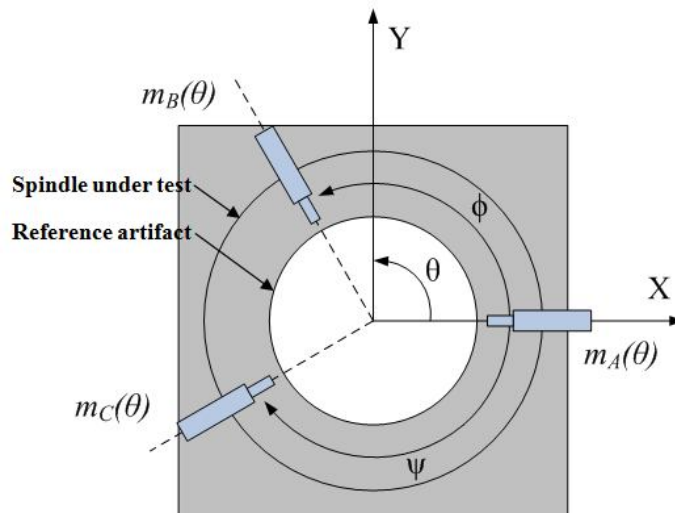
Fig. A.2 Schematic of the three-probe error separation method

The multiprobe error separation method requires three or more probes to simultaneously measure the combination of the spindle error motion and the artifact form error. Whitehouse published detailed analyses of the capability of multiprobe error separation using three or more displacement sensors targeting an artifact [16]. In this method, the probes and the artifact are not moved, but they must be properly arranged. Figure A.2 shows a schematic of the measurement with three displacement sensors that simultaneously record $m_A(\theta)$, $m_B(\theta)$, and $m_C(\theta)$. Sensors B and C are separated in the fixed XY-plane from sensor A by angles ϕ and ψ, respectively. As shown in Eqs. (A.5) to (A.7), the measurements recorded by the three displacement sensors are the sum of the roundness error $P(\theta)$, including a phase shift due to the sensor location, and the $x(\theta)$ and $y(\theta)$ components of the spindle error motion,

$$m_A(\theta) = P(\theta) + x(\theta) , \tag{A.5}$$

$$m_B(\theta) = P(\theta - \phi) + x(\theta)\cos\phi + y(\theta)\sin\phi , \tag{A.6}$$

$$m_C(\theta) = P(\theta + \psi) + x(\theta)\cos\psi - y(\theta)\sin\psi , \tag{A.7}$$

where $M(\theta)$ is defined as a linear combination of the three distinct measurements using coefficients of unity, a, and b, as shown in Eq. (A.8). The unknown coefficients a and b are determined by solving Eqs. (A.9) and (A.10) simultaneously.

$$M(\theta) = m_A(\theta) + am_B(\theta) + bm_C(\theta) \tag{A.8}$$

$$a\cos\phi + b\cos\psi + 1 = 0 \tag{A.9}$$

$$a\sin\phi - b\sin\psi = 0 \tag{A.10}$$

The roundness of the artifact is modeled as an infinite Fourier series as shown in the following equation:

$$P(\theta) = \sum_{k=1}^{\infty} (A_k \cos k\theta + B_k \sin k\theta) . \tag{A.11}$$

Equation (A.12) shows the result when the series representation for the artifact roundness $P(\theta)$ is substituted into the summed measurement $M(\theta)$, angle addition trigonometry identities are applied, and the common terms of $A_k \cos k\theta$, $A_k \sin k\theta$, $B_k \cos k\theta$ and $B_k \sin k\theta$ are collected.

$$M(\theta) = m_A(\theta) + a m_B(\theta) + b m_C(\theta)$$

$$= \sum_{k=1}^{\infty} A_k (1 + a \cos k\phi + b \cos k\psi) \cos k\theta + \sum_{k=1}^{\infty} A_k (a \sin k\phi - b \sin k\psi) \sin k\theta +$$

$$\sum_{k=1}^{\infty} B_k (1 + a \cos k\phi + b \cos k\psi) \sin k\theta + \sum_{k=1}^{\infty} B_k (b \sin k\psi - a \sin k\phi) \cos k\theta \qquad \text{(A.12)}$$

At this point, $\alpha_k = 1 + a \cos k\phi + b \cos k\psi$ and $\beta_k = b \sin k\psi - a \sin k\phi$ may be computed, so the remaining step is to compare the terms of Eq. (A.12) with the Fourier coefficients of $M(\theta)$ (F_k and G_k, as defined in Eq. (A.13)) to determine A_k and B_k. Therefore, Eq. (A.14) is solved for each term in the Fourier series.

$$M(\theta) = \sum_{k=1}^{\infty} (F_k \cos k\theta + G_k \sin k\theta) \qquad \text{(A.13)}$$

$$\begin{bmatrix} \alpha_k & \beta_k \\ -\beta_k & \alpha_k \end{bmatrix} \begin{Bmatrix} A_k \\ B_k \end{Bmatrix} = \begin{Bmatrix} F_k \\ G_k \end{Bmatrix} \qquad \text{(A.14)}$$

With A_k and B_k known, the artifact roundness $P(\theta)$ is fully defined. The roundness measurement is then used to determine the spindle error motion $S(\theta)$ as follows:

$$S(\theta) = m_A(\theta) - P(\theta). \qquad \text{(A.15)}$$

A.3 Multistep method

The multistep method requires many sets of measurements for measuring the spindle error motion. The indicator is stationary, while the artifact is sequentially indexed by 360° in a large, but flexible, number of equally spaced increments. Accuracy is improved using more measurements.
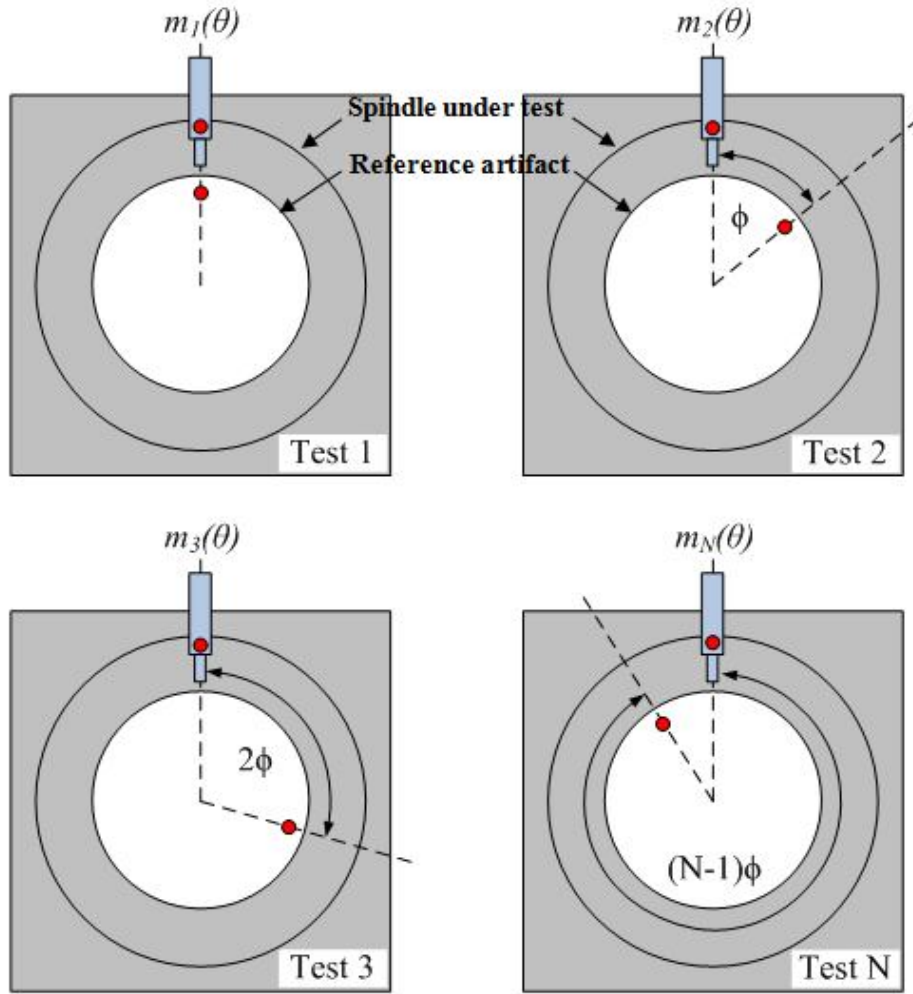
Fig. A.3 Schematic of the multistep error separation method

Figure A.3 shows a schematic of the multistep error separation method, in which measurements are carried out for each position as the artifact is indexed by N angular increments of ϕ relative to the spindle. A single, fixed sensor measures the displacements from the same orientation angle for all angular increments of the artifact. Therefore, each measurement includes the spindle radial error motion and the phase-shifted artifact form error. The analysis of the N measurements, as a function of the spindle rotor angle θ, is straightforward as shown in the following equations:

$$S(\theta) \cong \frac{1}{N} \sum_{j=1}^{N} m_j(\theta), \tag{A.16}$$

$$P(\theta) = m_1(\theta) - S(\theta). \tag{A.17}$$

A.4 Reversal separation method of the spindle radial motion measurement using three optical sensors
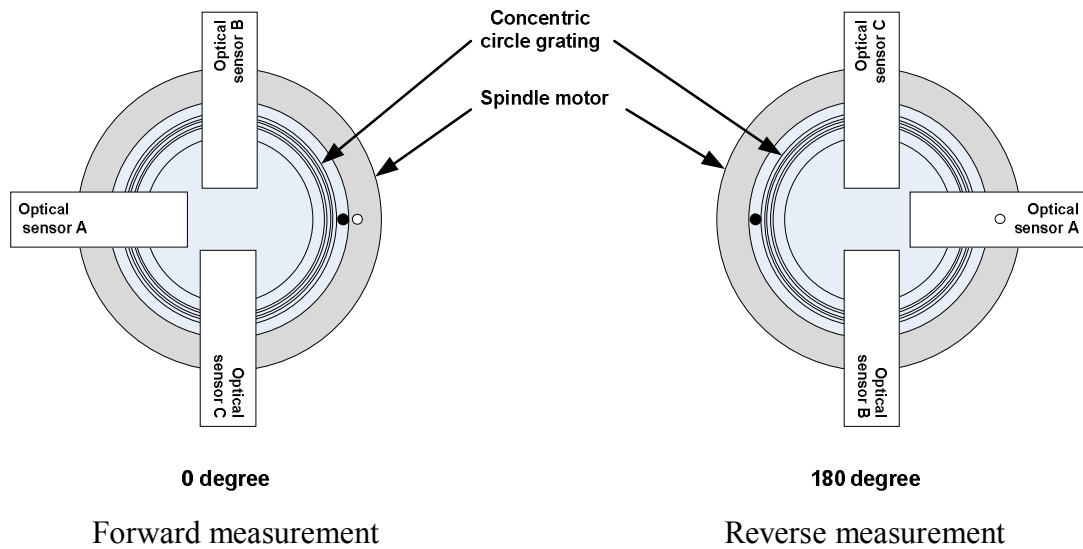
(a) Schematic diagram of the reversal method for the spindle radial motion measurement
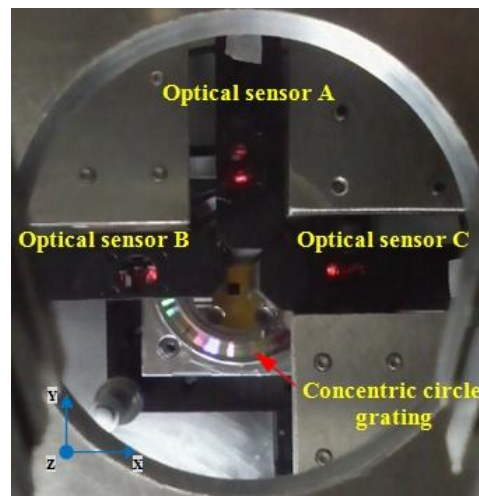
(b) Photograph of the experimental setup from the top view

Fig. A.4 Experimental setup of the reversal method for the spindle radial motion measurement using three optical sensors

To separate the centering error that affects the radial motion in the experimental results of chapter 5 (see Sect.5.4), we perform the error separation method of spindle

radial motion measurement using the Donaldson reversal method. The measurement principle this method is explained in appendix A.1. The experimental setup is shown in Fig. A.4. In the reversal method, three optical sensors and the concentric circle grating are set up to measure the spindle motion in the forward (0°) and reverse (180°) directions. The spindle is rotated at a speed of 4 rpm. We measure the spindle motion for three rotations (1 rotation = 15 s). Photodetector APD2 observes the radial (X- or Y-axis) displacement signal. The measurement conditions applied for the spindle motion are shown in Table 5.10 (chapter 5) and the measurement data is recorded in a PC using the Lab VIEW data acquisition program.
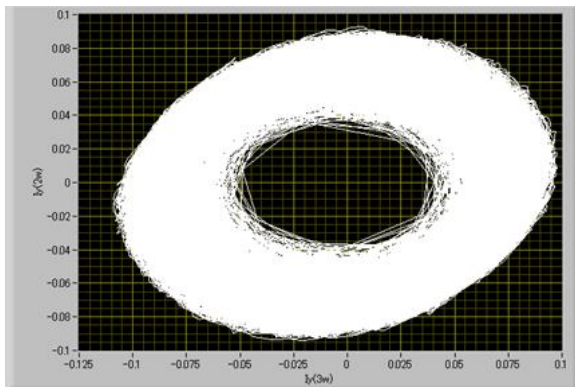
| Forward measurement | Reverse measurement |
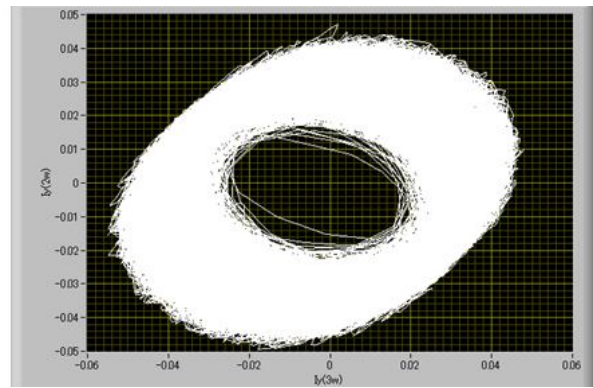
(a) Lissajous diagram of the forward and reverse measurements
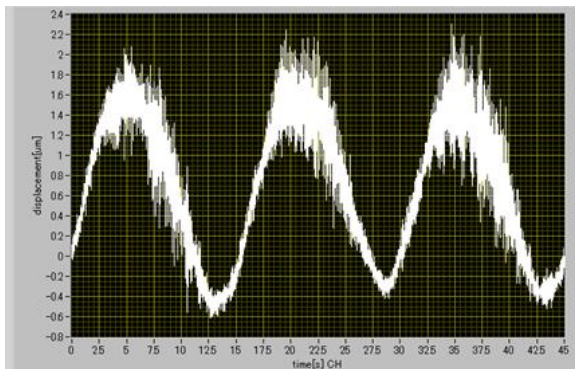
| Forward measurement | Reverse measurement |
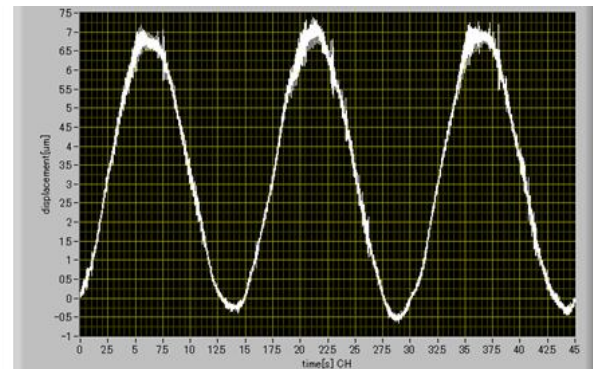
(b) Displacement of the forward and reverse measurements
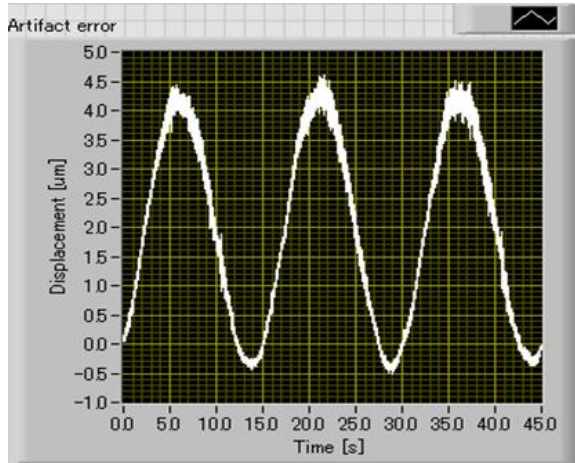
Artifact form error   Spindle motion error
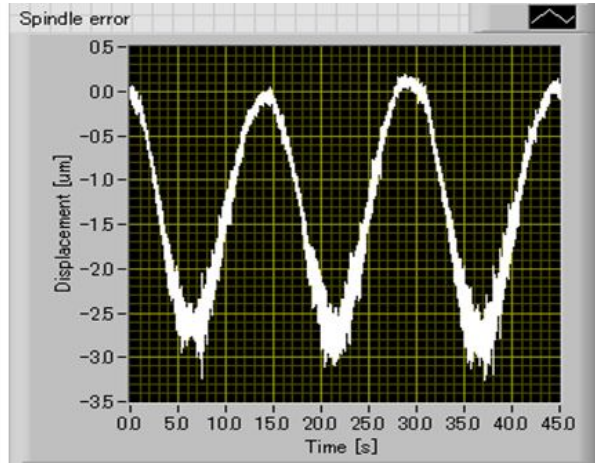
(c) Artifact form error and spindle motion error

Fig. A.5 Measurement results of the reversal method from optical sensor A

Forward measurement   Reverse measurement

(a) Lissajous diagram of the forward and reverse measurements

Forward measurement   Reverse measurement

(b) Displacement of the forward and reverse measurements

93
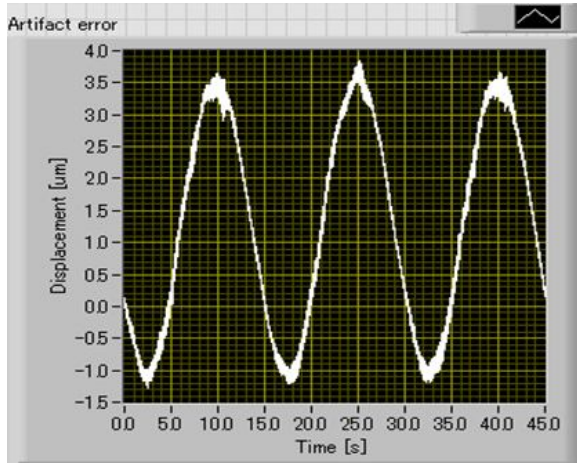
Artifact form error   Spindle motion error
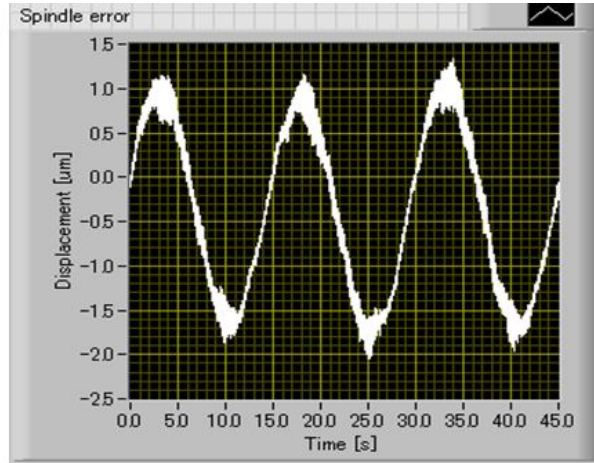
(c) Artifact form error and spindle motion error

Fig. A.6 Measurement results of the reversal method from optical sensor B
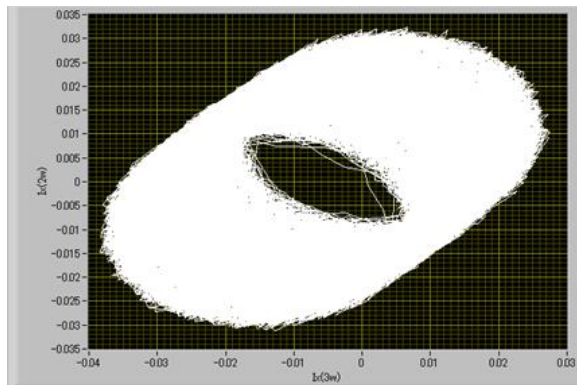
Forward measurement   Reverse measurement
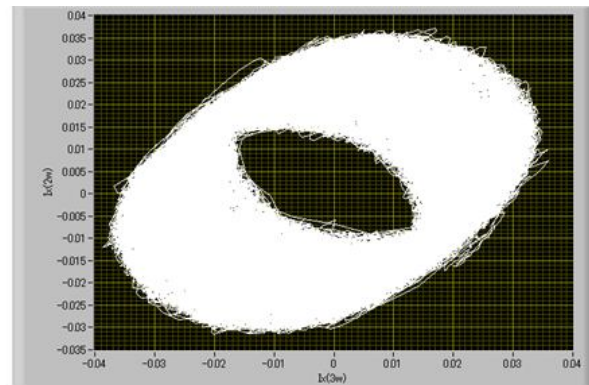
(a) Lissajous diagram of the forward and reverse measurements

Forward measurement   Reverse measurement

(b) Displacement of the forward and reverse measurements

94
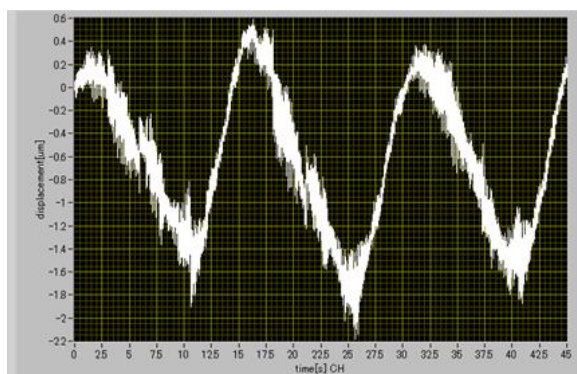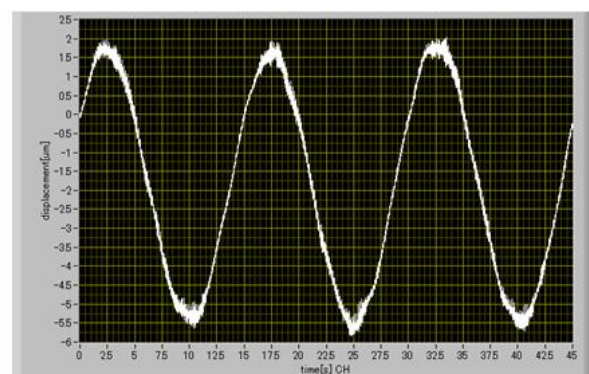
Artifact form error   Spindle motion error
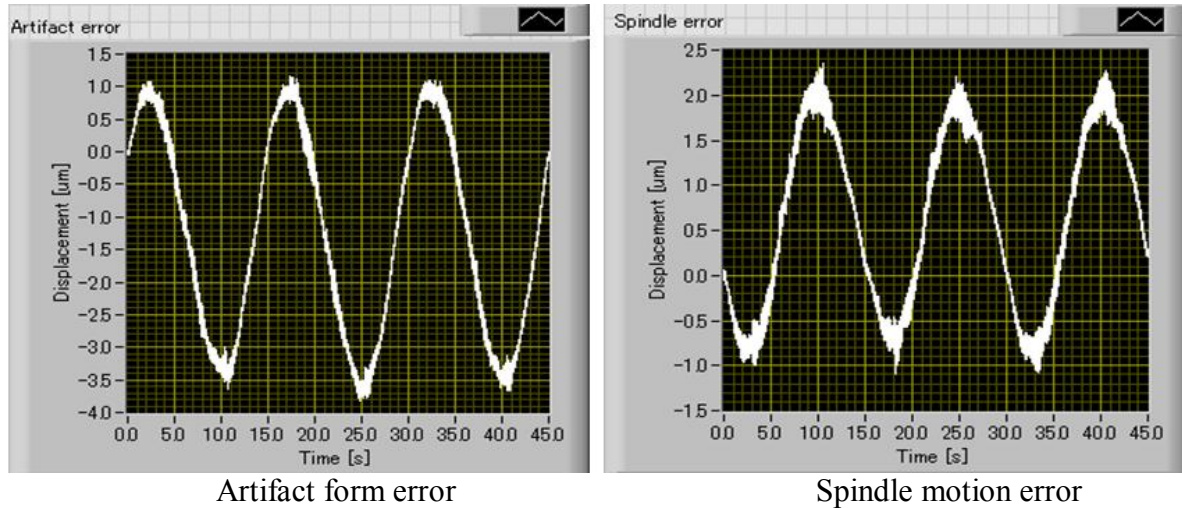
(c) Artifact form error and spindle motion error

Fig. A.7 Measurement results of the reversal method from optical sensor C

Figures A.5, A.6, and A.7 show the measurement results of the reversal method from optical sensors A, B, and C, respectively. In Figs. A.5, A.6, and A.7 (a) shows the Lissajous diagram of forward (0°) and reverse (180°) measurement, (b) shows the displacement of forward (0°) and reverse (180°) measurement, and (c) shows the artifact form error and the spindle motion error. From the measurement results of the three optical sensors, the artifact form error (including the centering error) and radial motion of the spindle are approximately 4.5 μm and 3 μm, respectively. By comparing the maximum error of spindle radial motion of 30 μm in Table 4.3 (chapter 4), the radial motion of this spindle is within the specification parameters. However, to compensate for the artifact form errors (roundness and surface flatness) of the concentric circle grating in the measurement, the concentric circle grating needs to be calibrated.

Appendix B

Bessel functions

Bessel functions, first defined by the mathematician Daniel Bernoulli and generalized by Friedrich Bessel, are the canonical solutions $y(x)$ of Bessel's differential equation as follows:

$$x^2 \frac{d^2 y}{dx^2} + x \frac{dy}{dx} + (x^2 - n^2)y = 0, \tag{B.1}$$

where n is a non-negative real number. The solutions of this equation are called Bessel functions of order n. Although the order n can be any real number, the scope of this section is limited to *non-negative integers*, i.e., $n = 1, 2, 3...$, unless specified otherwise. Since Bessel's differential equation is a second order ordinary differential equation, two sets of functions, Bessel functions of the first kind $J_n(x)$ and Bessel functions of the second kind (also known as the Weber functions) $Y_n(x)$, are requied to obtain the general solution

$$y(x) = c_1 J_n(x) + c_2 Y_n(x). \tag{B.2}$$

However, $Y_n(x)$ is *divergent* at $x = 0$. The associated coefficient c_2 is forced to be *zero* to obtain a physically meaningful result when there is no source or sink at $x = 0$. Figures B.1 and B.2 show the plots of Bessel functions of the first kind and second kind, respectively.
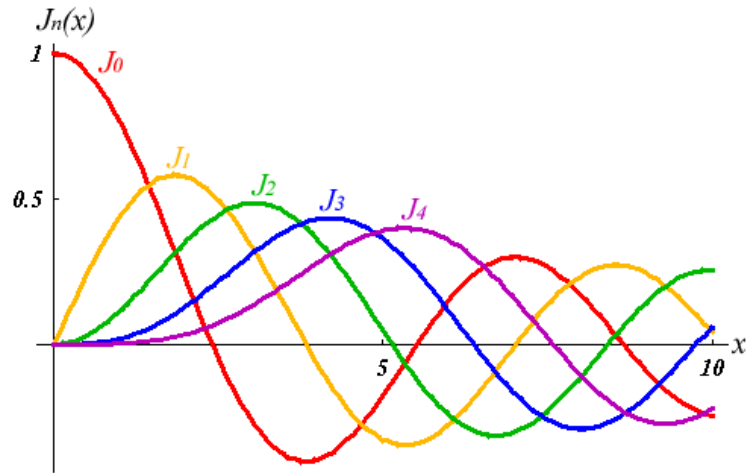
Fig. B.1 Plot of Bessel functions of the first kind
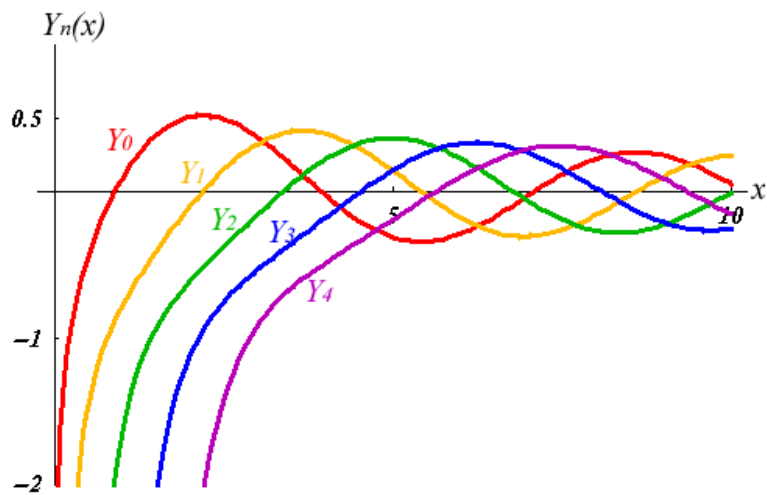
Fig. B.2 Plot of Bessel functions of the second kind

Another definition of the Bessel functions, for integer values of n, is possible using an integral representation as follows:

$$A_n(x) = \frac{1}{2} \int_{-\pi}^{\pi} e^{ix\sin(\theta) - in\theta} d\theta \ . \qquad (B.3)$$

To evaluate this integral, we use the Taylor series expansion of the exponent as

$$e^{ix\sin(\theta)} = \sum_{p=0}^{\infty} \frac{1}{p!} (ix\sin(\theta))^P = \sum_{p=0}^{\infty} \frac{1}{p!} \left(\frac{x}{2}\right)^P \left(e^{i\theta} - e^{-i\theta}\right)^P \ . \qquad (B.4)$$

Here, note that the integral

$$I_{p,\pi} = \frac{1}{2\pi} \int_{-\pi}^{\pi} (e^{i\theta} - e^{-i\theta})^P e^{-in\theta} d\theta = 0 \; ; \quad \text{if} \quad p < 0 .$$ (B.5)

Then, we write $p - n + q$. The integrand in Eq. (B.5) can be represented in the form

$$\frac{1}{2\pi} (e^{i\theta} - e^{-i\theta})^{n+q} e^{-in\theta} - (1 - e^{-2i\theta})^n (e^{i\theta} - e^{-i\theta})^q .$$ (B.6)

Suppose that q is odd and denote as $q - 2k + 1$. All terms in the first parentheses are even powers of $e^{-i\theta}$, while all terms in the second parentheses are odd powers (positive or negative) of $e^{-i\theta}$. As a result, the integrand is a linear combination of odd powers of $e^{-i\theta}$. Thus, the integral is zero, and we can put $q - 2k$. We obtain the following intermediate result:

$$A_n(x) = \left(\frac{x}{2}\right)^n \sum_{n=0}^{\infty} \frac{1}{(n+2k)} \left(\frac{x}{2}\right)^k I_{k,n} ,$$ (B.7)

where

$$I_{k,n} = \frac{1}{2\pi} \int_{-\pi}^{\pi} (e^{i\theta} - e^{-i\theta})^{n+2k} e^{-in\theta} d\theta .$$ (B.8)

To calculate $I_{k,n}$, we use the binominal expansion in the parentheses. In this expansion, we are only interested in the single term proportional to $e^{-in\theta}$. All other terms after multiplication by Eq. (B.8) and integration over θ are cancelled. Hence,

$$(e^{i\theta} - e^{-i\theta})^{n+2k} \approx \frac{(n+2k)!}{k!(n+k)!} (e^{i\theta})^{n+k} (-e^{-i\theta})^k = \frac{(-1)^k (n+2k)!}{k!(n+k)!} e^{in\theta}$$ (B.9)

and

$$I_{k,n} = \frac{(-1)^k (n+2k)!}{k!(n+k)!} .$$ (B.10)

By substituting Eq. (B.10) into Eq. (B.7), we finally obtain

$$A_n(x) = \left(\frac{x}{2}\right)^n \sum_{n=0}^{\infty} \frac{(-1)^k}{k!(n+k)!} \left(\frac{x}{2}\right)^k = J_n(x).$$ (B.11)

We obtain the integral representation for $J_n(x)$ as

$$J_n(x) = \frac{1}{2} \int_{-\pi}^{\pi} e^{ix\sin(\theta) - in\theta} d\theta.$$ (B.12)

This result is correct for positive n. And it note that

$$J_n(-x) = (-1)^n J_n(x).$$ (B.13)

Bessel functions of even order are even functions of z, while functions of odd order are odd functions. Now, we can determine $A_n(x)$ for negative n. Let us simultaneously change the signs of z and n.

$$A_{-n}(-x) = \frac{1}{2} \int_{-\pi}^{\pi} e^{-ix\sin(\theta) + in\theta} d\theta$$ (B.14)

By replacing $\theta \to -\theta$, we obtain the previous result. Hence,

$$A_{-n}(-x) = A_n(x) = J_n(x),$$
$$A_{-n}(x) = J_n(-x) = (-1)^n J_n(x).$$ (B.15)

Finally, for all integrals,

$$A_n(x) = (-1)^n J_n(x).$$ (B.16)

Note that when J_n is real, Eq. (B.12) can be rewritten as follows:

$$J_n(x) = \frac{1}{2}\int_{-\pi}^{\pi}\cos(x\sin\theta - n\theta)d\theta . \tag{B.17}$$

Term of $e^{ix\sin(\theta)}$, this is a periodic function which can be expanded in a Fourier series as follows:

$$e^{iz\sin(\theta)} = \sum_{n=-\infty}^{\infty}J_n(x)e^{in\theta} = J_0(x) + \sum_{n-1}^{\infty}J_n(x)\left(e^{in\theta} + (-1)^n e^{-in\theta}\right). \tag{B.18}$$

The separation of imaginary and real parts results in

$$\cos(x\sin(\theta)) = J_0(x) + 2\sum_{k=1}^{\infty}J_{2k}(x)\cos(2k\theta), \tag{B.19}$$

$$\sin(x\sin(\theta)) = 2\sum_{k=1}^{\infty}J_{2k+1}(x)\sin((2k+1)\theta). \tag{B.20}$$

In this thesis, we select the 2nd-harmonic ($2\omega_m$) and 3rd-harmonic ($3\omega_m$)to reduce the effect of the amplitude modulation of the LD. We apply the reference signal of the 2nd-harmonic cosine wave ($2\omega_m$) and the reference signal of the 3rd-harmonic sine wave ($3\omega_m$) to the lock-in detection signal of the Z-axis and X-axis displacement signals. Figure B.3 and Table B.1 show Bessel functions of J_2 (2nd-harmonic ($2\omega_m$)) and J_3(3rd-harmonic ($3\omega_m$)) and the relationship between the selected modulation depth (k_m), and the amplitudes of J_2 and J_3, respectively.
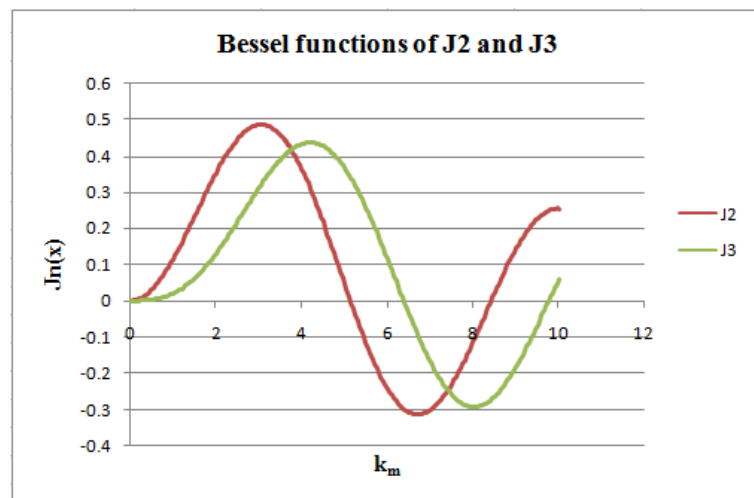
Fig. B.3 Bessel functions of J_2 and J_3

Table B.1 Relationship between the selected modulation depth (k_m) and the amplitudes of J_2 and J_3

km	J2	J3	J3/J2
0	0	0	0
3.7	0.42832966	0.4092251	0.95539754
3.71	0.42653996	0.41018202	0.96164968
3.72	0.42472487	0.41112218	0.96797296
3.73	0.42288449	0.41204547	0.97436884
3.74	0.42101895	0.41295176	0.98083888
3.75	0.41912837	0.41384092	0.98738463
3.76	0.41721288	0.41471283	0.99400774
3.77	0.41527259	0.41556738	1.00070985
3.78	0.41330765	0.41640444	1.00749269
3.79	0.41131817	0.41722389	1.01435803
3.8	0.4093043	0.41802563	1.02130769

From the concurrent measurement of spindle radial, axial, and angular motion using the three optical sensors and the phase modulation technique under the conditions shown in Table 5.10 (chapter 5), we selected the modulation depth ($k_{m,0}$ and $k_{m,\pm 2}$) of 3.76 rad, and an amplitude ratio of J_3 and J_2 of 0.994, and applied them to synchronize the signal of the axial (Z-axis) and radial (X-axis) motion.

References

[1] R. Grejda, E. Marsh, and R. Vallance, "Techniques for calibrating spindles with nanometer error motion," *Precision Engineering*, **Vol. 29**, No. 1, (2005), pp. 113-123.

[2] J.C. Lee, W. Gao, Y. Shimizu, J. Hwang, J.S. Oh, and C.H. Park, "Spindle error motion measurement of a large precision roll lathe," *International Journal of Precision Engineering and Manufacturing*, **Vol. 13**, No. 6, (2012), pp. 861-867.

[3] H. Murakami, N. Kawagoishi, E. Kondo, and A. Kodama, "Optical technique to measure five-degree of freedom error motions for a high-speed microspindle," *International Journal of Precision Engineering and manufacturing*, **Vol. 11**, No. 6, (2010), pp. 845-850.

[4] J. Kim, D. Shin, D. Yun, and C. Han, "The analysis of radial/axial error motion on a precision rotation stage," *Proceedings of World Academy of Science, Engineering and Technology*, **Vol. 23**, (2007), pp. 173-177.

[5] D.L. Martin, A.N. Tabenkin, and F.G. Parsons, "Precision spindle and bearing error analysis," *International Journal of Machine Tools and Manufacture*, **Vol. 35**, No. 2, (1995), pp. 187-193.

[6] S. Noguchi and T. Kanada, "Development of measuring system for radial non-repetitive run-out (NRRO) and perception about present state of angular contact ball bearing for machine tools," *Tribology International*, **Vol. 41**, No. 12, (2008), pp. 1176-1180.

[7] M.B. Bauza, S.C. Woody, S.T. Smith, and R.J. Hocken, "Development of a rapid profilometer with an application to roundness gauging," *Precision Engineering*, **Vol. 30**, No. 4, (2006), pp. 406-413.

[8] X. Lu and A. Jamalian, "A new method for characterizing axis of rotation radial error motion: Part 1: Two-dimensional radial error motion theory," *Precision Engineering*, **Vol. 35**, No. 1, (2011), pp. 73-94.

[9] S. Noguchi and K. Miyaguchi, "An evaluation method of radial accuracy for hydrostatic air spindles considering radial movement of the rotating center," *Precision Engineering*, **Vol. 27**, No. 4, (2003), pp. 395-400.

[10] R. Donaldson, "A simple method for separating spindle error from test ball roundness error," *Annals of the CIRP*, **Vol. 21**, (1972), pp. 125-126.

[11] C.J. Evans, R.J. Hocken, and W.T. Estler, "Self-calibration: reversal, redundancy, error separation and absolute testing," *CIRP Annals-Manufacturing Technology*, **Vol. 45**, No. 2, (1996) pp. 617-634.

[12] E.R. Marsh, Precision Spindle Metrology, *DEStech Publications*, Pennsylvania, (2008), pp. 1-13.

[13] D.G. Chetwynd and G.J. Siddall, "Improving the accuracy of roundness measurement," *Journal of Physics E: Scientific Instruments*, **Vol. 9**, No. 7, (1976), pp. 537-544.

[14] R. Thalmann and J. Spiller, "A primary roundness measuring machine," *Recent Developments in Traceable Dimensional Measurements III, Proceedings of SPIE*, **Vol. 5879**, (2005), pp. 1-10.

[15] S. Piengbangyang, T. Somthong, J. Buajarern, and A. Tonmueanwai, "Roundness measurement capability and traceability at NIMT," *Fundamental and Applied Metrology, Proceedings IMEKO*, (2009), pp. 1780-1783.

[16] D.J. Whitehouse, "Some theoretical aspects for error separation techniques in surface metrology," *Journal of Physics E: Scientific Instruments*, **Vol. 9**, No. 7, (1976), pp.531-536.

[17] W. Gao, S. Kiyono, and T. Nomura, "A new multiprobe method of roundness measurements," *Precision Engineering*, **Vol. 19**, No. 1, (1996), pp. 37-45.

[18] G.X. Zhang, Y.H. Zhang ,S.M. Yang, and Z. Li, "A multipoint method for spindle error motion measurement," *Annals of CIRP Manufacturing Technology*, **Vol. 46**, No. 1, (1997), pp. 441-445.

[19] W.T. Estler, C.J. Evans, and L.Z. Shao, "Uncertainty Estimation for Multiposition Form Error Metrology," *Precision Engineering*, **Vol. 21**, No. 2-3, (1997), pp.72-82.

[20] J.G. Salsbury, "Implementation of the Estler face motion reversal technique," *Precision Engineering*, **Vol. 27**, No. 2, (2003), pp.189-194.

[21] ANSI/ASME B89.3.4M, "Axes of Rotation, Methods for Specifying and Testing," *American Society of Mechanical Engineers*, (1985).

[22] ASME B89.3.4, "Axes of Rotation, Methods for Specifying and Testing," *American Society of Mechanical Engineers*, (2010).

[23] ISO 230-7, "Test code for machine tools-part 7: Geometric accuracy of axes of rotation," *International Standard organization*, (2006).

[24] J. Bryan, R. Clouser, and E. Holland, "Spindle Accuracy," *American Machinist*, **Vol. 111**, No. 25, (1967), pp. 149-164.

[25] H.F.F. Castro and M. Burdekin, "Calibration system based on a laser interferometer for kinematic accuracy assessment on machine tools," *International Journal of Machine Tools and Manufacture*, **Vol. 46**, No. 2, (2006), pp. 89-97.

[26] H.F.F. Castro, "A method for evaluating spindle rotation errors of machine tools using a laser interferometer," *Measurement*, **Vol.41**, No. 5, (2008), pp. 526-537.

[27] S. Noguchi, T. Tsukada, and A. Sakamoto, "Evaluation method to determine radial accuracy of high-precision rotating spindle units," *Precision Engineering*, **Vol.17**, No. 4, (1995), pp. 266-273.

[28] N. Srinivasa, J.C. Ziegert, and C.D. Mize, "Spindle thermal drift measurement using the laser ball bar," *Precision Engineering*, **Vol.18**, No. 2-3, (1996), pp. 118-128.

[29] S.H.H. Zargarbashi and J.R.R. Mayer, "Assessment of machine tool trunnion axis motion error, using magnetic double ball bar," *International Journal of Machine Tools and Manufacture*, **Vol. 46**, No. 14, (2006), pp.1823-1834.

[30] D. Kono, A. Matsubara, I. Yamaji, and T. Fujita, "High-precision machining by measurement and compensation of motion error," *International Journal of Machine Tools & Manufacture*, **Vol.48**, No. 10, (2008), pp. 1103-1110.

[31] H. Qiu, Y. Li, and Y. Li, "A new method and device for motion accuracy measurement of NC machine tools. Part 2: device error identification and trajectory measurement of general planar motions," *International Journal of Machine Tools and Manufacture*, **Vol. 41**, No. 4, (2001), pp. 535-554.

[32] H.L. Liu, H.M. Shi, B. Li and X. Li, "A new method and instrument for measuring circular motion error of NC machine tools," *International Journal of Machine Tools and Manufacture*, **Vol. 45**, No. 11, (2005), pp.1347-1351.

[33] S.H. Suh, E.S. Lee, and S.Y. Jung, "Error Modeling and Measurement for the Rotary Table of Five-axis Machine Tools," *International Journal of Advanced Manufacturing Technology*, **Vol.14**, No. 9, (1998), pp. 656-663.

[34] E.R. Marsh, J. Couey, and R. Vallance, "Roundness measurement of spherical artifacts at arbitrary latitude," *Precision Engineering*, **Vol. 30**, (2006), pp. 353-356.

[35] E.R. Marsh, J. Couey, and R. Valance, "Nanometer-level comparison of three spindle error motion separation techniques," *Journal of Manufacturing Science and Engineering*, **Vol.128**, No. 1, (2006), pp. 180-187.

[36] E. Okuyama, N. Nosaka, and J. Aoki, "Radial motion measurement of high-revolution spindle motor," *Measurement*, **Vol. 40**, No. 1, (2007), pp. 64-74.

[37] X. Huang, J. Lee, N. Ramakrishnan, M. Bedillion, and P. Chu, "Nano-positioning of and electromagnetic scanner with a MEMS capacitive sensor," *Mechatronics*, **Vol. 27**, No. 1, (2010), pp. 27-34.

[38] W.Y. Jywe, Y.R. Jeng, C.H. Liu, Y.F. Teng, C.H. Wu, H.S. Wang, and Y.J. Chen, "A novel 5 DOF thin coplanar nanometer-scale stage," *Precision Engineering*, **Vol. 32**, No. 4, (2008), pp. 239-250.

[39] P. Chapman, "A capacitance based ultra-precision spindle error analyzer," *Precision Engineering*, **Vol. 7**, No. 3, (1985), pp. 129-137.

[40] R.R. Vallance, E.R. Marsh, and P.T. Smith, "Effects of spherical targets on capacitive displacement measurements," *Journal of Manufacturing Science and Engineering*, **Vol.126**, No. 4, (2004), pp. 822-829.

[41] H.K. Chang, J.H. Kim, H. Kim., D. Y. Jang, and D.C. Han, "In-process surface roughness prediction using displacement signals from spindle motion," *International Journal of Machine Tools and Manufacture*, **Vol. 47**, No. 6, (2007), pp. 1021-1026.

[42] K.F. Hiia, R.R. Vallance, R. D. Grejda, and E.R. Marsh, "Error motion of a kinematic spindle," *Precision Engineering*, **Vol.28**, No. 2, (2004), pp. 204-217.

[43] D. Scheibner, J. Mehner, B. Bramer, T. Gessner, and W. Dotzel, "Wide range tunable resonators for vibration measurements," *Microelectronic Engineering*, **Vol. 67-68**, No. 1, (2003), pp. 542-549.

[44] C.P. Lawson and P.C. Ivey, "Turbomachinery blade vibration amplitude measurement through tip timing with capacitance tip clearance probes," *Sensors and Actuators A: Physical*, **Vol. 118**, No. 1, (2005), pp. 14-24.

[45] F.N. Toth and G.C.M. Meijer, "A low-cost, smart capacitive position sensor," *IEEE Transactions on Instrumentation and Measurement*, **Vol. 41**, No. 6, (1992), pp. 1041-1044.

[46] J.G. Kim, T.J. Lee, N.C. Park, Y.P. Park, K.S. Park, S.C. Lim, and W.S. Ohm, "Saw-based capacitive sensor with hemispherical electrode for nano-precision gap measurement," *Sensors and Actuators A: Physical*, **Vol. 163**, No. 1, (2010), pp. 54-60.

[47] e.g., Japan ADE Ltd.: MicroSense Series 5000.

[48] A. Sacconi, G.B. Picotto, and W. Pasin, "The IMGC calibration setup for micro-displacement actuators," *IEEE Transactions on Instrumentation and Measurement*, **Vol. 48**, No. 2, (1999), pp. 483-487.

[49] H. Haitjema, P. Schellekens, and S. Wetzels, "Calibration of displacement sensor up to 300 μm with nanometer accuracy and direct traceability to a primary standard of length," *Metrologia*, **Vol. 37**, No. 1, (2000), pp. 25-33.

[50] P.T. Smith, R.R. Vallance, and E.R. Marsh, "Correcting capacitive displacement measurements in metrology applications with cylindrical artifacts," *Precision Engineering*, **Vol. 29**, No. 3, (2005), pp. 324-335.

[51] M. Kim and W. Moon, "A new linear encoder-like capacitive displacement sensor," *Measurement*, **Vol. 39**, No. 6, (2006), pp. 481-489.

[52] M. Kim, W. Moon, E. Yoon, and K.R. Lee, "A new capacitive displacement sensor with high accuracy and long-range," *Sensors and Actuators A: Physical*, **Vol. 130-131**, (2006), pp. 135–141.

[53] J.B. Tan and J.N. Cui, "Ultra-precision 3D probing system based on spherical capacitive plate," *Sensors and Actuators A: Physical*, **Vol. 159**, No. 1, (2010), pp. 1-6.

[54] D. Crescini, A. Flammini, D. Marioli, and A. Taroni, "Application of an FFT-based algorithm to signal processing of LVDT position sensors," *IEEE Transactions on Instrumentation and Measurement*, **Vol. 47**, No. 5, (1998), pp. 1119–1123.

[55] H. Tariq, A. Takamori, F. Vetrano, C. Wang, A. Bertolini, G. Calamai, R. Salvo, A. Gennai, L. Holloway, G. Losurdo, S. Marka, M. Mazzoni, F. Paoletti, D. Passuello, V. Sannibale, and R. Stanga, "The linear variable differential transformer (LVDT) position sensor for gravitational wave interferometer low-frequency controls," *Nuclear Instruments and Methods in Physics Research A*, **Vol. 489**, No. 1-3, (2002), pp. 570-576.

[56] S.T. Wu, S.H. Mo, and B.S. Wu, "An LVDT-based self-actuating displacement transducer," *Sensors and Actuators A: Physical*, **Vol. 141**, No. 2, (2008), pp. 558-564.

[57] R. Thalmann, "A primary roundness measuring machine," *Proceedings of SPIE*: Recent Development in Traceable Dimensional measurment III, Washington, USA, **Vol. 5879**, (2005), pp. 1-10.

[58] T.G. Bifano and T.A. Dow, "Optical real time control of spindle runout," *Optical Engineering*, **Vol. 24**, No. 5, (1985), pp. 888–892.

[59] e.g., Taylor Hobson Ltd.: Talyrond 595 Range.

[60] e.g., Keyence Corporation.: Contact distance sensor/LVDT GT2 series.

[61] e.g., Agilent Technologies.

[62] e.g. Zygo Corp.

[63] e.g., Ranishaw.

[64] N. Bobroff, "Recent advances in displacement measuring interferometry," *Measurement Science and Technology*, **Vol. 4**, No. 9, (1993), pp. 907-926.

[65] T.Q. Banh, Y. Ohkubo, Y. Murai, and M. Aketagawa, "Active suppression of air refractive index fluctuation using Fabry-Perot cavity and piezoelectric volume actuator," *Applied Optics*, **Vol. 50**, No. 1, (2011), pp. 53-60.

[66] J.R. Lawall, "Fabry-Perot metrology for displacements up to 50 mm," *Journal of the Optical Society of America A*, **Vol. 22**, No. 12, (2005), pp. 2786-2798.

[67] J.Y. Lee and G.A. Jiang, "Displacement measurement using a wavelength-phase-shifting grating interferometer," *Optics Express*, **Vol. 21**, No. 21, (2013), pp. 25553-25564.

[68] C.C. Hsu, C.C. Wu, J.Y. Lee, H.Y. Chen, and H.F. Weng, "Reflection type heterodyne grating interferometry for in-plane displacement measurement," *Optics Communications*, **Vol. 281**, (2008), pp. 2582-2589.

[69] W. Gao and A. Kimura, "A three-axis displacement sensor with nanometric resolution," *Annals of the CIRP*, **Vol. 56**, No. 1, (2007), pp. 529-532.

[70] J.Y. Lee, H.Y. Chen, C.C. Hsu, and C.C. Wu, "Optical heterodyne grating interferometry for displacement measurement with sub-nanometric resolution," *Sensors and Actuators*, **Vol. 137**, No. 1, (2007), pp. 185-191.

[71] M. Ishige, F. Matsuura, M. Kawasugi, Y. Hoshino, T.Q. Banh, and M. Aketagawa, "Phase modulation homodyne displacement measuring interferometer using tunable laser diode as light source-1st Report:

Development of elementary techniques," *Journal of the Japan Society for Precision Engineering*, **Vol. 76**, No. 6, (2010), pp. 673-678.

[72] J. Ye, "Absolute measurement of a long arbitrary distance to less than an optical fringe," *Optics Letters*, **Vol. 29**, No. 10, (2004), pp. 1153-1155.

[73] S. Dejima, W. Gao, H. Shimizu, S. Kiyono, and Y. Tomita, "Precision positioning of a five degree-of-freedom planar motion stage," *Mechatronics*, **Vol.15**, No. 8, (2005), pp. 969-987.

[74] C.H. Liu, W.Y. Jywe, and S.C. Tzeng, "Simple three-dimensional laser angle sensor for three-dimensional small-angle measurement," *Applied Optics*, **Vol. 43**, No. 14, (2004), pp. 2840-2845.

[75] W. Jywe, C.J. Chen, W.H. Hsieh, P.D. Lin, H.H. Jwo, and T.Y. Yang, "A novel simple and low cost 4 degree of freedom angular indexing calibrating technique for a precision rotary table," *International Journal of Machine Tools & Manufacture*, **Vol.47**, No. 12-13, (2007), pp. 1978-1987.

[76] H. Qiu, Y. Yue, A. Kubo, C. Lin, K. Cheng, D. Huo, and D. Li, "Performance improvement of the LM device and its application to precise measurement of motion trajectories within a small range with a machining centre," *Journal of Modern Mechanical Engineering*, **Vol. 2**, No. 3, (2012), pp. 71-85.

[77] D. Kono, A. Matsubara, I. Yamaji, and T. Fujita, "High-precision machining by measurement and compensation of motion error," *International Journal of Machine Tools & Manufacture*, **Vol.48**, No. 10, (2008), pp. 1103-1110.

[78] T. Nomura, K. Kamiya, H. Miyashiro, S. Okuda, H. Tashiro, and K. Yoshikawa, "Shape measurements of mirror surfaces with a lateral shearing interferometer during machine running," *Precision Engineering*, **Vol. 22**, No. 4, (1998), pp. 185-189.

[79] A. Yamamoto and I. Yamaguchi, "Surface profilometry by wavelength scanning Fizeau interferometer," *Optics & Laser Technology*, **Vol. 32**, No. 4, (2000), pp. 261-266.

[80] G. Makosch and B. Drollinger, "Surface profile measurement with a scanning differential ac interferometer," *Applied Optics*, **Vol. 23**, No. 24, (1984), pp. 4544-4553.

[81] C. Xu, L. Chen, and J. Yin, "Method for absolute flatness measurement of optical surfaces," *Applied Optics*, **Vol. 48**, No. 13, (2009), pp. 2536-2541.

[82] A. Titov, I. Malinovsky, H. Belaidi, R.S. Franca, and C.A. Massone, "Precise interferometric length and phase-change measurement of gauge blocks based on reproducible wringing," *Applied Optics*, **Vol. 39**, No. 4, (2000), pp. 526-538.

[83] N. Ozawa, Y. Kitamura, T. Khono, K. Mitsui, and Y. Okazaki, "A new measurement method for spindle error motion using a cube-corner prism and laser interferometers (Principle of the method and preliminary experiment)," *Journal of the Japan Society for Precision Engineering*, **Vol. 56**, No. 2, (1990), pp. 381-387.

[84] W. Gao, T. Takahara, and S. Kiyono, "On machine measurement of angular motion of spindle," *Proceedings of ASPE Annual Meeting*, St. Louis, (1998), p. 355.

[85] I. Ogura and Y. Okazaki, "Precision measurement for axial and angular motion errors of turning spindle by using multi point method," *Journal of the Japan Society for Precision Engineering,* **Vol. 67**, (2001), pp. 1120-1124 (in Japanese).

[86] K.Y. Huang and C.H. Yeh, "Optical measurement system for error motions of small shaft," *Optical Engineering*, **Vol. 47**, No. 5, (2008), pp. 053601.

[87] J. Hartley, D. Berkley, and D. Franklin, "An ultrasonic technique for measuring the vibrational displacement of ultrasonic transducers," *Ultrasonic Imaging*, **Vol. 5**, (1983), p. 193.

[88] Y. Zhao, X. Li, L. Lin, and M.K. Lei, "Measurement of coating density using ultrasonic reflection coefficient phase spectrum," *Ultrasonics*, **Vol. 51**, No. 5, (2011), pp. 596-601.

[89] S. Zhao, S. Mojrzisch, and J. Wallaschek, "An ultrasonic levitation journal bearing able to control spindle center position," *Mechanical Systems and Signal Processing*, **Vol. 36**, (2013), pp. 168-181.

[90] S. Makinouchi, A. Watanabe, M. Takasaki, T. Ohara, and J.H. Ong, "An evaluation of a modulated laser encoder," *Precision Engineering*, **Vol. 35**, (2011), pp. 302-308.

[91] C.C. Wu, C.C. Hsu, J.Y Lee, H.Y. Chen, and C.L. Dai, "Optical heterodyne laser encoder with sub-nanometer resolution," *Measurement Science and Technology*, **Vol. 19**, No. 4, (2008), pp. 045305.

[92] A. Kimura, Y. Arai, and W. Gao, "A two-degree-of-freedom linear encoder for measurement of position and straightness," *Proceedings of the 23rd Annual Meeting of ASPE and the 12th ICPE, Portland*, USA, (2008), pp. 550-553.

[93] e.g., Heidenhain K.K: LIP 3x2 Series.

[94] e.g., Renishaw, FASTRACK incremental encoder.

[95] e.g., Mitutoyo, Absolute Linear Scale AT332.

[96] S. Kimoto, M. Nomura, T. Shibata, Y. Murakami, O. Horiuchi, and M. Masuda, "A prototype of axial encoder," *Proceedings of JSPE Annual Meeting 2008 Spring*, Tokyo, Japan, (2008), pp. 583-584 (in Japanese).

[97] M. Nomura, T. Kawashima, T. Shibata, Y. Murakami, M. Masuda, and O. Horiuchi, "Development of axis encoder to measure spindle axial motion," *International Journal of Automation Technology*, **Vol. 3**, No. 3, (2009), pp. 286-288.

[98] e.g., Keyence corporation: FS-V20.

[99] R. Schmitt, N. Konig, G. F. Mallmann, and F. Depiereux "Measurement of roundness and run-out with distributed fiber-optic sensors," *Proceedings of IMEKO*: Fundameantal and Applied Metrology, Lisbon, Portugal, (2009), pp. 69-73.

[100] K. Fujimaki and K. Mitsui, "Radial error measuring device based on auto-collimation for miniature ultra-high-speed spindle," *International Journal of Machine Tools and Manufacture*, **Vol.47**, No. 11, (2007), pp. 1667-1685.

[101] Y.C. Park and S.W. Kim, "Optical measurement of spindle radial motion by Moiré technique of concentric gratings," *International Journal of Machine Tools and Manufacture*, **Vol. 34**, No. 7, (1994), pp. 1019-1030.

[102] C.H. Liu, W.Y. Jywe, S.C. Tzeng, and Y.S. Lin, "Development of a novel optical measurement system for the error verification of a rotating spindle," *Optical Engineering*, **Vol. 44**, No. 9, (2005), pp. 097003.

[103] P. Chaikool, M. Aketagawa, and E. Okuyama, "Direct measurement of spindle radial motion error using a regular crystalline lattice and a scanning tunneling microscope," *International Journal of Precision Engineering and Manufacturing*, **Vol. 9**, No. 4, (2008), pp. 11-15.

[104] W. Gao, S. Kiyono, and E. Satoh, "Precision measurement of multi-degree of freedom spindle errors using two-dimensional slope sensors," *Annals of CIRP Manufacturing Technology*, **Vol. 51**, No. 4, (2002), pp. 447-450.

[105] E.R. Marsh and R. Grejda, "Experiences with the master axis method for measuring spindle error motions," *Precision Engineering*, **Vol.24**, No. 1, (2000), pp. 50-57.

[106] M. Madden, M. Aketagawa, Y. Ohkubo, S. Kimura, H. Maruyama, S. Higuchi, and E. Okuyama, "Proposal of concurrent measurement method for spindle radial, axial and angular motions using concentric grating interferometers," *International Journal of Surface Science and Engineering*, **Vol. 3**, No. 3, (2009), pp. 242-252.

[107] e.g., FANUC, ROBONANO.

[108] e.g., Zygo, flatness interferometer.

[109] P. Gregorcic, T. Pozar, and J. Mozina, "Quadrature phase-shift error analysis using a homodyne laser interferometer," *Optics Express*, **Vol.17**, No. 18, (2009), pp. 16322-16331.

[110] T. Keem, S. Gonda, I. Misumi, Q. Huang, and T. Kurosawa, "Removing nonlinearity of a homodyne interferometer by adjusting the gains of its quadrature detector system," *Applied Optics*, **Vol. 43**, No. 12, (2004), pp. 2443-2448.

[111] V. Greco, G. Molesini and F. Quercioli, "Accurate polarization interferometer," *Review of Scientific Instruments*, **Vol.66**, No. 7, (1995), pp. 3729-3734.

[112] G.H. Spencer and M. Murty, "General ray-tracing procedure," *Journal of the Optical Society of America*, **Vol. 52**, (1962), pp. 672.

[113] M. Madden, M. Aketagawa, S. Uesugi, T. Kumagai, and E. Okuyama, "Spindle error motion measurement using concentric circle grating and phase modulation interferometers," *International Journal of Automation Technology*, **Vol. 7**, No. 5, (2013), pp. 506-513.

[114] T. Hatsuzawa, Y. Tanimura, K. Toyoda, M. Nara, S. Toyonaga, S. Hara, H. Iwasaki, and K. Kondou, "A compact laser interferometer with a piezodriven scanner for metrological measurement in regular SEMs," *Review of Scientific Instruments*, **Vol. 65**, No. 8, (1994), pp. 2510-2513.

[115] e.g., SONY Manufacturing System, BD96 series.

[116] e.g., MicroE Systems**,** SP4800.

[117] O. Sasaki and H. Okasaki, "Sinusoidal phase modulating interferometry for surface profile measurement," *Applied Optics*, **Vol. 25**, No. 18, (1986), pp. 3137-3140.

[118] A. Dandridge, A.B. Tveten, and T.G. Giallorenzi, "Homodyne demodulation scheme for fiber optic sensors using phase generated carrier," *IEEE Journal of Quantum Electronics*, **Vol. 18**, No. 10, (1982), pp. 1647-1653.

[119] G. Basile, A. Bergamin, G. Cavagnero, and G. Mana, "Phase modulation in high-resolution optical interferometry," *Metrologia*, **Vol. 28**, (1991), pp. 455-461.

[120] e.g., Chuo Precision Industrial Co., Ltd.: ARS-636-HM.

[121] e.g., National Instrument**s,** M Series multifunction Data Acquisition (DAQ).

[122] M. Madden, M. Aketagawa, T. Kumagai, Y. Maeda, and E. Okuyama, "Concurrent measurement method for spindle radial, axial and angular motions using concentric circle grating and phase modulation interferometers," *Measurement Science and Technology*, **Vol. 25**, No. 9, (2014), 094005.

List of Papers

Published paper

1. **<u>Muhummad Madden</u>**, Masato Aketagawa, Yuria Ohkubo, Shohei Kimura, Hideki Maruyama, Satoru Higuchi, and Eiki Okuyama, 'Proposal of concurrent measurement method for spindle radial, axial and angular motions using concentric grating interferometers', *International Journal of Surface Science and Engineering*, (2009), Vol. 3, No. 3, pp.242-252.

2. **<u>Muhummad Madden</u>**, Masato Aketagawa, Shuhei Uesugi, Takuya Kumagai, and Eiki Okuyama, 'Spindle error motion measurement using concentric circle grating and phase modulation interferometers', *International Journal of Automation Technology*, (2013), Vol. 7, No. 5, pp.506-513.

3. **<u>Muhummad Madden</u>**, Masato Aketagawa, Takuya Kumagai, Yoshitaka Maeda, and Eiki Okuyama, 'Concurrent measurement method of spindle radial, axial and angular motions using concentric circle grating and phase modulation interferometers', *Measurement Science and Technology*, (2014), Vol. 25, No. 9, 094005.

Papers for the international conferences
(With referees)

1. **<u>Muhummad Madden</u>**, Yuria Ohkubo, Shohei Kimura, Eiki Okuyama, and Masato Aketagawa, 'Concurrent measurement method of spindle radial, axial and angular motions using concentric grating interferometers', *Proceedings of the 3rd International Conference on Positioning Technology (ICPT)*, (2008), Hamamatsu, Japan, PME6, pp.211-212.

2. **<u>Muhummad Madden</u>**, Masato Aketagawa, Jaratsri Soeatuptim, and Eiki Okuyama, 'Concurrent measurement of spindle radial, axial and angular motions using concentric grating interferometers', *Proceedings of the 10th International Symposium of Measurement Technology and Intelligent Instrument (ISMTII)*, (2011), Daejeon, Korea, D2-1, pp.132.

3. Masato Aketagawa, **Muhummad Madden**, Shuhei Uesugi, Takuya Kumagai, Yoshitaka Maeda, and Eiki Okuyama, 'Spindle error motion measurement using concentric circle grating and phase modulation interferometers', *Proceedings of the Society of Photographic Instrumentation Engineers (SPIE): Optical Metrology and Inspection for Industrial Applications II*, (2012), Vol. 8563, Beijing, China, pp. 1-10.

4. Masato Aketagawa, **Muhummad Madden**, Shuhei Uesugi, Takuya Kumagai, Yoshitaka Maeda, and Eiki Okuyama, 'Spindle error motion measurement using concentric circle grating and phase modulation interferometers', *Proceedings of the 5th International Conference on Positioning Technology (ICPT)*, (2012), Kaohsiung, Taiwan, SE-8, pp.211-212.

5. **Muhummad Madden**, Masato Aketagawa, Takuya Kumagai, Yoshitaka Maeda, and Eiki Okuyama, 'Concurrent measurement method of spindle radial, axial and angular motions using concentric circle grating and phase modulation interferometers', *Proceedings of the 5th International Conference of Asian Society for Precision Engineering and Nanotechnology (ASPEN)*, (2013), Taipei, Taiwan, 1083, pp.65.

(Without referees)

1. **Muhummad Madden**, Masato Aketagawa, Jaratsri Soeatuptim, and Eiki Okuyama, 'Concurrent measurement of spindle radial, axial and angular motions using concentric grating interferometers', *Proceedings of the 1st International Gigaku Conference in Nagaoka (IGCN)*, (2012), Nagaoka, Japan, MP-26.

2. **Muhummad Madden**, Masato Aketagawa, Takuya Kumagai, Yoshitaka Maeda, and Eiki Okuyama, 'Spindle error motion measurement using concentric circle grating and phase modulation interferometers', *Proceedings of the 2nd International Gigaku Conference in Nagaoka (IGCN)*, (2013), Nagaoka, Japan, IP-7, pp.18.

3. **Muhummad Madden**, Masato Aketagawa, Takuya Kumagai, Yoshitaka Maeda, and Eiki Okuyama, 'Spindle error motion measurement using concentric circle grating and phase modulation interferometers', *Proceedings of the 3rd International Symposium on Engineering, Energy and Environment (ISEEE)*, (2013), Bangkok, Thailand, MAD02, pp.78.

Papers for the national conferences

1. 明田川正人• **Muhummad Madden** • 大久保ユリア• 木村書平・奥山栄樹, 同心円回折格子干渉計を用いた軸受のラジアル　アキシャル　アンギュラモーションの同時測定法 (第 1 報：測定原理と誤差分析), 2009 年度精密工学会春季大会学術講演会講演論文集, G19, pp.477-478.

2. **Muhummad Madden** • Jaratsri Soeatuptim • 明 田 川 正 人 , Concurrent measurement method of spindle radial, axial and angular motions using concentric grating interferometers, 2010 年度精密工学会北陸信越支部学術講演会講演論文集, B17, pp.69-70.

3. 明田川正人• **Muhummad Madden** • Jaratsri Soeatuptim • 奥山栄樹, 同心円回折格子干渉計を用いた軸受のラジアル　アキシャル　アンギュラモーションの同時測定法 (第 2 報：光学センサーの性能評価), 2011 年度精密工学会秋季大会学術講演会講演論文集, N32, pp.872-873.

4. Jaratsri Soeatuptim • **Muhummad Madden** • 明 田 川 正 人 , Concurrent measurement method of spindle radial, axial and angular motions using concentric grating interferometers (3rd report: Measurements of 5 degree of freedom error motions), 2012 年度精密工学会春季大会学術講演論文集, F09, pp.433-434.

5. 上杉修平・**Muhummad Madden**・熊谷卓也・前田能孝・明田川正人, 同心円回折格子干渉計を用いた軸受のラジアル　アキシャル　アンギュラモーションの一括測定(第 4 報：周波数変調によるリサージュダイアグラムの取得), 2012 年度精密工学会秋季大会学術講演会講演論文集, N03, pp.927-928.

6. 上杉修平・**Muhummad Madden**・熊谷卓也・明田川正人, 同心円回折格子干渉計を用いた軸受のラジアル　アキシャル　アンギュラモーションの一括測定(第 5 報：低速回転軸受の誤差測定), 2013 年度精密工学会春季大会学術講演会講演論文集, N33.

7. **Muhummad Madden**・上杉修平・熊谷卓也・明田川正人, マイケルソン干渉計と回折格子干渉計のための位相変調と補間法, 2013 年度精密工学会春季大会学術講演会講演論文集, N21, pp.917-918.

8. 熊谷卓也・**<u>Muhummad Madden</u>**・前田能孝・中谷勇貴・明田川正人, 同心円回折格子干渉計を用いた軸受のラジアル　アキシャル　アンギュラモーションの一括測定(第 6 報：小型高剛性干渉計の製作), 2013 年度精密工学会秋季大会学術講演会講演論文集, B23, pp.81-82.

9. 熊谷卓也・**<u>Muhummad Madden</u>**・前田能孝・明田川正人, 同心円回折格子干渉計を用いた軸受のラジアル　アキシャル　アンギュラモーションの一括測定(第 7 報：小型高剛性干渉計の製作), 2014 年度精密工学会春季大会学術講演会講演論文集, A36.

Proposal of concurrent measurement method for spindle radial, axial and angular motions using concentric grating interferometers

Muhummad Madden, Masato Aketagawa*, Yuria Ohkubo and Shohei Kimura

Department of Mechanical Engineering,
Nagaoka University of Technology,
1603-1 Kamitomioka-cho, Nagaoka, Niigata 940-2188, Japan
Fax: +81-258-47-9771
E-mail: madden@stn.nagaokaut.ac.jp
E-mail: masatoaa@vos.nagaokaut.ac.jp
E-mail: okhkubo@stn.nagaokaut.ac.jp
E-mail: kimura@stn.nagaokaut.ac.jp
*Corresponding author

Hideki Maruyama and Satoru Higuchi

Industrial Research Institute of Niigata Prefecture,
1-11-1 Abuminishi, Chuo-Ku, Niigata 950-0915, Japan
Fax: +81-258-47-5172
E-mail: hmaru@iri.pref.niigata.jp
E-mail: shiguchi@iri.pref.niigata.jp

Eiki Okuyama

Department of Mechanical Engineering,
Akita University,
1-1 Tegatagakuenmachi, Akita 010-8502, Japan
Fax: +81-188-37-0405
E-mail: okuyama@ipc.akita-u.ac.jp

Abstract: In this paper, we propose a measurement method for spindle radial, axial and angular motions using concentric circle grating interferometers. In this method, the grating is installed on top of the spindle. Three optical sensors, which consist of two interferometers, are fixed over the grating. One interferometer detects an interference signal between reflection lights from a fixed mirror and the grating for vertical displacement measurement. The other interferometer detects an interference signal between ±first diffraction lights from the grating for lateral displacement measurement. Using three optical sensors, radial, axial and angular motions of the spindle, can be measured concurrently.

Keywords: spindle; radial motion; axial motion; angular motion; grating; interferometer; nanometre.

Biographical notes: Muhummad Madden received his Bachelor of Science in Physics from King Mongkut's University of Technology Thonburi, Thailand, in 2001. He acted as a Metrologist in Surface Texture and Roundness Laboratory, National Institute of Metrology, Thailand, in 2002. He is currently Master's Degree student at Nagaoka University of Technology. He is a student member of the JSPE.

Masato Aketagawa received his MS in Applied Physics from Tokyo Institute of Technology, Japan, in 1985. He worked in Canon Inc., Japan, from 1985 to 1990. He joined Mechanical Engineering Department in Nagaoka University of Technology, Japan, in 1991. He received Doctor of Engineering from Nagaoka University of Technology in 1998. He is currently Associate Professor in Nagaoka University of Technology. He acted as a Visiting Researcher at Mechanical Engineering Department of Birmingham University, UK, in 1995 and a visiting researcher at Precision Engineering Department of Physikalisch-Technischen Bundesanstalt, Germany, in 2003. His research interests include optical interferometer and nanometrology. He is a member of the JSPE, ASPE, JSAP and OSA.

Yuria Ohkubo received her Bachelor's Degree in Mechanical Engineering from Nagaoka University of Technology, Japan, in 2008. She is currently Master's Degree student at Nagaoka University of Technology. She is a student member of the JSME and JSPE.

Shohei Kimura received her Bachelor's Degree in Mechanical Engineering from Nagaoka University of Technology, Japan, in 2008. He is currently Master's Degree student at Nagaoka University of Technology. He is a student member of the JSPE.

Hideki Maruyama received his BS in Mechanical Engineering from Niigata University, Japan, in 1990. He joined Applied Materials Japan Inc., from 1990 to 1993. He joined Industrial Research Institute of Niigata Prefecture from 1993. He is currently senior researcher in Industrial Research Institute of Niigata Prefecture.

Satoru Higuchi received his BS in Mechanical Engineering from Niigata University, Japan, in 1998. He joined Industrial Research Institute of Niigata Prefecture in 1998. He is currently researcher in Industrial Research Institute of Niigata Prefecture.

Eiki Okuyama obtained his MS in Engineering from Tohoku University, Japan, in 1985. He worked at Akita National College of Technology from 1985 to 1991. He is now Associate Professor at Akita University, Japan. He obtained Doctoral Degree of Engineering from Tohoku University in 1995. He was a visiting fellow at School of Engineering, University of Warwick, UK, in 1995. His research interests are precision measurement, software datum and nanometrology. He is a member of the JSPE and JSME.

1   Introduction

Ideal spindles as basic mechanical components must have only one-dimensional rotary motion degree of freedom; therefore, extra five-dimensional motion degrees of freedom (= radial (2 degrees) + axial (1 degree) + angular (2 degrees)) are identified as motion errors, which must be eliminated or reduced. Since ultra-precision fabrication machines and information technology instruments, such as a hard disk, have progressed very rapidly, reductions in spindle rotating errors (radial, axial and angular motions) to nanometre and sub-μ radian levels in such industries are required. The industries have also intended to increase the rotation speed up to 100 krpm or more while keeping the nanometre and sub-μ radian precision.

Conventional spindle motion error measurements are error separation methods, which require artefact reference and displacement sensors, such as capacitive sensors. Radial motion error can be measured using a precise sphere or circular cylinder (Donaldson, 1972; Marsh et al., 2006; Okuyamaet al., 2007). A concentric circle grating is also used for measuring the radial motion error (Park and Kim, 1994; Kataoka et al., 2008). A precise circular cylinder with a precise end mirror surface can be used as the reference artefact for the concurrent measurement of (radial + axial) or (axial + angular) motions (Gao et al., 1998; Ogura and Okazaki, 2001). The concentric measurement of radial, axial and angular motions can be realised using the reference artefact of two spheres linked with a bar (Marsh, 2008). However, in the concurrent measurement of radial, axial and angular motions, the artefact is voluminous and has too much mass to have the possibility of inhibiting the original rotational motion of the spindle. Moreover, capacitive sensors have narrow bandwidths, and maintaining the traceability against the meter definition is difficult because of their drift characteristic. As similar examples for multi-axes displacement measurement, two-dimensional grating mirrors are used as fixed and moving mirrors in Michelson interferometers (Gao and Kimura, 2007; Kimura et al., 2008).

In this paper, we propose a novel method for the concurrent measurement of five degree motion errors (= radial, axial and angular motions) using a concentric circle grating and interferometers and discuss its application to ultra-precise and high-speed spindles. In this method, a concentric circle grating plate with a fine pitch is installed on top of the spindle of interest and is used as the reference artefact. Because the concentric circle grating plate is not voluminous and not heavy, this method is effective for any spindle, and does not affect the spindle original rotational motion. Since this method is based on wide-bandwidth photosensors, it is possible to apply it to high rotational speed spindles. Moreover, this method is suitable for maintaining the traceability against the meter definition because it uses laser interferometers. In this paper, we discuss the measurement principle and preliminary experiment.

2   Measurement principles

2.1   *Two-dimensional displacement measuring interferometer using one-dimensional grating*

Figure 1 shows a schematic diagram of the two-dimensional displacement measuring interferometer. In the figure, the *X-*, *Y-* and *Z*-axes indicate the grating pitch, the ruling

and height directions, respectively; therefore, the *XY* plane is parallel to the grating plane. The two-dimensional displacement measuring interferometer consists of *X*-axis and *Z*-axis displacement measuring interferometers, as shown in Figure 1.

Figure 1 Schematic diagram of two-dimensional displacement measuring interferometer
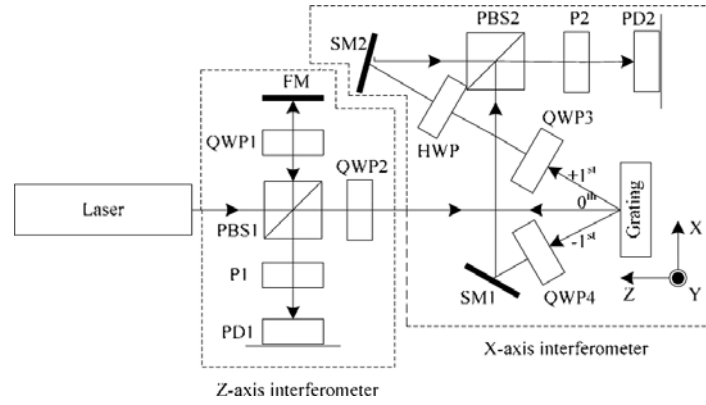
PBS: Polarised beam splitter; QWP: Quarter-wave plate; HWP: Half-wave plate;
FM: Fixed mirror; SM: Steering mirror; PD: Photodiode; P: Polariser.

A light beam emitted from the laser is incident on Polarised Beam Splitter 1 (PBS1), and then, it is divided into two beams. The first beam reflected from PBS1 enters the FM via Quarter-Wave Plate 1 (QWP1) and bounces from FM and reaches Photodiode 1 (PD1) via PBS1 and Polariser 1 (P1). The second beam, which goes through PBS1, reaches the one-dimensional grating via QWP2. In Figure 1, we assume that the incident angle θ_i of the second beam to the grating is almost null. Thus, the reflected light (= zeroth-order diffraction light) reaches PD1 via QWP2, PBS1 and P1. At PD1, it is possible to detect an interferometer fringe between the reflection lights from FM and the grating, and to measure the displacement along the *Z*-axis of the grating.

The incident light on the grating can produce ±first-order diffraction lights. The diffraction light direction is derived using the vector format from (Spencer and Murty, 1962)

$$s' \times \varepsilon - s \times \varepsilon = m \frac{\lambda}{nd} q, \tag{1}$$

where s, s', ε, q, m, d, n and λ represent a unit vector along the incident light direction, a unit vector along the diffraction light direction, a unit vector normal to the grating plane, a unit vector along the ruling direction, a diffraction order, a grating pitch, a refractive index and a vacuum wavelength, respectively. In the figure, the ε and q vectors are the same as the unit vectors along the *Z*- and *Y*-axes. If the incident angle on the *XZ* plane is $\theta_{iXZ} (\theta_{iXZ} \ll 1)$, the ±first-order diffraction angles θ_{+1} and θ_{-1} (on *XZ* plane) can be derived from

$$d(\sin\theta_{+1} - \sin\theta_{iXZ}) = +\lambda \tag{2}$$

$$d(\sin\theta_{-1} - \sin\theta_{iXZ}) = -\lambda. \tag{3}$$

In these equations, we assume $n = 1$.

In Figure 1, the interference fringe between ±first-order diffraction lights is formed on PD2 via QWP 3/4, Half-Wave Plate (HWP), Steering Mirror 1/2 (SM1/2), PBS2 and P2. We assume that Δx, Δy and Δz are the displacement shifts of the grating along the *X*-, *Y*- and *Z*-axes, respectively. We also assume that the small incident angle θ_{iYZ} ($\theta_{iYZ} \ll 1$) on the *YZ* plane and the small incident angle θ_{iz} ($\theta_{iZ} \ll 1$) between the incident light and the *Z*-axis affect the interference fringe. The phase shifts $\Delta\phi_{+1}$ and $\Delta\phi_{-1}$ of the ±first-order diffraction lights owing to the shifts (Δx, Δy, Δz) and the small incident angles of (θ_{iXZ}, θ_{iYZ}) are written as

$$\phi_{+1} = \frac{2\pi}{\lambda}\{\Delta x \sin\theta_{+1} - \Delta z \cos\theta_{+1} + \Delta x \sin 2\theta_{iYZ} - \Delta z \cos 2\theta_{iYZ}\}, \tag{4}$$

$$\phi_{-1} = \frac{2\pi}{\lambda}\{\Delta x \sin\theta_{-1} - \Delta z \cos\theta_{-1} + \Delta x \sin 2\theta_{iYZ} - \Delta z \cos 2\theta_{iYZ}\}. \tag{5}$$

From equations (4) and (5), the combined electrical field $E_{\pm1}$ on PD2 is represented as

$$E_{\pm1} = E_{+1}\exp i(\varphi_{+1} + \phi_{+1}) + E_{-1}\exp i(\varphi_{-1} + \phi_{-1}), \tag{6}$$

where E_{+1} and E_{-1} and φ_{+1} and φ_{-1} are the amplitudes and initial phases of ±first-order diffraction electrical fields, respectively.

From equations (2)–(6), the interference light intensity $I_{\pm1}(\Delta x, \Delta z)$ on PD2 is

$$I_{\pm1}(\Delta x, \Delta z) = E_{+1}^2 + E_{-1}^2 + 2E_{+1}E_{-1}\cos\{(\varphi_{+1} - \varphi_{-1})$$
$$+ \frac{2\pi}{\lambda}\Delta z(\cos\theta_{+1} - \cos\theta_{-1}) + \frac{4\pi}{d}\Delta x \tag{7}$$

The interference light intensity $I_{\mathrm{fix}0}(\Delta x, \Delta z)$ between the two lights reflected from FM and the grating can be written in the same manner as

$$I_{\mathrm{fix}0}(\Delta x, \Delta z) = E_{\mathrm{fix}}^2 + E_0^2 + 2E_{\mathrm{fix}}E_0\cos\left[\psi + \frac{4\pi}{\lambda}\left(\Delta z + \sqrt{\Delta x^2 + \Delta y^2}\tan 2\theta_{iZ}\right)\right.$$
$$\left. + L\left(1 - \sqrt{\tan^2 2\theta_{iYZ} + 1}\right)\right\} \tag{8}$$

where E_{fix}, E_0, ψ and L are the amplitudes of the lights reflected from FM, the grating, the initial phase and the *Z*-axis and the distance from the grating and PD1. The last two terms in cosine are from the incline wave front of the grating.

Equations (7) and (8) contain errors arising from the small incident angles θ_{iXZ} and θ_{iZ}. However, the contributions from θ_{iXZ} and θ_{iZ} can be neglected in the case of the ultra-precise spindle measurement. If $\lambda = 633$ nm, $d = 2$ μm, $\theta_{iXZ} < 10$ arcsec and $\Delta z < 1$ μm, then $(2\pi/\lambda)\Delta z(\cos\theta_{+1} - \cos\theta_{-1}) \leqq 10^{-4}$ order. This value is the same as $|\Delta x| \leqq 50$ pm; therefore, it can be neglected. For the condition of ($\lambda = 633$ nm, $\theta_{iZ} < 10$ arcsec, $\sqrt{\Delta x^2 + \Delta y^2} < 1$ μm and $L = 20$ mm), the contributions from $\sqrt{\Delta x^2 + \Delta y^2}\tan 2\theta_{iZ}$ and $L\left(1 - \sqrt{\tan^2 2\theta_{iYZ} + 1}\right)$ in equation (8) are 90 pm and 90 pm, respectively; therefore, they can also be neglected. In the ultra-precise spindle measurement, radial $\left(\sqrt{\Delta x^2 + \Delta y^2}\right)$, axial ($\Delta z$) and angular ($\theta_{iXZ}$ and θ_{iZ}) are less than 1 μm, 1 μm and 10 arcsec, respectively. Therefore, for the small radial, axial and angular motions, equations (7) and (8) are approximated as

$$I_{\pm 1} = E_{+1}^2 + E_{-1}^2 + 2E_{+1}E_{-1} \cos\left(\frac{4\pi}{d}\Delta x\right). \tag{9}$$

$$I_{\text{fix}0} = E_{\text{fix}}^2 + E_0^2 + 2E_{\text{fix}}E_0 \cos\left(\frac{4\pi}{\lambda}\Delta z\right). \tag{10}$$

To interpolate the unit periods of ($d/2$) and ($\lambda/2$) in equations (9) and (10), some optical techniques (Hatsuzawa et al., 1994) can be used in the method. An interpolation order of 8000 or more is available with some commercial products for homodyne interferometers (BD96 @ SONY Manufacturing System, SP4800 @ MicroE System). A heterodyne technique (Hsu et al., 2008) can also be applied to the proposed method. To reduce the distance L between the grating and PD1, the compact size optics can be applied.

2.2   Spindle motion error measurement

Figure 2 shows the measurement principle of the spindle motion error using the two-dimensional displacement measuring interferometers. A concentric circle grating is set on top of the spindle of interest. Three two-dimensional displacement measuring interferometers *A*, *B* and *C* are fixed over the concentric circle grating. The spindle rotation centre must be nearly aligned to the centre of the concentric grating within 1 μm or less. The grating plane must also be aligned to be parallel with the *XY* plane within 10 arcsec. In Figure 2, the centre is selected as the origin point of the *XYZ* coordinate system. The two-dimensional displacement measuring interferometer *A* is located along the *Y*-axis with the distance R_A from the centre and measures the *Y*-axis and *Z*-axis displacements y_A and z_A using the concentric circle grating, whereas the interferometers *B* and *C* are located along the *X*-axis with the distances R_B and R_C from the centre, and measure the *X*-axis and *Z*-axis displacements x_B, z_B, x_C and z_C using the concentric circle grating. From the measured displacements by the three interferometers, the radial R_x, R_y, axial R_z and angular θ_x, θ_y motions can be derived from

$$R_x = \frac{1}{2}(x_B + x_C), \tag{11}$$

$$R_y = y_A, \tag{12}$$

$$R_z = \frac{1}{3}(z_A + z_B + z_C), \tag{13}$$

$$\theta_x = \frac{1}{R}\left[z_A - \frac{(z_B + z_C)}{2}\right], \tag{14}$$

$$\theta_y = \frac{2}{R}(z_B - z_C), \tag{15}$$

$$R = \frac{1}{3}(R_A + R_B + R_C), \tag{16}$$

where *R* is the averaged distance of the interferometers *A*, *B* and *C* from the centre. In general, the grating must exhibit artefact errors (= roundness, flatness and irregular pitch); however, it is possible to apply the error separation methods (multistep, multipoint) to the concentric circle grating. Therefore, another arrangement of interferometers *A*, *B* and *C* is possible.

Figure 2   Measurement principle for radial, axial and angular motions using two-dimensional displacement measuring interferometer. *A*, *B* and *C* are two-dimensional displacement interferometers, *A*: *YZ* sensor, *B* and *C*: *XZ* sensor

Top view   Side view
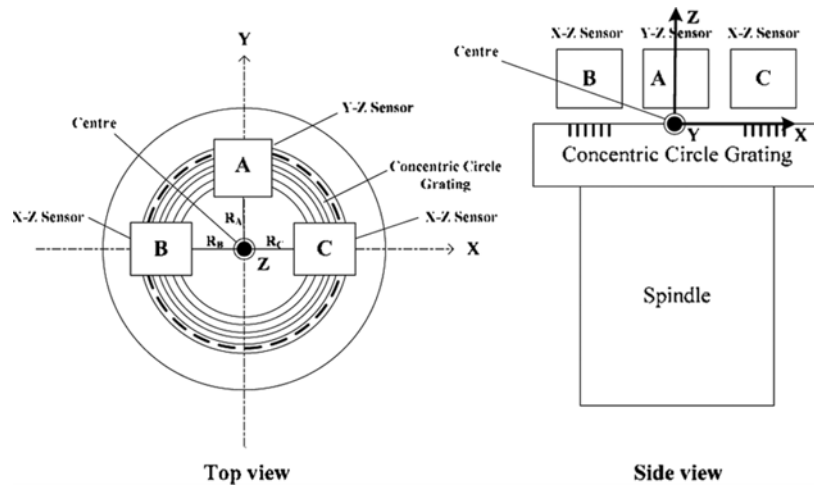
We would like to apply our method to ultra-precise spindles with a radial (or axial) motion of 1 μm or less, an angular motion of 5 μrad or less and a high rotational speed of 100 krpm or more. The target measurement specification is as follows.

(S1)   Radial motion (*X* and *Y* axes) resolution: 0.12 nm (2 μm pitch grating with 8000 interpolation order)

(S2)   Axial motion (*Z* axis) resolution: 0.04 nm (Wavelength of 633 nm with 8000 interpolation order)

(S3)   Angular motion resolution: 0.01 μrad (concentric circle grating radius (R) of 20 mm)

(S4)   Maximum measurable rotational speed: 100 krpm (360 points per one revolution and sampling rate of 600 kHz).

3   Preliminary experiment and discussion

3.1   *Performance evaluation of two-dimensional displacement measuring interferometer*

To confirm equations (9) and (10), we constructed a trial interferometer using a one-dimensional grating, as shown in Figure 3. In our experiment, the grating was set on the *XZ*-axes stage and moved with Piezoelectric (PZT) actuators along both

the *X*- and *Z*-axes. Instead of the concentric circle grating, a one-dimensional grating with 1200 lines/mm was utilised. A He–Ne laser ($\lambda = 633$ nm) was used as the light source. In our experiment, interference signals on PD1 and PD2 were compared with the driving signal of PZT actuators. Figures 4 and 5 show the obtained comparison results. Figure 4 shows the time variations of the *X*-axis driving signal and the interference fringe of ±first-order diffraction lights obtained when the *Z*-axis movement was stopped. Figure 5 shows the time variation of the *Z*-axis driving signal and the interference fringe of the reflected lights from FM and the grating obtained when the *X*-axis movement was stopped.

In Figure 4, the applied displacement amplitude to the *X*-axis stage is 1.3 µm, and the observed fringe period of the interference is about 4. This shows that the basic period is 0.4 µm, and *d*/2 is 417 nm. In Figure 5, the applied displacement amplitude to the *Z*-axis stage is 1.1 µm, the observed period of the interference signal is nearly 0.3 µm and λ/2 is 317 nm. The experiment results show that the proposed method enables the measurement of the *X*-axis and *Z*-axis displacements from the interference fringes.

Figure 3 Schematic photograph of experimental system (see online version for colours)
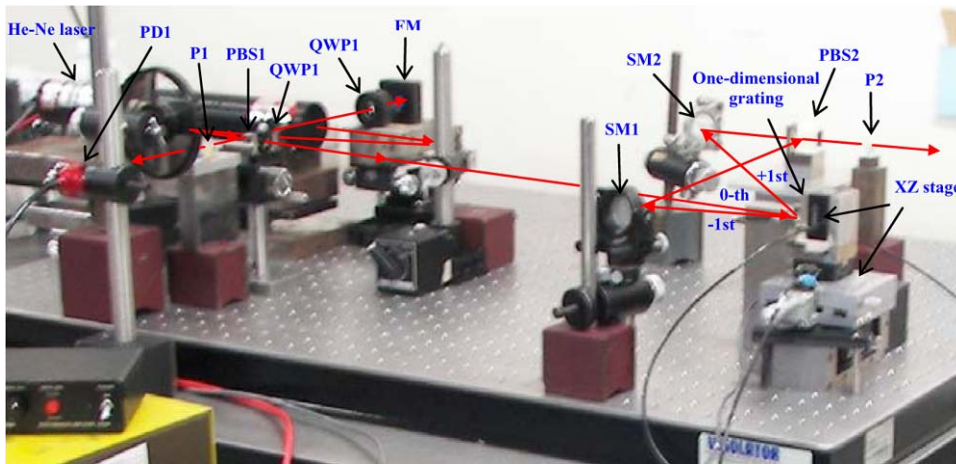
Figure 4 Relationship between *X*-axis displacement driving signal (upper) and interference signal from ±first-order diffraction (lower) (see online version for colours)
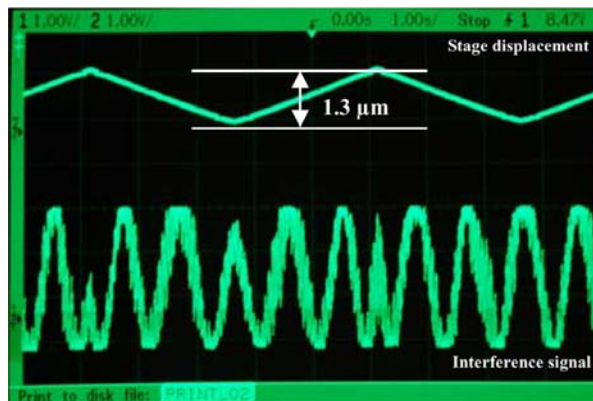
Figure 5   Relationship between *Z*-axis displacement driving signal (upper) and interference signal from zeroth-order diffraction (lower) (see online version for colours)
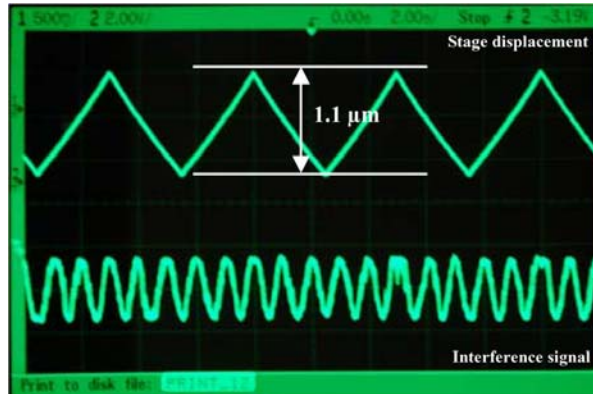
3.2   Trial fabrication of concentric circle grating

In the proposed method, the fine concentric circle grating is the key technology for attaining the measurement goal. To confirm this, we have fabricated a concentric circle grating with a pitch of 5 µm. Figure 6(a) and (b) show the outline photo and the design of the concentric circle grating, respectively. The grating was fabricated using an ultra-precise Numerical Control (NC) cutting machine tool (ROBONANO@FANUC) and a sharp single crystal diamond tool with a top radius of 1 µm. The material used was stainless steel with nickel phosphide plating of 100 µm thickness. Many grating grooves were formed on the nickel phosphide plate. In the grating, 1000 pitches were formed with a concentric circle structure. In Figure 6(b), the grooved grating shows good uniformity and a period of 5 µm. To determine the possibility of fabricating narrower gratings using the NC machine and diamond tool, we fabricated a 2-µm-pitch grating. Figure 7 shows its SEM image. We believe that it is possible to fabricate a concentric circle grating with a fine pitch of 1 µm or less using the NC machine and a diamond tool. If we can use optical (or electron beam) lithography, the grating pitch of 500 nm or less is possible to fabricate.

Figure 6   (a) Outline of concentric circle grating. 1000 concentric circle gratings with a pitch period of 5 µm were fabricated and (b) the concentric circle grating design (see online version for colours)

(a)   (b)
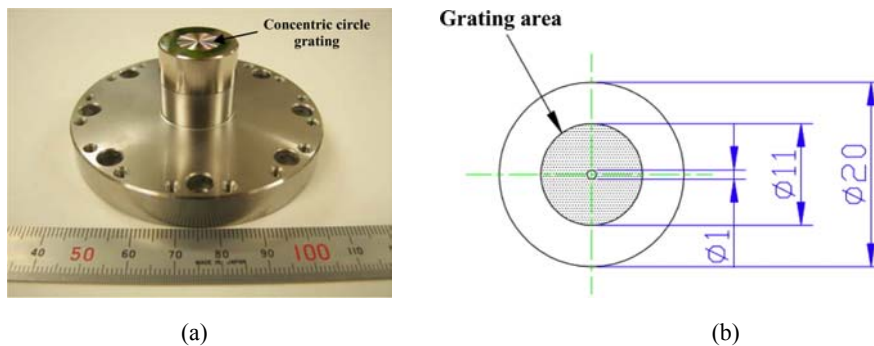
Figure 7 Scanning electron microscopy image of 2-μm-pitch-period grating
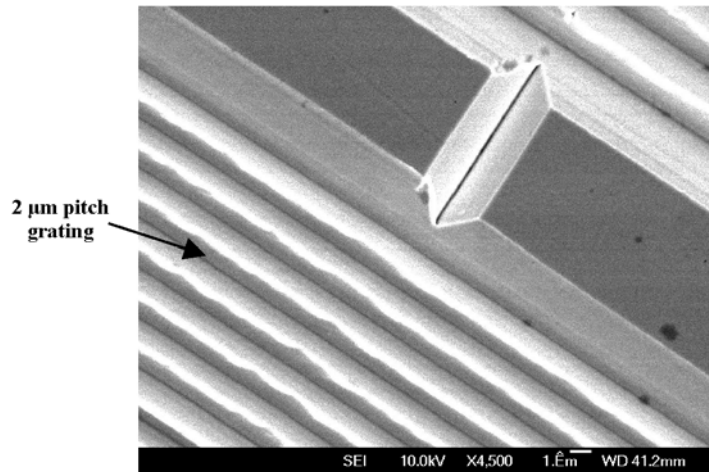
4 Conclusion and future study

In this paper, to measure the spindle radial, axial and angular motions simultaneously, we propose a novel method using a concentric circle grating and interferometers. The measurement principle of a two-dimensional displacement measuring interferometer using a one-dimensional grating is clarified. The error analysis of the interferometer is performed from the views of radial, axial and angular motion measurements. For a small motion error, the interferometer can be used to measure the lateral and vertical axes displacements with high speed.

The two-dimensional displacement measuring interferometer using a one-dimensional grating was constructed and examined. The vertical and lateral displacements were obtained from interference signals. The concentric circle grating with a period of 5 μm and 1000 pitches was fabricated using an ultra-precise NC machine tool and a diamond cutter. A 2-μm-pitch-grating was also fabricated. From the obtained results, we believe that it is possible to concurrently measure the spindle radial, axial and angular motions with high resolution and speed. In the near future, we plan to construct the entire system and report its performance characteristics.

References

Donaldson, R. (1972) 'A simple method for separating spindle error from test ball roundness error', *Annals of the CIRP*, Vol. 21, pp.125, 126.

Gao, W. and Kimura, A. (2007) 'A three-axis displacement sensor with nanometric resolution', *Annals of the CIRP*, Vol. 56, No. 1, pp.529–532.

Gao, W., Takahara, T. and Kiyono, S. (1998) 'On machine measurement of angular motion of spindle', *Proceeding of ASPE Annual Meeting*, St. Luis, p.355.

Hatsuzawa, T., Tanimura, Y., Toyoda, K., Nara, M., Toyonaga, S., Hara, S., Iwasaki, H. and Kondou, K. (1994) 'A compact laser interferometer with a piezodriven scanner for metrological measurement in regular SEMs', *Rev. Sci. Instum.*, Vol. 65, No. 8, pp.2510–2513.

Hsu, C.C., Wu, C.C., Lee, J.Y., Chen, H.Y. and Weng, H.F. (2008) 'Reflection type heterodyne grating interferometry for in-plane displacement measurement', *Optics Communications*, Vol. 281, pp.2582–2589.

Kataoka, A., Nomura, M., Horiuchi, O., Shibata, T. and Murakami, Y. (2008) 'A prototype of radial encoder', *Proceeding of JSPE Annual Meeting 2008 Spring*, Tokyo, Japan, pp.513, 514 (in Japanese).

Kimura, A., Arai, Y. and Gao, W. (2008) 'A two-degree-of-freedom linear encoder for measurement of position and straightness', *Proceeding of the 23rd Annual Meeting of ASPE and The 12th ICPE*, Portland, USA, pp.550–553.

Marsh, E., Couey, J. and Vallance, R. (2006) 'Roundness measurement of spherical artifacts at arbitrary latitude', *Precision Engineering*, Vol. 30, pp.353–356.

Marsh, E.R. (2008) *Precision Spindle Metrology*, DEStech Publications, Pennsylvania, pp.1–13.

Ogura, I. and Okazaki, Y. (2001) 'Precision measurement for axial and angular motion errors of turning spindle by using multi point method', *Journal of the Japan Society for Precision Engineering*, Vol. 67, pp.1120–1124 (in Japanese).

Okuyama, E., Nosaka, N. and Aoki, J. (2007) 'Radial motion measurement of high-revolution spindle motor', *Measurement*, Vol. 40, pp.64–74.

Park, Y.C. and Kim, S.W. (1994) 'Optical measurement of spindle radial motion by moiré technique of concentric gratings', *International Journal of Machine Tools and Manufacture*, Vol. 34, No. 7, pp.1019–1030.

Spencer, G.H. and Murty, M. (1962) 'General ray-tracing procedure', *J. Opt. Soc. Am.*, Vol. 52, p.672.

Websites

BD96@SONY Manufacturing System, http://assets.sonybiz.net/doc/sesdatasheets/BD96series_Eng.pdf

ROBONANO@FANUC, http://www.fanuc.co.jp/en/product/robonano/index.htm

SP4800@MicroE Systems, http://www.microesys.com/

Paper:

Spindle Error Motion Measurement Using Concentric Circle Grating and Phase Modulation Interferometers

Muhummad Madden*, Masato Aketagawa*, Shuhei Uesugi*,
Takuya Kumagai*, and Eiki Okuyama**

*Nagaoka University of Technology
1603-1 Kamitomioka, Nagaoka, Niigata 940-2188, Japan
E-mail: masatoaa@vos.nagaokaut.ac.jp
**Akita University
1-1 Tegatagakuenmachi, Akita 010-8502, Japan

In the conventional methods of measuring radial, axial, and angular motions of a spindle concurrently, complicated reference artifacts with relative large volume, e.g., two balls linked to a cylinder, are required. A simple and small artifact is favorable from the viewpoint of accurate measurement. This paper describes a concurrent measurement of radial, axial, and angular spindle motions using concentric circle grating and phase modulation interferometers. In the measurement, concentric circle grating with fine pitch is installed on top of the spindle of interest. The grating is a reference artifact in the method. Three optical sensors are fixed over the concentric circle grating, to observe its proper positions. The optical sensor consists of a frequency modulated laser diode as a light source as well as two interferometers. One interferometer observes an interference fringe between reflected light from a fixed mirror and 0-th order diffraction light from the grating to measure the axial motion. Another interferometer observes an interference fringe between ± 2nd order diffraction lights from the grating to measure the radial motion. Using three optical sensors, three axial displacements, and three radial displacements of the proper observed position of the grating can be measured. From these measured displacements, radial, axial, and angular motions of the spindle can be calculated concurrently. In this paper, a measurement instrument, a novel fringe interpolation technique using sinusoidal phase modulation, and experimental results are discussed.

Keywords: spindle, concentric circle grating, interferometer, sinusoidal phase modulation, fringe interpolation

1. Introduction

The industrial processes for ultra-precision engineering and metrology require fine quality control of products. The precision of rotary spindles is also required to enhance the accuracy of spindle motions to the nanometer and sub-μradian levels. The five degrees of freedom for spindle motion, or radial (2 degrees) + axial (1 degree) + angular (2 degrees), are identified as motion errors, and they must be eliminated or reduced. Conventional spindle motion error measurements are error separation methods, which require artifact reference and displacement sensors, such as capacitive sensors. Radial motion error can be measured using a precise sphere or circular cylinder [1–3]. A concentric circle grating is also used for measuring the radial motion error [4,5]. A precise circular cylinder with an end mirror surface can be used as the reference artifact for the concurrent measurement of (radial + axial) or (axial + angular) motions [6,7]. Using a sphere ball as a reference artifact, three degrees of freedom for spindle motion (radial (2 degrees) + axial (1 degree)) can be measured [8]. In addition, the concurrent measurement of radial, axial, and angular motions can be realized using the reference artifact of two sphere balls linked to a cylinder [8]. However, in the concurrent measurement of radial, axial, and angular motions, the artifact is voluminous and has too much mass to have the possibility of inhibiting the original rotational motion of the spindle. Moreover, capacitive sensors have narrow bandwidths, and maintaining the traceability against the meter definition is difficult because of their drift characteristic. As similar examples for multi-axes displacement measurement, 2-dimensional grating mirrors are used as fixed and moving mirrors in Michelson interferometers [9, 10]. This paper describes a concurrent measurement of spindle radial, axial, and angular motions using concentric circle grating and phase modulation interferometers. In this method, a concentric circle grating plate with a fine pitch is installed on top of the spindle of interest and is used as the reference artifact. Because the concentric circle grating plate is not voluminous and not heavy, this method can be applied to any spindle, and it does not affect the spindle original rotational motion. Since this method is based on wide-bandwidth photo sensors, it is possible to apply it to spindles with high rotational speeds. Moreover, this method is suitable for maintaining the traceability against the meter definition because it uses laser interferometers.
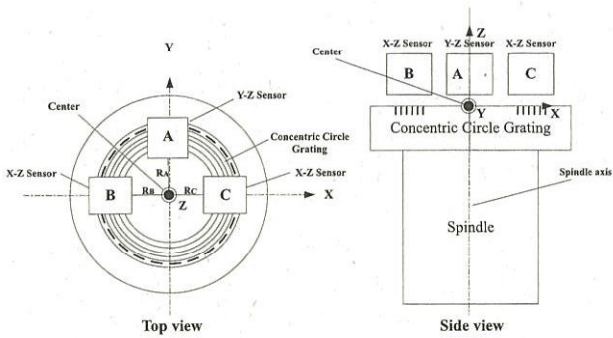
Fig. 1. Basic principle of spindle error motion measurement.

2. Measurement Principle

2.1. Spindle Error Motion Measurement

Figure 1 shows the measurement system of the spindle motion error using three optical sensors and the concentric circle grating. In the system, the Z-axis is the ideal rotation axis for the spindle. A concentric circle grating is set on top of the spindle of interest. Three optical sensors A, B, and C are fixed over the concentric circle grating. The rotation center of the spindle must be nearly aligned to the center of the concentric grating, within 1 μm or less. The grating plane must also be aligned nearly parallel to the XY plane within 10 arcsec.

In **Fig. 1**, the center is selected as the origin point of the XYZ coordinate system. The optical sensor A is located along the Y-axis with the distance R_A from the center, where it measures the Y-axis and Z-axis displacements y_A and z_A. Optical sensors B and C are located along the X-axis at distances R_B and R_C from the center, where they measure the X-axis and Z-axis displacements x_B, z_B, x_C, and z_C. From the displacements measured by the three optical sensors, the radial R_x, R_y, axial R_z, and angular θ_x, θ_y motions can be derived as follows [11]:

$$R_x = \frac{1}{2}(x_B + x_C), \qquad \ldots \ldots \ldots \ldots (1)$$

$$R_y = y_A, \qquad \ldots \ldots \ldots \ldots \ldots (2)$$

$$R_z = \frac{1}{3}(z_A + z_B + x_C), \qquad \ldots \ldots \ldots (3)$$

$$\theta_x = \frac{1}{R}\left(z_A - \frac{(z_B + z_C)}{2}\right), \qquad \ldots \ldots (4)$$

$$\theta_y = \frac{2}{R}(z_B - z_C), \qquad \ldots \ldots \ldots \ldots (5)$$

$$R = \frac{1}{3}(R_A + R_B + R_C), \qquad \ldots \ldots \ldots (6)$$

where R is the averaged distance of the interferometers A, B, and C from the center.

2.2. Optical Sensor

The optical sensors consist of a frequency modulated Laser Diode (LD) as a light source, and two interferometers. The configuration of the optical sensors is shown in
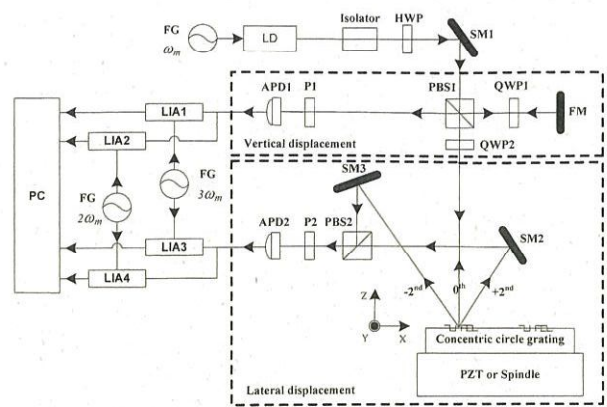
Fig. 2. Schematic diagram of the optical sensor, LD: laser diode; SM: steering mirror; FM: fixed mirror; HWP: half-wave plate; QWP: quarter-wave plate; PBS: polarized beam splitter; P: polarizer; APD: avalanched photodetector; LIA: lock-in amplifier, FG: function generator, PC: personal computer.

Fig. 2. To obtain displacements (Lissajous diagram), we apply the sinusoidal phase modulation techniques [12, 13] to the light source of the LD. We use the frequency modulation of the LD. The sinusoidal angular modulation frequency is ω_m. One interferometer observes an interference fringe between reflected light from a Fixed Mirror (FM) and 0-th order diffraction light from the grating. In this case, a light beam emitted from the laser is incident on Polarized Beam Splitter 1 (PBS1), and then, it is divided into two beams. The first beam reflected from PBS1 enters the Fixed Mirror (FM) via Quarter-Wave Plate 1 (QWP1), bounces off the FM, and reaches Avalanche PhotoDetector 1 (APD1) via PBS1 and Polarizer 1 (P1). The second beam, which goes through PBS1, reaches the concentric circle grating via QWP2.

In **Fig. 2**, we assume that the incident angle θ_i of the second beam to the grating is almost null. Thus, the reflected light (0-th order diffraction light) reaches APD1 via QWP2, PBS1, and P1. At APD1, it is possible to detect an interferometer fringe between the reflection lights from the FM and the grating, and to measure the displacement along the Z-axis of the grating. Another interferometer observes an interference fringe between $+2^{nd}$ and -2nd order diffraction lights from the concentric circle grating. In this case, the $+2^{nd}$ and -2nd order diffraction light from the grating through the steering mirror 2/3 (SM2/3) and reaches Avalanche PhotoDetector 2 (APD2) via PBS2 and Polarizer 2 (P2). If the incident angle on the XZ plane is negligibly small, the $\pm$ 2nd-order diffraction angles θ_{+2} and θ_{-2} (on XZ plane) can be derived as follows:

$$d(\sin\theta_{+2} - \sin\theta_{iXZ}) = +2\lambda, \qquad \ldots \ldots (7)$$

$$d(\sin\theta_{-2} - \sin\theta_{iXZ}) = -2\lambda, \qquad \ldots \ldots (8)$$

where d is a grating pitch and λ is a wavelength of the light source. In **Fig. 2**, we assume that Δz and Δx are the displacement shifts of the grating along the Z-axis, and

X-axis, respectively. The observed light intensity of I_{0F} and $I_{\pm 2}$ at APD1 and APD2 is represented as follows:

$$I_{0F} = |E_0|^2 + |E_F|^2$$
$$+ 2E_0 E_F \cos\left\{ \varphi_{\text{int},0} - \frac{4\pi n}{c} f(L_{\text{int}} + \Delta z) \right\}$$
$$\cdots \cdots \cdots \cdots \cdots \cdots \cdots (9)$$

$$I_{\pm 2} = |E_{+2}|^2 + |E_{-2}|^2$$
$$+ 2E_{+2} E_{-2} \cos\left\{ \varphi_{\text{int},\pm 2} - \frac{8\pi n}{c} f L_{\pm 2} - \frac{8\pi}{d} \Delta x \right\}$$
$$\cdots \cdots \cdots \cdots \cdots (10)$$

where E_0, E_F, E_{+2}, E_{-2}, $\varphi_{\text{int},0}$, $\varphi_{\text{int},\pm 2}$, n, c, f, L_{int} and $L_{\pm 2}$ are the amplitudes of the lights reflected from 0th order diffraction of the grating and FM, the amplitudes of the lights diffracted from $\pm 2^{\text{nd}}$ order of the grating, the initial phase of the 0th order interferometer, the initial phase of the $\pm 2^{\text{nd}}$ order interferometer, the refractive index of air, the speed of light, the frequency of the light source, the optical path difference of the 0th order interferometer arms, and the optical path difference of the $\pm 2^{\text{nd}}$ order interferometer arms, respectively. In the system, the vertical displacement Δz is assumed to be of the same order as the wavelength of the LD, i.e., $\Delta z \sim \lambda$. We add a little modulation to the frequency of LD:

$$f = f_0 + \Delta f \quad \cdots \cdots \cdots \cdots (11)$$

where f_0 and Δf are the center frequency and modulation. We assume the following:

$$\frac{\Delta f}{f_0} \ll 1 \quad \left(\frac{\Delta \lambda}{\lambda} \ll 1 \right) \quad \cdots \cdots \cdots (12)$$

$\Delta \lambda$ is the wavelength modulation. In Eq. (9), the 2nd content of the blanket can be calculated as:

$$\frac{4\pi n}{c}(f_0 + \Delta f)(L_{\text{int}} + \Delta z) =$$
$$\frac{4\pi n}{c} f_0 (L_{\text{int}} + \Delta z) + \frac{4\pi n}{c} \Delta f - \frac{4\pi n}{\lambda^2} \Delta \lambda \Delta z$$
$$\cdots \cdots \cdots \cdots \cdots (13)$$

The order of the last term of the Eq. (13) is

$$\left| -4\pi n \frac{\Delta \lambda}{\lambda} \frac{\Delta z}{\lambda} \right| \sim \left| \frac{4\pi n}{c} \frac{\Delta \lambda}{\lambda} \right| \ll 1 \quad \cdots \cdots (14)$$

Therefore Eq. (9) can be represented as follows:

$$I_{0F} = |E_0|^2 + |E_F|^2 + 2E_0 E_F \cos\left\{ \varphi_{\text{int},0} \right.$$
$$\left. - \frac{4\pi}{c} n L_{\text{int}} f_0 - \frac{4\pi}{c} n f_0 \Delta z - \frac{4\pi}{c} n L_{\text{int}} \Delta f \right\}$$
$$= |E_0|^2 + |E_F|^2$$
$$+ 2E_0 E_F \cos\left\{ \varphi_0' - \frac{4\pi}{c} n f_0 \Delta z - \frac{4\pi}{c} n L_{\text{int}} \Delta f \right\}$$
$$\cdots \cdots \cdots \cdots \cdots (15)$$

where $\varphi_0' (= \varphi_{\text{int},0} - \{(4\pi)/c\} n L_{\text{int}} f_0)$ is an initial phase of interferometer. We add the sinusoidal modulation to $(-\{(4\pi)/c\} n L_{\text{int}} \Delta f)$ using

$$-\frac{4\pi}{c} n L_{\text{int}} \Delta f = k_{m,0} \sin \omega_m t. \quad \cdots \cdots (16)$$

where $k_{m,0}$ is a modulation depth. By combining Eqs. (15) and (16) and using the Bessel function, we obtain,

$$I_{0F} = |E_0|^2 + |E_F|^2 + 2E_0 E_F \left[\cos\left(\varphi_0' - \frac{4\pi}{c} n f_0 \Delta z \right) \right.$$
$$\left\{ J_0(k_{m,0}) + 2 \sum_{m=1}^{\infty} J_{2m}(k_{m,0}) \cos 2m\omega_m t \right\}$$
$$- \sin\left(\varphi_0' - \frac{4\pi}{c} n f_0 \Delta z \right)$$
$$\left. \left\{ 2 \sum_{m=n}^{\infty} J_{2m+1}(k_{m,0}) \sin(2m+1)\omega_m t \right\} \right],$$
$$\cdots \cdots \cdots \cdots \cdots (17)$$

In order to reduce the effect from the amplitude modulation of LD, we select the 2nd-harmonic ($2\omega_m$) and the 3rd-harmonic ($3\omega_m$). We apply the reference signal of the 2nd-harmonic cosine wave ($2\omega_m$) and the reference signal of the 3rd-harmonic sine wave ($3\omega_m$) to the lock-in detection signal of the interference light intensity I_{0F}. When the interference light intensity I_{0F} from Eq. (17) is synchronized by the Lock-In Amplifier 1 (LIA1) with the reference signal of the 3rd-harmonic sine wave ($3\omega_m$) and the Lock-In Amplifier 2 (LIA2) with the reference signal of 2nd-harmonic cosine wave ($2\omega_m$) (**Fig. 2**), two signals of LIA1 and LIA2 can be written as follows:

$$I_{0F}(3\omega_m) = -2E_0 E_F J_3(k_{m,0}) \sin\left(\varphi_0' - \frac{4\pi}{c} n f_0 \Delta z \right) \quad (18)$$

and

$$I_{0F}(2\omega_m) = 2E_0 E_F J_2(k_{m,0}) \cos\left(\varphi_0' - \frac{4\pi}{c} n f_0 \Delta z \right). \quad (19)$$

where $J_2(k_{m,0})$ and $J_3(k_{m,0})$ are the Bessel function of 2nd and 3rd-order. The interference light intensity $I_{\pm 2}$ of the $\pm$ 2nd-order diffraction at APD2 is written as follows:

$$I_{\pm 2} = |E_{+2}|^2 + |E_{-2}|^2 + 2E_{+2} E_{-2} \left[\cos\left(\varphi_{\pm 2}' - \frac{8\pi}{d} \Delta x \right) \right.$$
$$\left\{ J_0(k_{m,\pm 2}) + 2 \sum_{m=1}^{\infty} J_{2m}(k_{m,\pm 2}) \cos 2m\omega_m t \right\}$$
$$- \sin\left(\varphi_{\pm 2}' - \frac{8\pi}{d} \Delta x \right)$$
$$\left. \left\{ 2 \sum_{m=n}^{\infty} J_{2m+1}(k_{m,\pm 2}) \sin(2m+1)\omega_m t \right\} \right]$$
$$\cdots \cdots \cdots \cdots \cdots (20)$$

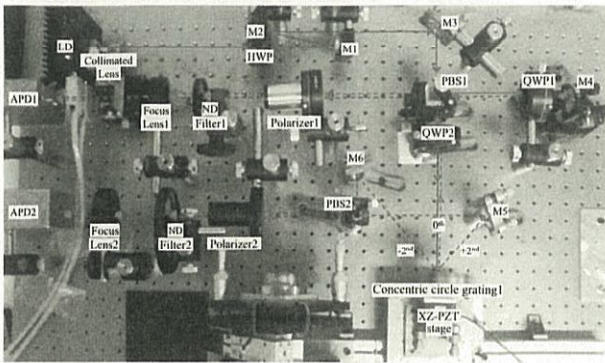where $\varphi_{\pm 2}'$ is the initial phase of the interferometer, and

Fig. 3. Schematic photograph of the experimental setup for measurement of the XZ stage motion.

Table 1. Measurement conditions applied to the XZ stages.

Modulation frequency for LD	20 [kHz]
Amplitude of PZTstage	1 [μm]
Frequency of PZTstage	1 [Hz]
Motion shape	Triangular
Sampling time	6 [s]
Cut off frequency of low pass filter of LIA	300 [Hz]

Fig. 4. Concentric circle grating (2 μm pitch).

$k_{m,\pm2}$ is the modulation depth. When the interference light intensity $I_{\pm2}$ from Eq. (20) is synchronized by the Lock-In Amplifier 3 (LIA3) with the reference signal of the 3rd-harmonic sine wave ($3\omega_m$) and the Lock-In Amplifier 4 (LIA4) with the reference signal of the 2nd-harmonic co-sine wave ($2\omega_m$) (**Fig. 2**), two signals of LIA3 and LIA4 can be written as follows:

$$I_{\pm2}(3\omega_m) = -2E_{+2}E_{-2}J_3(k_{m,\pm2})\sin\left(\varphi'_{\pm2} - \frac{2\pi}{d}\Delta x\right)$$

$$\cdots\cdots\cdots\cdots\cdots\cdots\cdots (21)$$

and

$$I_{\pm2}(2\omega_m) = 2E_{+2}E_{-2}J_2(k_{m,\pm2})\cos\left(\varphi'_{\pm2} - \frac{2\pi}{d}\Delta x\right).$$

$$\cdots\cdots\cdots\cdots\cdots\cdots\cdots (22)$$

From Eqs. (18), (19), (21) and (22), we can obtain a Lissajous diagram from two reference signals with a phase difference of 90° [14]. By using the Lissajous diagram, the axial (Z-axis) and radial (X-axis) displacements of the grating can be calculated concurrently.

3. Preliminary Experiment and Discussion

3.1. Motion Measurement of XZ Stage Using One Optical Sensor

In order to confirm Eqs. (18), (19), (21) and (22), we constructed the grating interferometer shown in **Fig. 3**. In the experiment, the concentric circle grating with a pitch of 2 μm was set up on the XZ stage, which was driven by a piezo-electric actuator. An LD, with a wavelength of 635 nm and a sinusoidal phase modulation frequency of 20kHz, was applied to the interferometer as a light source. APD1 detected the interference signal of Z-axis displacement, and APD2 detected the interference signal of X-axis displacement. The measurement conditions applied to the XZ stage motion are shown in **Table 1**. We applied a triangular motion with an amplitude of 1 μm and a frequency of 1Hz to the XZ stage. The measurement time was 6 seconds, and the cut off frequency of the low pass

(a) Z-axis displacement   (b) X-axis displacement

Fig. 5. Lissaajous diagram of the XZ stage motion measurement.

filter of the lock-in amplifier was 300Hz.

Figure 4 is a photograph of the concentric circle grating. The fine concentric circle grating is the key technology in terms of the attainment of our measurement goal. The grating was fabricated using an ultra-precise Numerical Control (NC) cutting machine tool (ROBO-NANO@FANUC) and a sharp monocrystalline diamond tool with a top radius of less than 1 μm. The material used was stainless steel with nickel phosphide plating 100 μm thick. Many grating grooves were formed on the nickel phosphide plate. In the grating, 1000 pitches were formed with a concentric circle structure.

Lissajous figures of Z-axis and X-axis displacements of the XZ stage motion measurement can be seen in **Fig. 5**.
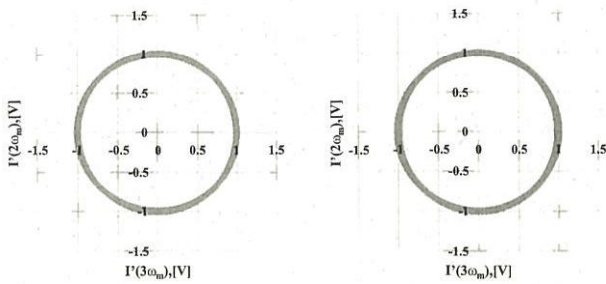
(a) Z-axis displacement   (b) X-axis displacement

Fig. 6. Standardized Lissajous diagram of XZ stage motion measurement.

Fig. 7. The axial (Z-axis) motion of the XZ stage.

Fig. 8. The radial (X-axis) motion of the XZ stage.

(a) Z-axis displacement   (b) X-axis displacement

Fig. 9. Lissajous diagram of the XZ stage motion measurement after reduction of the nonlinear errors.
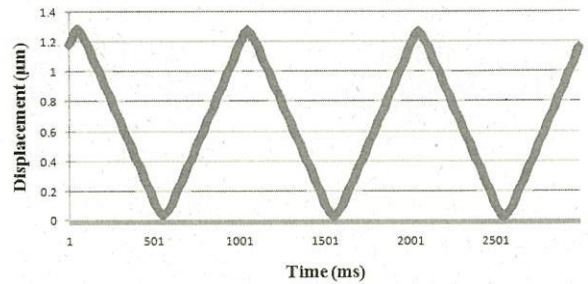
Fig. 10. The axial (Z-axis) motion of the XZ stage after reduction of the nonlinear errors.

Fig. 11. The radial (X-axis) motion of the XZ stage after reduction of the nonlinear errors.

The Lissajous diagrams are deformed due to variations in laser beam intensity, and the center of the Lissajous diagram is not the same as the origin. In this case, the normalized Lissajous diagram can be calculated using the following equation:

$$I'(3\omega_m) = \frac{I(3\omega_m)J_2(k_m)}{\sqrt{(I(2\omega_m)J_3(k_m))^2 + (I(3\omega_m)J_2(k_m))^2}}$$

$$= \sin\left(\frac{4\pi}{\lambda}\Delta z + \varphi_0\right) \quad \dots \dots \quad (23)$$

and

$$I'(2\omega_m) = \frac{I(2\omega_m)J_3(k_m)}{\sqrt{(I(2\omega_m)J_3(k_m))^2 + (I(3\omega_m)J_2(k_m))^2}}$$

$$= \cos\left(\frac{4\pi}{\lambda}\Delta z + \varphi_0\right) \quad \dots \dots \quad (24)$$

The normalized Lissajous diagram is shown in **Fig. 6**. In **Fig. 6**, the center and radius of the diagram are the origin and 1, respectively. The axial (Z-axis) and radial (X-axis) motions of the XZ stage are shown in **Figs. 7** and **8**, respectively. In **Figs. 7** and **8**, the nonlinear errors (or cyclic error) due to the polarization mixing of two interferometer arms can be seen. If there is no cyclic error, measured motions must be triangular. However, the nonlinear error can be reduced by the polarization adjustment of two interferometer arms. **Fig. 9** is a Lissajous diagram of the Z-axis and X-axis displacements of the XZ stage motion after the polarization adjustment. In **Fig. 9**, the center of the Lissajous diagram is closer to the origin than

it is in **Fig. 5**. **Fig. 10** shows the axial (Z-axis) motions and **Fig. 11** shows the radial (X-axis) motion of the XZ stage after the polarization adjustment. From **Figs. 10** and **11**, it can be seen that the polarization adjustment can reduce
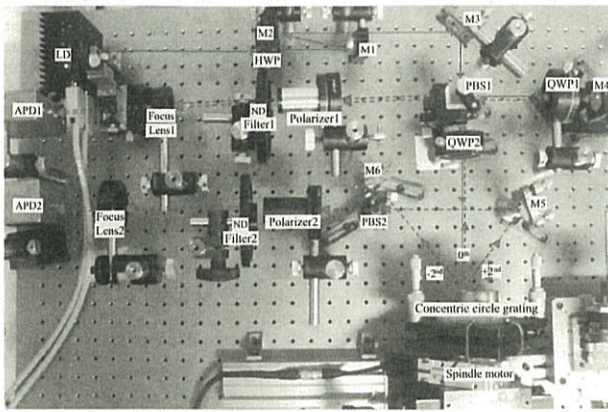
Fig. 12. Schematic photograph of the experimental setup
for measurement of the spindle error motion.

Table 2. The specifications of the spindle motor.

Diameter of motor stage	60 [mm]
Accuracy of position	0.15° [degree]
Axial error (Maximum)	0.06 [mm]
Radial error (Maximum)	0.03 [mm]
Maximum speed	40°/sec [degree/sec]

Table 3. Measurement conditions applied to the spindle motion.

Modulation frequency for LD	33 [kHz]
Revolution speed of spindle	4 [rpm]
Number of rotation	5 rotations
Sampling rate	10 [kHz]
Cut off frequency of low pass filter of LIA	300 [Hz]

cyclic error of the two interferometers. In the near future,
we will clarify the quantitative relationship between the
cyclic error and the polarization mixing in the interferom-
eters.

3.2. Measurement of Spindle Radial and Axial Motions Using One Optical Sensor

We also constructed the spindle error motion measure-
ment system shown in **Fig. 12**. In the experiment, concen-
tric circle grating with a pitch of 2 μm was set up on the
spindle motor (ARS-636-HM; Chuo Precision). **Table 2**
lists the specifications of the spindle motor. In the ex-
periment, its maximum speed was 40°/sec, or 4rpm. The
measurement conditions applied to the spindle motion are
shown in **Table 3**. The spindle was rotated at low speed,
4rpm. We measured the spindle motion over 5 rotations.
The cut off frequency of the low pass filter of the lock-in
amplifier was 300Hz.

Figures 13 and **14** are Lissajous diagrams and normal-
ized Lissajous diagrams of the axial (Z-axis) and radial
(X-axis) displacements of the spindle motion during 1 ro-

(a) Z-axis displacement   (b) X-axis displacement
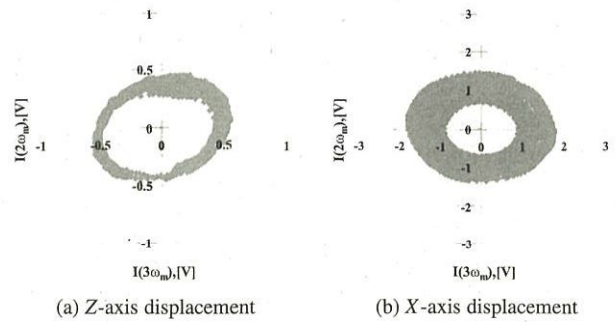
Fig. 13. Lissaajous diagram of the spindle error motion
measurement.

(a) Z-axis displacement   (b) X-axis displacement
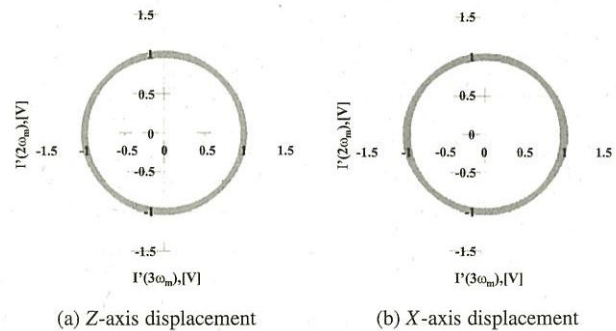
Fig. 14. Standardized Lissajous diagram of spindle error
motion measurement.
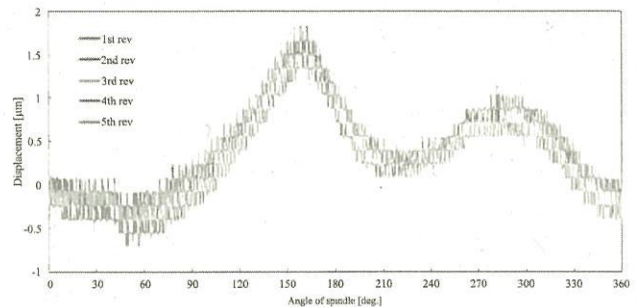
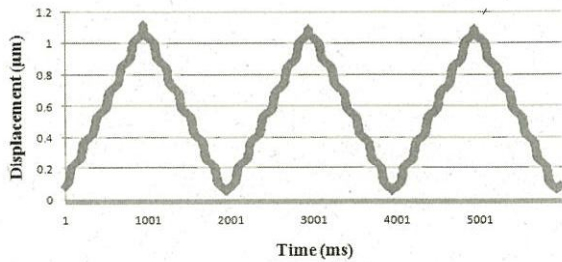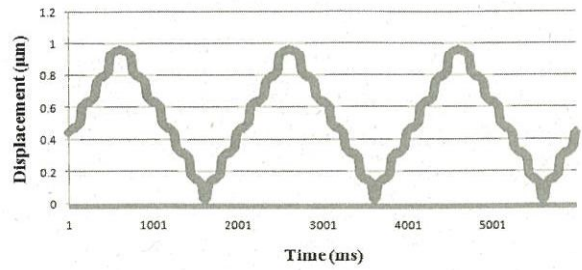Fig. 15. Axial motion (Z-axis) of the spindle.

tation. The axial (Z-axis) and radial (X-axis) motions of
the spindle for the speed of 4rpm with 5 rotations are
shown in **Figs. 15** and **16**, respectively. Since we could
not adjust the center of the grating to the rotation center of
the spindle within less than 80 μm, a large radial motion
of around 80 μm can be seen in **Fig. 16**. The repeatability
of Z- and X-axis motion measurement is approximately
several μm. The experiment results show that the pro-
posed method can measure the displacement of the grat-
ing using fringe interpolation. We can apply three optical
sensors for concurrent measurement of radial, axial, and
angular motions of a spindle.
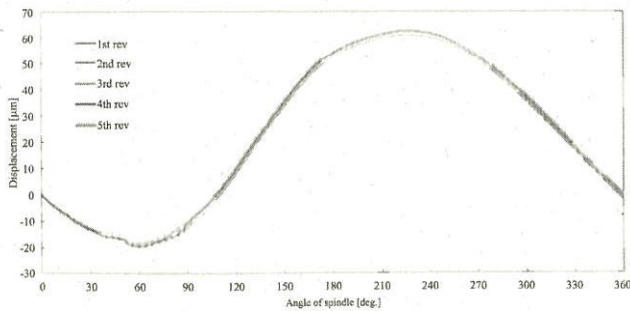
Fig. 16. Radial motion (*X*-axis) of the spindle.

4. Conclusion and Future Study

In this paper, we have proposed a measurement method using concentric circle grating and phase modulation interferometers to measure the spindle radial, axial, and angular motions concurrently. The measurement principle of the optical sensor using a concentric circle grating to measure the displacement was clarified. The displacement (Lissajous diagram) could be obtained when we added a small amount of modulation to the frequency of the light source. If there was deformation of the Lissajous diagram due to variations in laser source intensity, a normalized Lissajous diagram could be obtained.

By using one optical sensor, we were able to measure spindle radial and axial motions concurrently. Based on the results, we are planning to construct a concurrent measurement system of spindle radial, axial, and angular motions using three optical sensors in the near future. Moreover, we think it is possible to control or reduce the spindle radial, axial, and angular motions using our proposed method.

References:

[1] R. Donaldson, "A simple method for separating spindle error from test ball roundness error," Annals of the CIRP, Vol.21, pp. 125-126, 1972.

[2] E. Marsh, J. Couey, and R. Vallance, "Roundness measurement of spherical artifacts at arbitrary latitude," Precision Engineering, Vol.30, pp. 353-356, 2006.

[3] E. Okuyama, N. Nosaka, and J. Aoki, "Radial motion measurement of high-revolution spindle motor," Measurement, Vol.40, pp. 64-74, 2007.

[4] Y. C. Park and S. W. Kim, "Optical measurement of spindle radial motion by Moiré technique of concentric gratings," Int. J. Machine Tools and Manufacture, Vol.34, No.7, pp. 1019-1030, 1994.

[5] A. Kataoka, M. Nomura, O. Horiuchi, T. Shibata, and Y. Murakami, "A prototype of Radial Encoder," Proc. of JSPE Annual Spring Meeting, Tokyo, Japan, pp. 513-514, 2008. (in Japanese)

[6] W. Gao, T. Takahara, and S. Kiyono, "On machine measurement of angular motion of spindle," Proc. of ASPE Annual Meeting, St. Luis, p. 355, 1998.

[7] I. Ogura and Y. Okazaki, "Precision measurement for axial and angular motion errors of turning spindle by using multi point method," J. of JSPE, Vol.67, pp. 1120-1124, 2001. (in Japanese)

[8] E. R. Marsh, "Precision Spindle Metrology," DEStech Publications, Pennsylvania, pp. 1-13, 2008.

[9] W. Gao and A. Kimura, "A Three-axis displacement sensor with nanometric resolution," Annals. of the CIRP, Vol.56, No.1, pp. 529-532, 2007.

[10] A. Kimura, Y. Arai, and W. Gao, "A two-degree-of-freedom linear encoder for measurement of position and straightness," Proc. of ASPE Annual and ICPE Meeting, Portland, USA, pp. 550-553, 2008.

[11] M. Madden, M. Aketagawa, Y. Ohkubo, S. Kimura, H. Maruyama, S. Higuchi, and E. Okuyama, "Proposal of concurrent measurement method for spindle radial, axial and angular motios using concentric grating interferometers," Int. J. of Surface Science and Engineering, Vol.3, No.3, pp. 242-252, 2009.

[12] O. Sasaki and H. Okasaki, "Sinusoidal phase modulating interferometry for surface profile measurment," Applied Optics, Vol.52, No.18, pp. 3137-3140, 1986.

[13] A. Dandridge, A. B. Tveten, and T. G. Giallorenzi, "Homodyne demodulation scheme for fiber optic sensors using phase generated carrier," IEEE J. of Quantum Electronics, Vol.18, No.10, pp. 1647-1653, 1982.

[14] S. Uesugi, M. Madden, T. Kumagai, Y. Maeda, and M. Aketagawa, "Concurrent measurement of radial, axial and angular motions of spindle using concentric circle grating interferometers," Proc. of JSPE Annual Autumn Meeting, Fukuoka, Japan, pp. 927-928, 2012. (in Japanese)

Name:
Muhummad Madden

Affiliation:
Ph.D. Student, Aketagawa Laboratory, Department of Mechanical Engineering, Nagaoka University of Technology

Address:
1603-1 Kamitomioka, Nagaoka, Niigata 940-2188, Japan

Brief Biographical History:
2002- Metrologist, Length Laboratory, National Institute of Metrology, Thailand
2008- Master Student, Nagaoka University of Technology
2010- Ph.D. Student, Nagaoka University of Technology

Main Works:
• "Proposal of concurrent measurement method for spindle radial, axial and angular motions using concentric grating interferometers," Int. J. of Surface Science and Engineering, Vol.3, No.3, pp. 242-252, 2009.

Membership in Academic Societies:
• The Japan Society for Precision Engineering (JSPE)
• The International Society for Optics and Photonics (SPIE)

Name:
Masato Aketagawa

Affiliation:
Professor, Department of Mechanical Engineering, Nagaoka University of Technology

Address:
1603-1 Kamitomioka, Nagaoka, Niigata 940-2188, Japan
Brief Biographical History:
1985 Canon Inc.
1991 Research Associate, Nagaoka University of Technology
1999 Associate Professor, Nagaoka University of Technology
2011 Professor, Nagaoka University of Technology
Main Works:
• "Ultraslow strain rate measurement system for ice using modified phase modulation homodyne interferometer," Institute of Physics, Measurement Science & Technology, Vol.22, No.2, 035702, 2011.
Membership in Academic Societies:
• The Japan Society for Precision Engineering (JSPE)
• The Optical Society of Japan (OSJ)
• The Japan Society of Applied Physics (JSAP)
• The American Society for Precision Engineering (ASPE)
• Optical Society of America (OSA)

Name:
Eiki Okuyama

Affiliation:
Associate Professor, Akita University

Address:
1-1 Tegatagakuenmachi, Akita 010-8502, Japan
Brief Biographical History:
1985-1991 Assistant Researcher, Akita National College of Technology, Japan
1991-1996 Assistant Researcher, Akita University, Japan
1995 Visiting Fellow, University of Warwick, UK
1996- Associate Professor, Akita University, Japan
Main Works:
• E. Okuyama, "Multi-probe Method for Straightness Profile Measurement Based on Least Uncertainty Propagation," Precision Engineering, Vol.34, Issue 1, pp. 49-54, 2010.
Membership in Academic Societies:
• The Japan Society for Precision Engineering (JSPE)
• European Society for Precision Engineering and Nanotechnology (euspen)

Name:
Shuhei Uesugi

Affiliation:
Master Student, Aketagawa Laboratory, Department of Mechanical Engineering, Nagaoka University of Technology
Address:
1603-1 Kamitomioka, Nagaoka, Niigata 940-2188, Japan

Name:
Takuya Kumagai

Affiliation:
Master Student, Aketagawa Laboratory, Department of Mechanical Engineering, Nagaoka University of Technology
Address:
1603-1 Kamitomioka, Nagaoka, Niigata 940-2188, Japan

Concurrent measurement method of spindle radial, axial and angular motions using concentric circle grating and phase modulation interferometers

Muhummad Madden[1]**, Masato Aketagawa**[1]**, Takuya Kumagai**[1]**, Yoshitaka Maeda**[1] **and Eiki Okuyama**[2]

[1] Department of Mechanical Engineering, Nagaoka University of Technology, 1603–1 Kamitomioka, Nagaoka, Niigata, 940-2188 Japan
[2] Department of Mechanical Engineering, Akita University, 1–1 Tegatagakuenmachi, Akita, 010-8502 Japan

E-mail: masatoaa@vos.nagaokaut.ac.jp

Abstract

This paper describes a concurrent measurement of spindle radial, axial and angular motions using concentric circle grating and phase modulation interferometers. In the measurement, a concentric circle grating with fine pitch is the reference artifact. A frequency modulated laser diode is used for the light source of the phase modulation interferometers. The phase modulation interferometers, which consist of three Michelson and three grating interferometers, measure three radial and three axial displacements of the grating. From these six measured displacements, radial, axial and angular motions of a spindle can be determined concurrently. In the paper, a measurement principle, a measurement instrument and experimental results are discussed. Concurrent measurements of spindle radial, axial and angular motions were successfully attained.

Keywords: spindle, radial motion, axial motion, angular motion, Michelson interferometer, grating interferometer, sinusoidal phase modulation

(Some figures may appear in colour only in the online journal)

1. Introduction

Industrial processes for ultra-precision engineering and metrology require fine quality control of products. The precision of rotary spindles is also required. It is necessary to enhance the accuracy of spindle motions at nanometer and sub-μradian levels [1, 2]. Ideal spindles must have rotary motion with only one degree of freedom; therefore, any extra motions with five degrees of freedom (= radial (2 degrees) + axial (1 degree) + angular (2 degrees)) are identified as error motions which must be eliminated or reduced. Conventional spindle error motion measurements are error separation methods [3–5], which require artifact reference and displacement sensors such as capacitive sensors. Radial error motion

can be measured using a precise sphere or circular cylinder as a reference artifact [3–5]. A concentric circle grating is also used as the reference artifact for measuring radial error motion [6, 7]. A precise circular cylinder with an end mirror surface can be used as the reference artifact for the concurrent measurement of (radial + axial) or (axial + angular) motions [8, 9]. Using a sphere ball as the reference artifact, spindle error motions (radial (2 degrees) + axial (1 degree)) can be measured [10]. In addition, the concurrent measurement of radial (2 degrees), axial (1 degree) and angular (2 degrees) motions can be realized using a reference artifact of two sphere balls linked with a cylinder [10]. However, in the concurrent measurement of radial, axial and angular motions, this artifact is voluminous and has too much mass and has
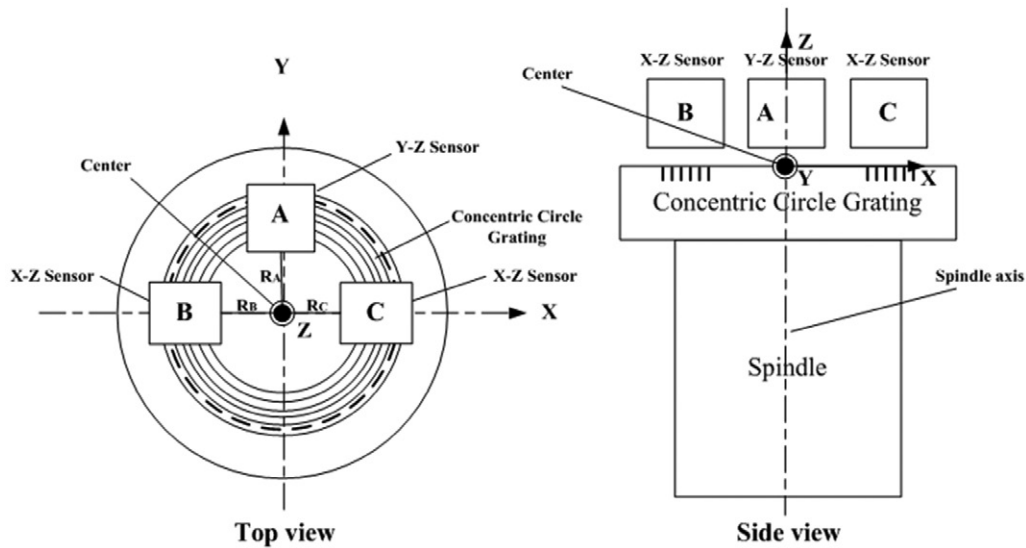
Figure 1. Basic principle of spindle error motion measurement.

the possibility of inhibiting the original rotational motion of the spindle. Moreover, capacitive sensors have narrow bandwidths, and maintaining traceability against the meter definition is difficult because of their drift characteristic. As similar examples for multi-axes displacement measurement, 2-dimensional grating mirrors are used as fixed and moving mirrors in Michelson interferometers [11, 12].

This paper describes the concurrent measurement of spindle radial, axial and angular motions using a concentric circle grating and phase modulation interferometers. In this method, a concentric circle grating plate with a fine pitch is installed on top of the spindle of interest and is used as the reference artifact. Because the concentric circle grating plate is not voluminous and not heavy, this method is effective for any spindle, and does not affect the spindle's original rotational motion. Since this method is based on wide-bandwidth photo sensors, it is possible to apply it to high- rotational-speed spindles. Moreover, this method is suitable for maintaining traceability against the meter definition through calibration of the wavelength of the light source and grating pitch using a measurement standard.

2. Measurement principle

2.1. Spindle error motion measurement

Figure 1 shows a measurement system of spindle error motions using three optical sensors and a concentric circle grating. In the system, the z-axis is the ideal rotation axis for the spindle. A concentric circle grating is set on top of the spindle of interest. Three optical sensors, A, B and C, are fixed over the concentric circle grating. In order to reduce the centering error, the spindle rotation center must be nearly aligned to the center of the concentric circle grating. The grating plane must be aligned to be nearly parallel with the XY plane – within 10 arcseconds to reduce the crosstalk error [13]. In figure 1, the spindle rotation center is selected as the origin point of the XYZ coordinate system. Optical sensor A is located along

the y-axis, with a distance R_A from the center and measures the y-axis and z-axis displacements y_A and z_A, whereas optical sensors B and C are located along the x-axis with a distances R_B and R_C from the center, and measure the x-axis and z-axis displacements x_B, z_B, x_C and z_C. From the measured displacements by the three optical sensors, the radial R_x, R_y, axial R_z and angular θ_x, θ_y motions can be derived as [13]

$$R_x = \frac{1}{2}(x_B + x_C), \qquad (1)$$

$$R_y = y_A, \qquad (2)$$

$$R_z = \frac{1}{3}(z_A + z_B + z_C), \qquad (3)$$

$$\theta_x = \frac{1}{R}\left(z_A - \frac{(z_B + z_C)}{2}\right), \qquad (4)$$

$$\theta_y = \frac{1}{2R}(z_B - z_C), \qquad (5)$$

$$R = \frac{1}{3}(R_A + R_B + R_C), \qquad (6)$$

where R is the averaged distance of the interferometers A, B and C from the center.

2.2. Optical sensor

The optical sensor consists of a frequency modulated laser diode (LD) as a light source, and two interferometers (one Michelson + one grating interferometers). The configuration of the optical sensor is shown in figure 2. To obtain displacements (Lissajous diagram), we apply sinusoidal phase modulation techniques [14, 15] to the light source LD. We use the frequency modulation of the LD. The sinusoidal angular modulation frequency is ω_m. One interferometer observes the interference fringe between the reflected light
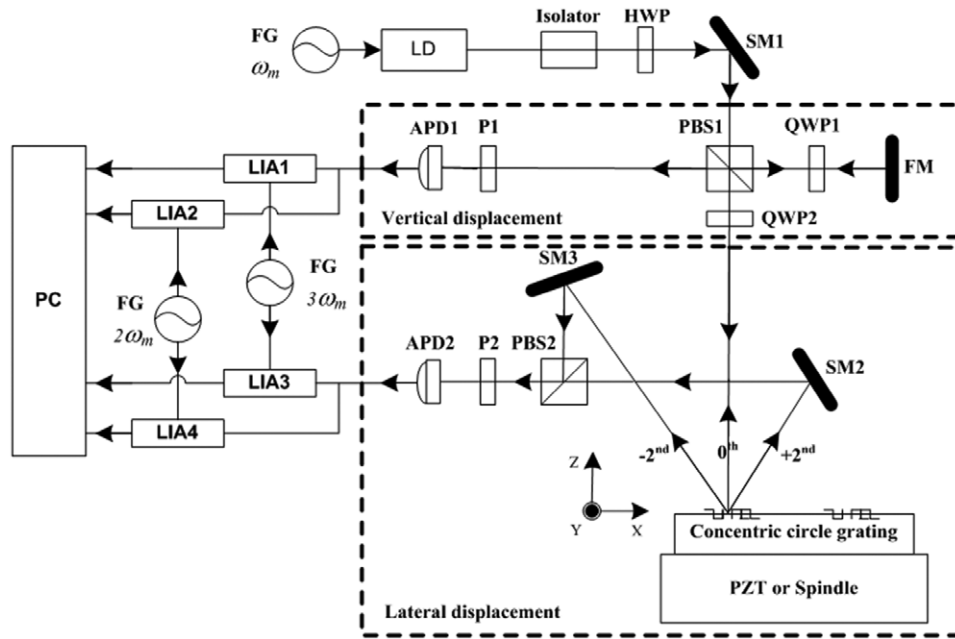
Figure 2. Schematic diagram of the optical sensor. LD: laser diode; SM: steering mirror; FM: fixed mirror; HWP: half-wave plate; QWP: quarter-wave plate; PBS: polarized beam splitter; P: polarizer; APD: avalanche photodetector; LIA: lock-in amplifier, FG: function generator, PC: personal computer.

from a fixed mirror (FM) and the 0th order diffraction light from the grating. In this case, a light beam emitted from the laser is incident on a polarized beam splitter 1 (PBS1), and then is divided into two beams. The first beam reflected from PBS1 enters the fixed mirror (FM) via quarter-wave plate 1 (QWP1) and bounces from FM and reaches avalanche photodetector 1 (APD1) via PBS1 and polarizer 1 (P1). The second beam, which goes through PBS1, reaches the concentric circle grating via QWP2. In figure 2, we assume that the incident angle θ_i of the second beam to the grating is almost null. Thus, the reflected light (= 0th order diffraction light) reaches APD1 via QWP2, PBS1 and P1. At APD1, it is possible to detect an interferometer fringe between the reflection lights from FM and the grating, and to measure the displacement along the z-axis of the grating. Another interferometer observes the interference fringe between +2nd and −2nd order diffraction lights from the concentric circle grating. We use +2nd and −2nd order diffraction lights because the lights are stronger than the other order diffraction lights. In this case, the +2nd and −2nd order diffraction lights from the grating through the steering mirror 2/3 (SM2/3) and reaches avalanche photodetector 2 (APD2) via PBS2 and polarizer 2 (P2). If the incident angle to XY plane θ_{iXZ} is negligibly small, the ±2nd-order diffraction angles θ_{+2} and θ_{-2} (on XZ plane) can be derived as

$$d(\sin\theta_{+2} - \sin\theta_{iXZ}) = d\sin\theta_{+2} = +2\lambda, \quad (7)$$

$$d(\sin\theta_{-2} - \sin\theta_{iXZ}) = d\sin\theta_{-2} = -2\lambda, \quad (8)$$

where d is a grating pitch and λ is a wavelength of the light source. In figure 2, we assume that Δz and Δx are the displacement shifts of the grating along the z-axis, and x-axis, respectively. The observed light intensity of I_{0F} and $I_{\pm 2}$ at APD1 and APD2 is represented as
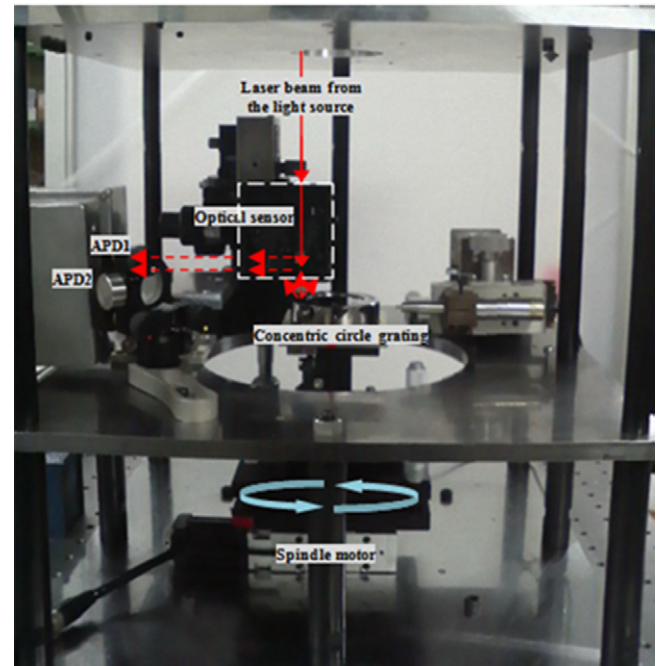
Figure 3. Schematic photograph of the experimental setup for the spindle motion measurement using one optical sensor.

$$I_{0F} = |E_0|^2 + |E_F|^2 + 2E_0 E_F \cos\left\{ \varphi_{int,0} - \frac{4\pi n}{c} f(L_{int} + \Delta z) \right\}, \quad (9)$$

$$I_{\pm 2} = |E_{+2}|^2 + |E_{-2}|^2 + 2E_{+2}E_{-2} \cos\left\{ \varphi_{int,\pm 2} - \frac{8\pi n}{c} f L_{\pm 2} - \frac{8\pi}{d}\Delta x \right\}, \quad (10)$$

where $E_0, E_F, E_{+2}, E_{-2}, \varphi_{int0}, \varphi_{int\pm 2}, n, c, f, L_{int}$ and $L_{\pm 2}$ are the amplitudes of the lights reflected from 0th order diffraction of the grating and FM, the amplitudes of the lights

Diameter of motor stage	60 [mm]
Accuracy of position	0.15 °[degree]
Axial error (Maximum)	0.06 [mm]
Radial error (Maximum)	0.03 [mm]
Maximum speed	24 °/sec[degree/sec]

Table 2. Measurement conditions applied to the spindle motion.

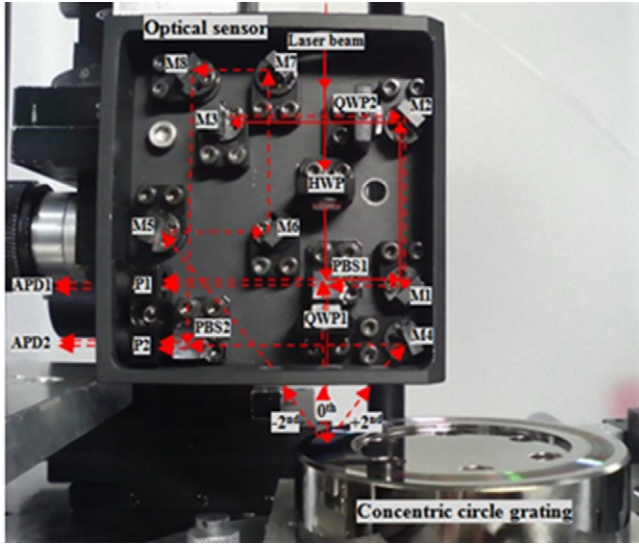|	
Modulation frequency for LD	33 [kHz]
Modulation depth for *X* or *Y*-axis interferometer	3.67 [rad]
Modulation frequency bandwidth for *X* or *Y*-axis interferometer	1.75 [GHz]
Modulation depth for *z*-axis interferometer	3.67 [rad]
Modulation frequency bandwidth for *Z*-axis interferometer	1.75 [GHz]
Revolution speed of spindle	4 [rpm]
Number of rotation	3 [rotations]
Sampling rate	10 [kHz]
Cut off frequency of low pass filter	300 [Hz]

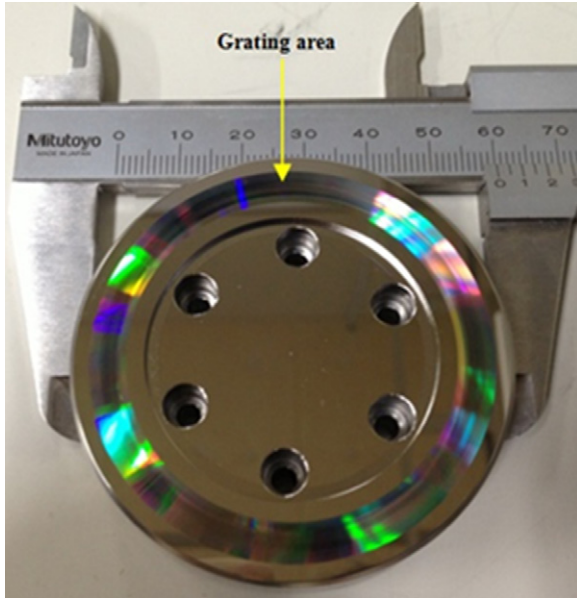**Figure 4.** Photograph of the optical sensor.

Figure 5. Photograph of the concentric circle grating ($2\,\mu$m pitch).

diffracted from ±2nd order of the grating, the initial phase of the 0th order interferometer, the initial phase of the ±2nd order interferometer, the refractive index of air, the speed of light, the frequency of the light source, the optical path difference of the 0th order interferometer arms and the optical path difference of the ±2nd order interferometer arms, respectively. In the system, the vertical displacement Δz is assumed to be the same order of the wavelength of the LD (i.e. $\Delta z \sim \lambda$). We add small modulation to the frequency of LD as

$$f = f_0 + \Delta f, \qquad (11)$$

where f_0 and Δf are the center frequency and modulation. We assume

$$\frac{\Delta f}{f_0} \ll 1 \left(\frac{\Delta \lambda}{\lambda} \ll 1 \right), \qquad (12)$$

$\Delta \lambda$ is the wavelength modulation. In equation (9), the second term in the bracket can be calculated as

$$\frac{4\pi n}{c}(f_0 + \Delta f)(L_{\text{int}} + \Delta z)$$

$$= \frac{4\pi n}{c} f_0 (L_{\text{int}} + \Delta z) + \frac{4\pi n}{c} L_{\text{int}} \Delta f - \frac{4\pi n}{\lambda^2} \Delta \lambda \Delta z. \qquad (13)$$

The order of the last term of equation (13) is

$$\left| -4\pi n \frac{\Delta \lambda}{\lambda} \frac{\Delta z}{\lambda} \right| \sim \left| \frac{-4\pi n}{c} \frac{\Delta \lambda}{\lambda} \right| \ll 1. \qquad (14)$$

Therefore equation (9) can be represented as

$$I_{0\text{F}} = |E_0|^2 + |E_{\text{F}}|^2$$
$$+ 2E_0 E_{\text{F}} \cos\left\{ \varphi_{\text{int},0} - \frac{4\pi}{c} n L_{\text{int}} f_0 - \frac{4\pi}{c} n f_0 \Delta z - \frac{4\pi}{c} n L_{\text{int}} \Delta f \right\}$$
$$= |E_0|^2 + |E_{\text{F}}|^2 + 2E_0 E_{\text{F}} \cos\left\{ \varphi_0' - \frac{4\pi}{c} n f_0 \Delta z - \frac{4\pi}{c} n L_{\text{int}} \Delta f \right\}, \qquad (15)$$

where $\varphi_0' \left(= \varphi_{\text{int},0} - (4\pi/c) n L_{\text{int}} f_0 \right)$ is an initial phase of interferometer. We add the sinusoidal modulation to $(-(4\pi/c) n L_{\text{int}} \Delta f)$ using

$$-\frac{4\pi}{c} n L_{\text{int}} \Delta f = k_{m,0} \sin \omega_m t, \qquad (16)$$

where $k_{m,0}$ is a modulation depth. By combining equations (15) and (16) and using the Bessel function, we obtain

$$I_{0\text{F}} = |E_0|^2 + |E_{\text{F}}|^2 + 2E_0 E_{\text{F}}$$
$$\times \left[\cos\left(\varphi_0' - \frac{4\pi}{c} n f_0 \Delta z \right) \left\{ J_0(k_{m,0}) + 2 \sum_{m=1}^{\infty} J_{2m}(k_{m,0}) \cos 2m \omega_m t \right\} \right.$$
$$\left. - \sin\left(\varphi_0' - \frac{4\pi}{c} n f_0 \Delta z \right) \left\{ 2 \sum_{m=1}^{\infty} J_{2m+1}(k_{m,0}) \sin(2m+1) \omega_m t \right\} \right]. \qquad (17)$$
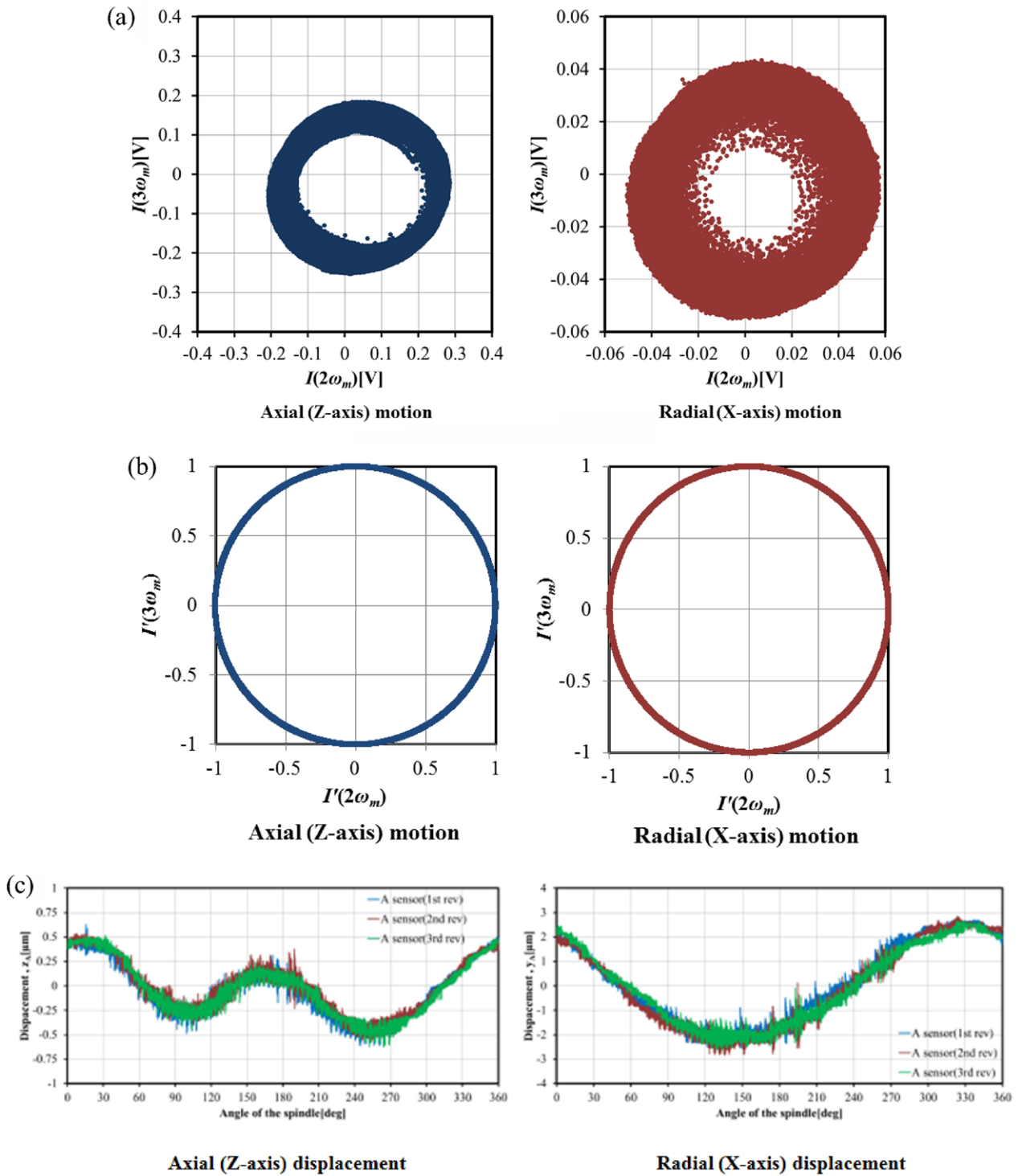
Figure 6. Spindle motion measurement with one optical sensor. (*a*) Raw Lissajous diagram. (*b*) Normalized Lissajous diagram. (*c*) The axial (*Z*-axis) and radial (*X*-axis) displacements of the spindle motion.

In order to reduce the effect from the amplitude modulation of LD, we select 2nd-harmonic ($2\omega_m$) and 3rd-harmonic ($3\omega_m$). We apply the reference signal of 2nd-harmonic cosine wave ($2\omega_m$) and the reference signal of 3rd-harmonic sine wave ($3\omega_m$) to the lock-in detection signal of the interference light intensity I_{0F}. When the interference light intensity I_{0F} from equation (17) is synchronized by the lock-in amplifier 1 (LIA1) with the reference signal of 3rd-harmonic sine wave ($3\omega_m$), and the lock-in amplifier 2 (LIA2) with the reference signal of 2nd-harmonic cosine wave ($2\omega_m$) (see figure 2), two signals of LIA1 and LIA2 can be written as

$$I_{\pm 2}(2\omega_m) = 2E_{+2}E_{-2}J_2(k_{m,\pm 2})\cos\left(\varphi'_{\pm 2} - \frac{8\pi}{d}\Delta x\right). \quad (22)$$

From equations (18), (19), (21) and (22), we can obtain a Lissajous diagram from two reference signals with a phase difference of 90° [16]. Using the Lissajous diagram, the axial (*z*-axis) and radial (*x*-axis) displacements of the grating can be calculated concurrently. In the optical sensor, to reduce crosstalk error between the Z and X axes interferometers down to 10^{-4} order, the grating plane must be aligned to be nearly parallel with the XY plane within 10 arcseconds [13]. Even though the electronics circuit in the interferometer is complicated, we can reduce the number of optical elements for the interpolation. From previous work [16], we estimate that the measurement uncertainties for X and Z axes interferometers are less than $0.1\,\mu$m.

3. Experiments and discussions

3.1. Optical sensor performance

In order to confirm equations (18), (19), (21) and (22), we constructed a spindle motion measurement system using one optical sensor as shown in figure 3. An LD (Hitachi, model: HL6344G), with a wavelength of 635 nm and a sinusoidal phase modulation frequency of 33 kHz, was applied to the interferometer as a light source. Figure 4 shows a photograph of the optical sensor. In the sensor, the optics were firmly fixed in the plate. The optical sensor was fixed over the concentric circle grating. APD1 detected the interference signal of axial (*z*-axis) motion and APD2 detected the interference signal of radial (*x*-axis) motion. The concentric circle grating with a pitch of $2\,\mu$m was set up on the spindle motor (Chuo Precision, model: ARS-636-HM). Figure 5 shows a photograph of the concentric circle grating. The fine concentric circle grating is the key technology for attaining our measurement goal. The grating was fabricated using an ultra-precise numerical control (NC) cutting machine tool (ROBONANO@ FANUC) and a sharp single crystal diamond tool with a top radius of less than 1μm. The material used was stainless steel with a nickel phosphide plating of $100\,\mu$m thickness. Many grating grooves were formed on the nickel phosphide plate. In the grating, 1000 pitches were formed with a concentric circle structure [13]. Table 1 lists the specifications of the spindle motor [17]. In the experiment, its maximum speed was $24^\circ\,s^{-1}$, or 4 rpm. The measurement conditions applied for the spindle motion are shown in table 2. We measured the spindle motion over 3 rotations. In the measurement, we used four commercial digital lock-in amplifiers (SRS-620). The cut off frequency of the low pass filter of the lock-in amplifier was 300 Hz. Figure 6 shows the measurement results of spindle motion using one optical sensor. Figure 6(*a*) shows the raw Lissajous diagram of the axial (*z*-axis) and radial (*x*-axis) motion of the spindle. In figure 6(*a*), the Lissajous

Figure 7. Measurement system for spindle radial, axial and angular motions.

$$I_{0F}(3\omega_m) = -2E_0E_FJ_3(k_{m,0})\sin\left(\varphi'_0 - \frac{4\pi}{c}nf_0\Delta z\right), \quad (18)$$

$$I_{0F}(2\omega_m) = 2E_0E_FJ_2(k_{m,0})\cos\left(\varphi'_0 - \frac{4\pi}{c}nf_0\Delta z\right), \quad (19)$$

where $J_2(k_{m,0})$ and $J_3(k_{m,0})$ are the Bessel function of 2nd and 3rd order. The interference light intensity $I_{\pm 2}$ of the $\pm$2nd-order diffraction at APD2 is also written as

$$
\begin{aligned}
I_{\pm 2} = &|E_{+2}|^2 + |E_{-2}|^2 + 2E_{+2}E_{-2}\Bigg[\cos\left(\varphi'_{\pm 2} - \frac{8\pi}{d}\Delta x\right)\\
&\times\left\{J_0(k_{m,\pm 2}) + 2\sum_{m=1}^{\infty}J_{2m}(k_{m,\pm 2})\cos 2m\omega_m t\right\}\\
&-\sin\left(\varphi'_{\pm 2} - \frac{8\pi}{d}\Delta x\right)\left\{2\sum_{m=n}^{\infty}J_{2m+1}(k_{m,\pm 2})\sin(2m+1)\omega_m t\right\}\Bigg],
\end{aligned}
\quad (20)
$$

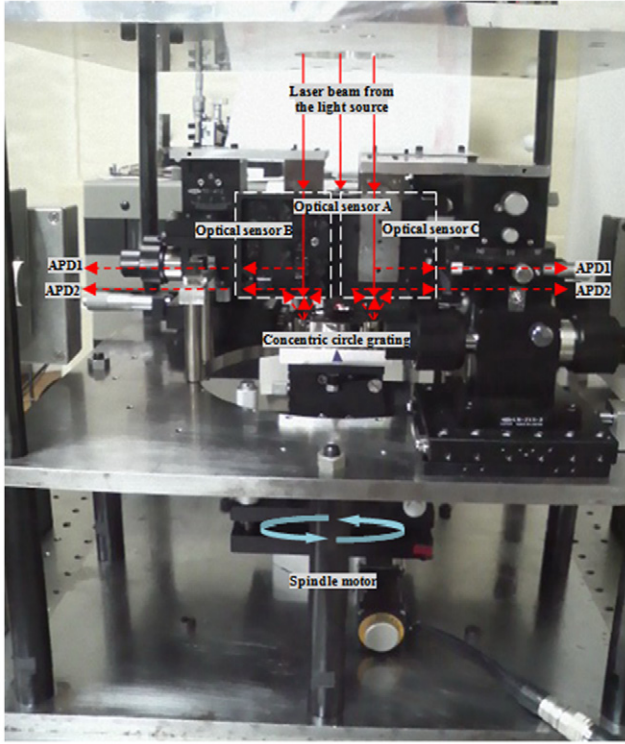where $\varphi'_{\pm 2}$ is an initial phase of interferometer, and $k_{m,\pm 2}$ is a modulation depth. When the interference light intensity $I_{\pm 2}$ from equation (20) is synchronized by the lock-in amplifier 3 (LIA3) with the reference signal of 3rd-harmonic sine wave ($3\omega_m$), and the lock-in amplifier 4 (LIA4) with the reference signal of 2nd-harmonic cosine wave ($2\omega_m$) (see figure 2), the two signals of LIA3 and LIA4 can be written as

$$I_{\pm 2}(3\omega_m) = -2E_{+2}E_{-2}J_3(k_{m,\pm 2})\sin\left(\varphi'_{\pm 2} - \frac{8\pi}{d}\Delta x\right), \quad (21)$$
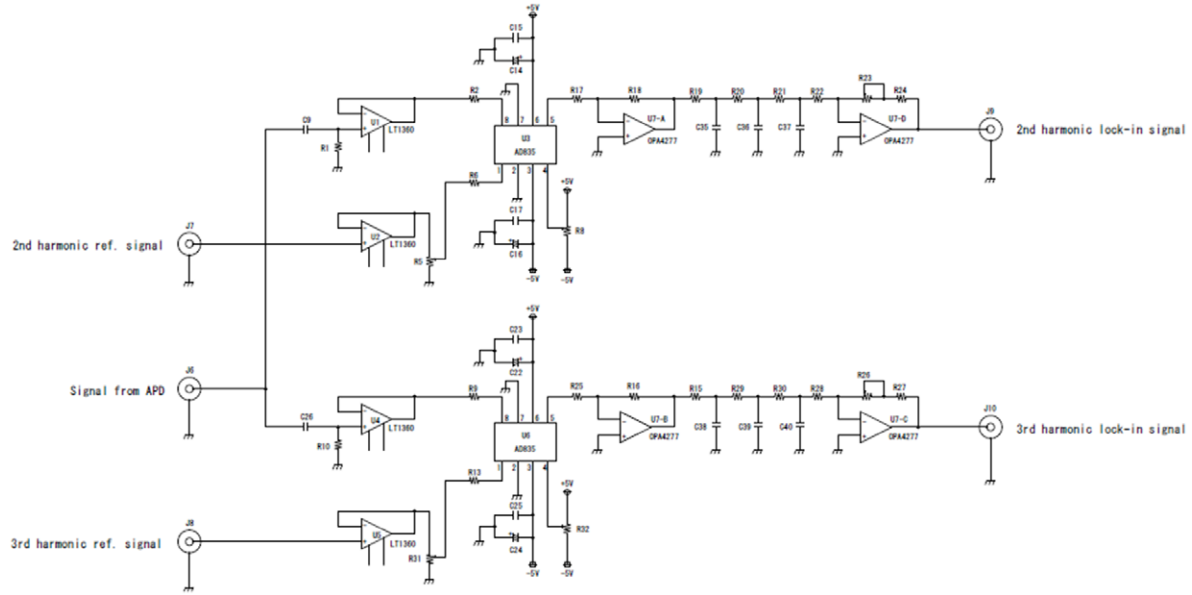
Figure 8. Circuit diagram of the analog lock-in amplifier.

diagrams of spindle motion are deformed due to variation of the laser beam intensity, and the center of the Lissajous diagram is not the same as the origin. In this case, a normalized Lissajous diagram can be calculated using equations as follows,

$$I_Z' (3\omega_m) = \frac{I_{0F}(3\omega_m) J_3(k_m)}{\sqrt{(I_{0F}(2\omega_m) J_3(k_m))^2 + (I_{0F}(3\omega_m) J_2(k_m))^2}}$$
$$= \sin\left(\varphi_0' + \frac{4\pi}{c} n f_0 \Delta z \right), \tag{23}$$

$$I_Z' (2\omega_m) = \frac{I_{0F}(2\omega_m) J_3(k_m)}{\sqrt{(I_{0F}(2\omega_m) J_3(k_m))^2 + (I_{0F}(3\omega_m) J_2(k_m))^2}}$$
$$= \cos\left(\varphi_0' + \frac{4\pi}{c} n f_0 \Delta z \right), \tag{24}$$

$$I_x' (3\omega_m) = \frac{I_{\pm2}(3\omega_m) J_2(k_m)}{\sqrt{(I_{\pm2}(2\omega_m) J_3(k_m))^2 + (I_{\pm2}(3\omega_m) J_2(k_m))^2}}$$
$$= \sin\left(\varphi_{\pm2}' + \frac{8\pi}{d} \Delta x \right), \tag{25}$$

$$I_x' (2\omega_m) = \frac{I_{\pm2}(2\omega_m) J_3(k_m)}{\sqrt{(I_{\pm2}(2\omega_m) J_3(k_m))^2 + (I_{\pm2}(3\omega_m) J_2(k_m))^2}}$$
$$= \cos\left(\varphi_{\pm2}' + \frac{8\pi}{d} \Delta x \right). \tag{26}$$

The normalized Lissajous diagram is shown in figure 6(*b*). In figure 6(*b*), the center and radius of the diagram are the origin and 1. Figure 6(*c*) shows the axial (*z*-axis) and radial (*x*-axis) displacement of the spindle motion. In figure 6(*c*), the centering error of approximately 5 μm can be seen.

3.2. Concurrent measurement of spindle radial, axial and angular motions

We also constructed a concurrent spindle motions measurement system as shown in figure 7. In the experiment, we applied analog lock-in amplifiers for three optical sensors. Figure 8 shows a circuit diagram of two lock-in amplifiers for 2nd and 3rd harmonic lock-in detections. The circuit used 4-quadrant multipliers (AD835, Analog Devices), precision operational amplifiers and a passive low pass filter. Three optical sensors were fixed over the concentric circle grating. The measurement conditions applied for the spindle motion were the same as table 2. Figure 9 shows the axial (*z*-axis) and radial (*x* or *y*-axis) displacement of the spindle motion from three optical sensors A, B and C with 3 rotations. In figure 9, the axial (*z*-axis) and the radial (*x* or *y*-axis) motions are approximately 1 μm and 5 μm, respectively. Because the radial motions have a component whose period is the same as that of the rotation, the centering error mostly affects the radial motions. Figures 10 and 11 show two concurrent measurements of radial (R_x and R_y), axial (R_z) and angular (θ_x and θ_y) motions, respectively, obtained on different days. In figures 10 and 11, the magnified figures of radial, axial and angular motions are also shown, respectively. In the magnified figures, vibrations, whose frequency is approximately 54 Hz, are clearly seen (there are approximately 54 periods in 24 degrees (= 1 s)). By comparing figures 10 and 11, the spindle motion is not a repeatable one, the spindle motion changes day by day. From the figures 10 and 11, radial (R_x and R_y), axial (R_z) and angular (θ_x and θ_y) motions are approximately 5 μm, 0.5~1 μm and 1~3 arcseconds, respectively. If the displacement is larger than $\lambda/2$ or $d/2$ for the sampling time (= 1/sampling rate (f_s)), it is impossible to interpolate or determine the displacement using a Lissajous diagram. The relationship between the maximum speed (v_{max}) and the sampling rate (f_s) is described by
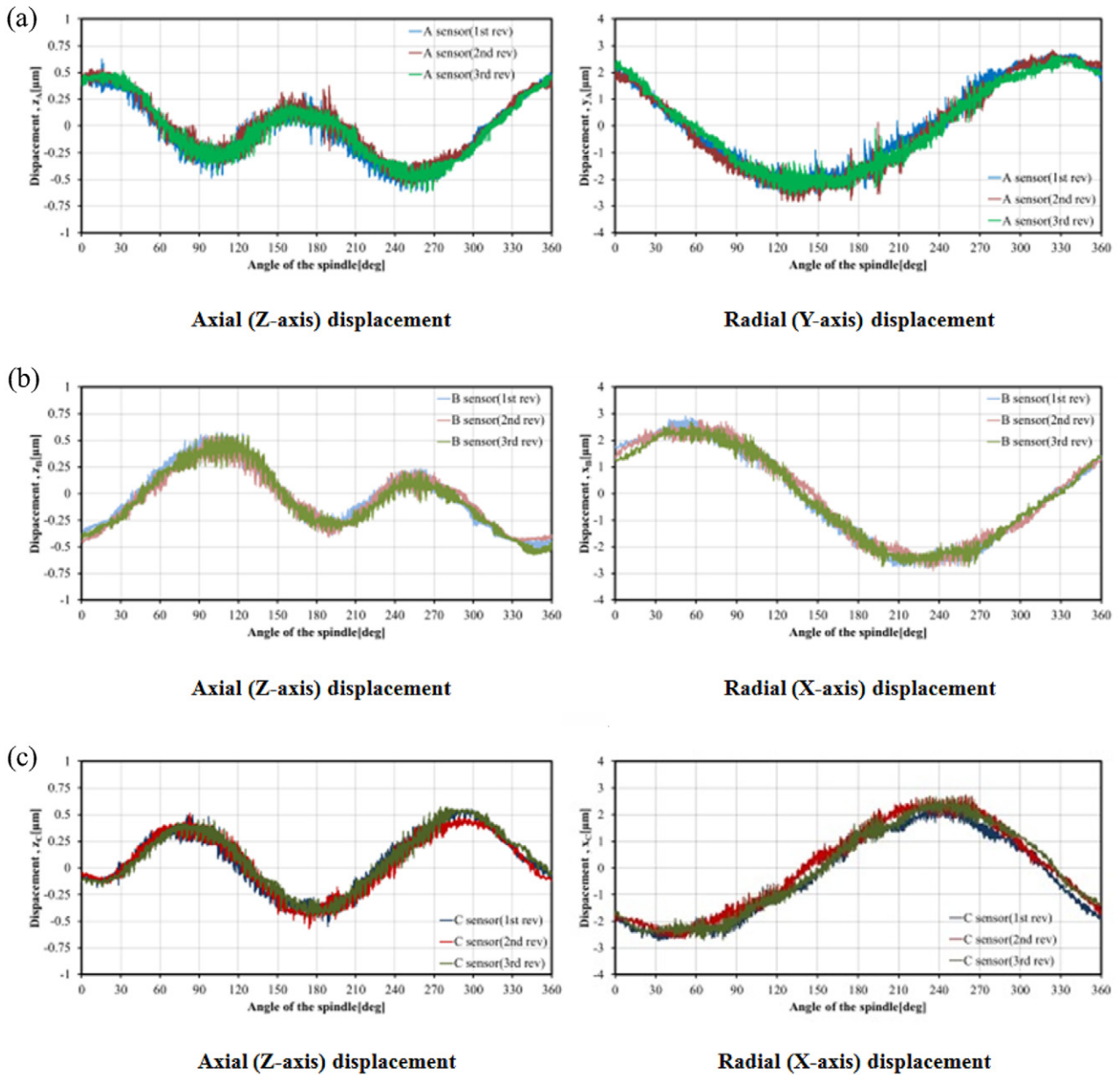
Figure 9. Axial (*Z*-axis) and radial (*X* or *Y*-axis) displacements of the spindle from three optical sensors. (*a*) Optical sensor A. (*b*) Optical sensor B. (*c*) Optical sensor C.

$$\frac{v_{max}}{f_s} < \frac{\lambda}{2} \text{ or } \frac{d}{2}. \tag{27}$$

In the measurement $f_s = 10\,\text{kHz}$, $\lambda = 635\,\text{nm}$ and $d = 2\,\mu\text{m}$, then

$$v_{max} < 3.18\,\text{mm/s (axial)}. \tag{28}$$

$$v_{max} < 10\,\text{mm/s (radial)}. \tag{29}$$

From the magnified figure on figure 10(*a*), the maximum vibration speed is approximately 0.3 mm/s ($\approx 3\,\mu\text{m} \times 2 \times 54\,\text{Hz}$), therefore we could obtain the vibration by our proposed method. The experimental results show that the concurrent measurements of the spindle radial, axial and angular motions were successfully attained.

4. Conclusions and next work

In this paper, we have proposed a measurement method using concentric circle grating and phase modulation interferometers to measure spindle radial, axial, and angular motions concurrently. The measurement principle of an optical sensor using a concentric circle grating to measure the displacement was clarified. The displacement (Lissajous diagram) can be obtained when we add a small modulation to the frequency of the light source. If there is deformation of the Lissajous diagram due to variations of the laser source intensity and other causes, a normalized Lissajous diagram can be obtained. By using three optical sensors and the concentric circle grating, we attained concurrent measurements of spindle radial, axial, and angular motions at the low speed of 4 rpm with a sinusoidal phase
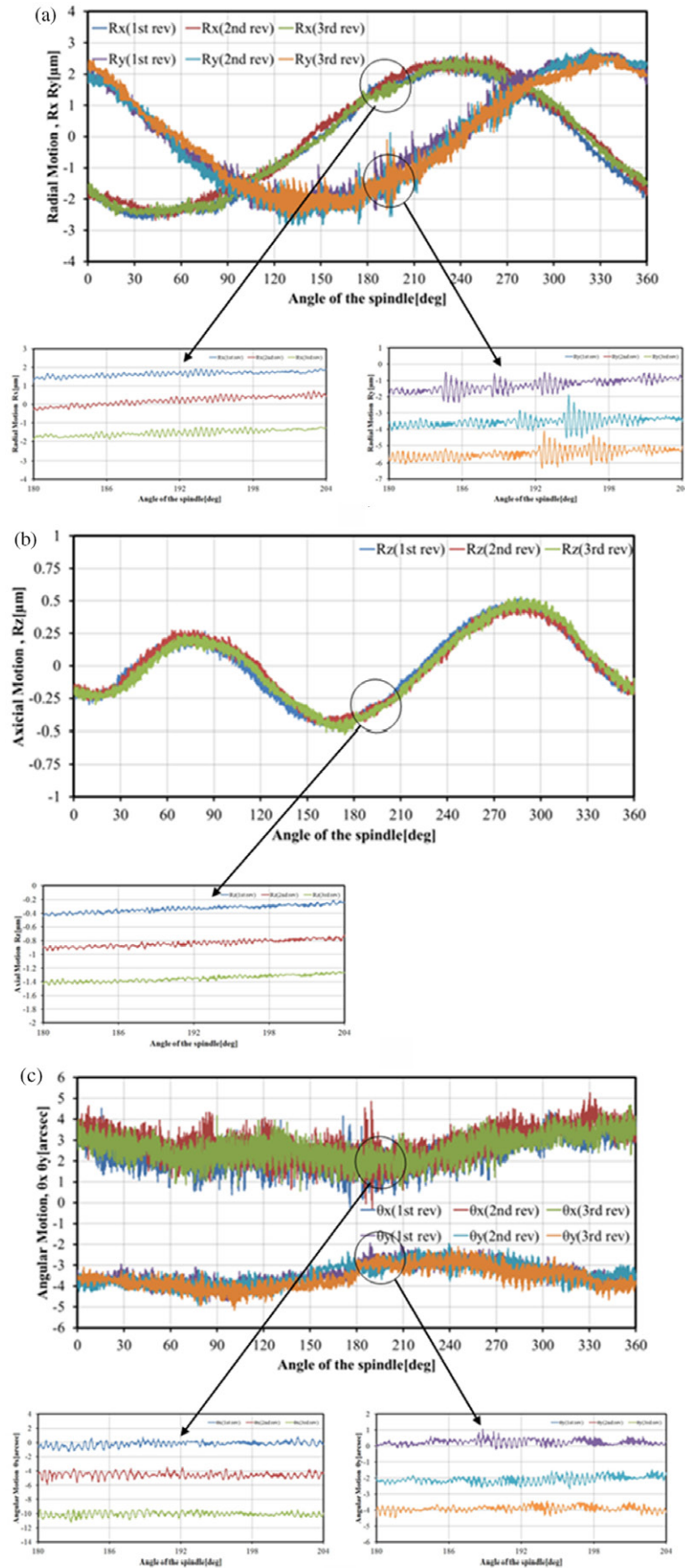
Figure 10. The radial, axial and angular motions of spindle and their magnification figures. (*a*) Radial motions R_x, R_y. (*b*) Axial motion R_z. (*c*) Angular motions θ_x, θ_y.
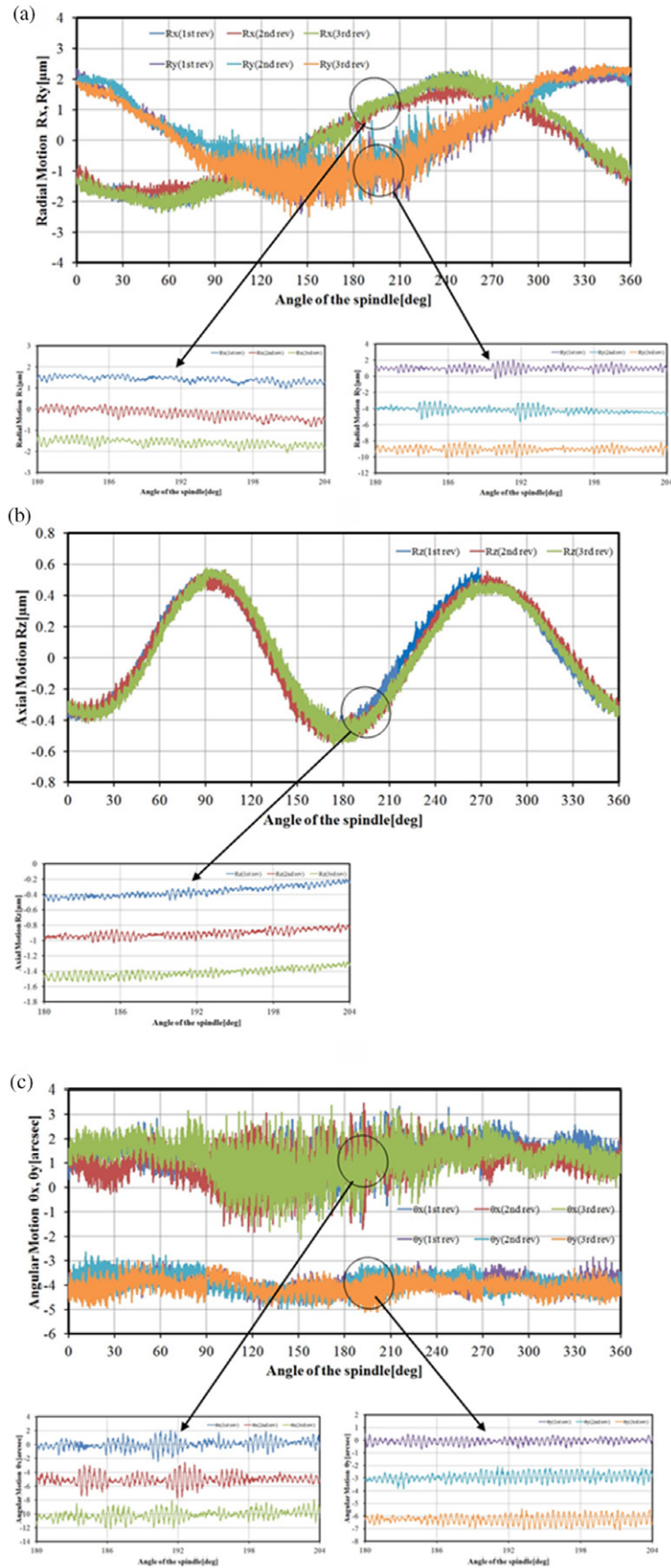
Figure 11. The radial, axial and angular motions of spindle. These results were obtained on different day from figure 10. (*a*) Radial motions R_x, R_y. (*b*) Axial motion R_z. (*c*) Angular motions θ_x, θ_y.

modulation frequency of 33 kHz. Based on the results, we are planning to increase the modulation frequency up to several 10 MHz in order to measure the spindle motion at the high speed of 10 krpm, and test the performance of this system in the near future. About the measurement range of our method, there is no limitation for displacement measurement if the spindle motion speed does not exceed the detectable speed (v_{max}). However, crosstalk error between radial and axial interferometers must be solved to increase the measurement range of the angle. In a previous paper [16], we clarified that one of the causes of the interpolation error for the two interferometers is polarization mixing. However, to reduce the interpolation error due to amplitude modulation appearing the laser diode, we need a compensation method. We will discuss a theoretical and experimental treatment for compensating interpolation errors due to polarization mixing and amplitude modulation in the near future. To remove the air turbulence effect in the measurement system, we will employ a stabilized chamber. For compensating the artifact form errors (roundness and surface flatness) of the concentric circle grating in the measurement, the concentric circle grating needs to be calibrated. We are also planning to use some error separation methods, such as the reversal method, in order to improve the measurement accuracy. A grating pitch of less than 2 μm is favorable to improve the measurement resolution of radial motion. In this case, we must pay attention to selection of the wavelength of LD, the diffraction order, and the diffraction angle. We are also planning to use a light source with a shorter wavelength. Lastly, we must compare other spindle motion measurement methods with the proposed method in the near future.

Acknowledgment

References

[1] Grejda R, Marsh E and Vallance R 2005 Techniques for calibrating spindles with nanometer error motion *Prec. Eng.* **29** 113–23

[2] Lee J C, Gao W, Shimizu Y, Hwang J, Oh J S and Park C H 2012 Spindle error motion measurement of a large precision roll lathe *Int. J. Prec. Eng. Manuf.* **13** 861–7

[3] Donaldson R 1972 A simple method for separating spindle error from test ball roundness error *Ann. CIRP* **21** 125–6

[4] Marsh E, Couey J and Vallance R 2006 Roundness measurement of spherical artifacts at arbitrary latitude *Prec. Eng.* **30** 353–6

[5] Okuyama E, Nosaka N and Aoki J 2007 Radial motion measurement of high-revolution spindle motor *Measurement* **40** 64–74

[6] Park Y C and Kim S W 1994 Optical measurement of spindle radial motion by Moiré technique of concentric gratings *Int. J. Mach. Tools Manuf.* **34** 1019–30

[7] Kataoka A, Nomura M, Horiuchi O, Shibata T and Murakami Y 2008 A prototype of radial encoder *Proc. JSPE Ann. Spring Meeting (Tokyo)* **2008S** 513–4 (in Japanese)

[8] Gao W, Takahara T and Kiyono S 1998 On machine measurement of angular motion of spindle *Proc. 13th ASPE Ann. Meeting* p 355

[9] Ogura I and Okazaki Y 2001 Precision measurement for axial and angular motion errors of turning spindle by using multi point method *J. Japan. Soc. Prec. Eng.* **67** 1120–4

[10] Marsh E R 2008 *Precision Spindle Metrology* (Pennsylvania: DEStech Publications)

[11] Gao W and Kimura A 2007 A Three-axis displacement sensor with nanometric resolution *Ann. CIRP* **56** 529–32

[12] Kimura A, Arai Y and Gao W 2008 A two-degree-of-freedom linear encoder for measurement of position and straightness *Proc. 23rd ASPE Ann. Meeting and 12th ICPE Meeting (Portland)* pp 550–3

[13] Madden M, Aketagawa M, Ohkubo Y, Kimura S, Maruyama H, Higuchi S and Okuyama E 2009 Proposal of concurrent measurement method for spindle radial, axial and angular motios using concentric grating interferometers *Int. J. Surf. Sci. Eng.* **3** 242–52

[14] Sasaki O and Okasaki H 1986 Sinusoidal phase modulating interferometry for surface profile measurement *Appl. Opt.* **52** 3137–40

[15] Dandridge A, Tveten A B and Giallorenzi T G 1982 Homodyne demodulation scheme for fiber optic sensors using phase generated carrier *IEEE J. Quantum Electron.* **18** 1647–53

[16] Madden M, Aketagawa M, Uesugi S, Kumagai T and Okuyama E 2013 Sindle error motion measurement using concentric circle grating and phase modulation interferometers *Int. J. Automation Technol.* **7** 506–13

[17] Chuo Precision Industrial Co. Ltd Catalog of products, version 37th (www.chuo.co.jp/contents/hp0341/list.php?CNo=341&ProCon=5433) (in Japanese)